A LARGE DISPLACEMENT FINITE ELEMENT ANALYSIS OF A REINFORCED UNPAVED ROAD

by

Harvey John Burd

A Thesis submitted for the Degree
of Doctor of Philosophy at the
University of Oxford

Hertford College

Trinity Term, 1986

ABSTRACT

A Large Displacement Finite Element Analysis of a Reinforced Unpaved Road

H. J. Burd
Hertford College, University of Oxford

A Thesis submitted for the Degree of Doctor of Philosophy

Trinity Term 1986

A series of finite element predictions of the behaviour of a reinforced unpaved road consisting of a layer of fill compacted on top of a clay subgrade with rough, thin reinforcement placed at the interface, is described in this thesis. These numerical solutions are obtained using a large strain finite element formulation that is based on the displacement method, and are restricted to the case of plane strain, monotonic loading. Separate elements are used to model the soil and reinforcement.

In the finite element formulation, an Eulerian description of deformation is adopted and the Jaumann stress rate is used in the soil constitutive equations. Elastic perfectly-plastic soil models are used which are based on the von Mises yield function for cohesive soil and the Matsuoka criterion for frictional material. Emphasis is placed on obtaining new closed form solutions to parts of calculations that are performed numerically in many existing finite element formulations. The solution algorithm is based on a 'Modified Euler Scheme'.

The computer implementation of the formulation is checked against an extensive series of test problems with known closed form solutions. These include the analysis of finite deformation of a single element of material and the calculation of small strain collapse loads. Finite cavity expansion is also studied.

This numerical formulation is used to perform back analyses of a series of reinforced unpaved road model tests. The reinforcement tensions, and the stresses at the interface with the surrounding soil, are calculated using the numerical model and discussed with a view to identifying the mechanisms of reinforcement.

Two existing analytical design models of the reinforced unpaved road are described and critically reviewed in the light of the finite element results.

CONTENTS

CHAPTER 1 INTRODUCTION

CHAPTER 2 THE CHOICE OF FORMULATION OF A FINITE ELEMENT MODEL

CHAPTER 3 FORMULATION OF CONTINUUM ELEMENTS

CHAPTER 4 STRESS UPDATE CALCULATIONS FOR CONTINUUM ELEMENTS

CHAPTER 5 FORMULATION OF MEMBRANE ELEMENTS

CHAPTER 6 VERIFICATION OF THE FINITE ELEMENT PROGRAM

CHAPTER 7 ANALYSIS OF A REINFORCED ROAD

CHAPTER 8 MECHANISMS OF REINFORCEMENT

CHAPTER 9 TWO EXISTING DESIGN METHODS

CHAPTER 10 CONCLUDING REMARKS

REFERENCES

'The fear of the Lord is the
beginning of wisdom.' *Psalm 111 v. 10*

ACKNOWLEDGEMENTS

The research described in this thesis was carried out during the period April 1983 to April 1986, and was made possible by the financial support of a SERC Research Assistantship.

All of this work was undertaken while I was a member of the Oxford Soil Mechanics Group, and I should like to express gratitude to my fellow workers in the group for their advice and encouragement.

I am particularly indebted to Dr George Milligan who supervised my work for the first six months of this research, and to Dr Guy Houlsby who acted in this capacity for the remaining period of the project. Guy Houlsby has been a stimulating person to work with and I wish to record my sincere appreciation of his help and guidance. I should also like to thank Dr Scott Sloan who, as well as helping me to understand the basic principles of finite element analysis, provided me with a copy of the mesh generation program that was used extensively in this research.

I am also grateful to the Fellows of Hertford College who supported me by means of a Carreras Senior Scholarship. I particularly wish to thank Dr Gerry McCrum who has often gone out of his way to encourage me in my work.

Finally, I would wish to thank my family and friends who bore with considerable patience my preoccupation with this thesis during the six-month period that it was in preparation.

CHAPTER 1 INTRODUCTION

1.1 The Reinforced Unpaved Road

The use of fabric or polymer grid reinforcing materials to improve the strength and stability of geotechnical structures is increasing. The applications of this reinforced earth technique are diverse, and include the construction of retaining walls, bridge abutments, embankments and roads. The primary incentive for the use of this technique in favour of more traditional methods is that in some cases it can reduce the construction costs. Although the benefits of using reinforcing materials are well known, current design methods are generally unable to give accurate predictions of performance. As a result, over-generous safety factors are necessary which increase construction costs and therefore make the use of the reinforced earth technique less attractive.

The particular application of this technique that is the subject of the research described in this thesis is the use of soil reinforcement to improve the structural performance of reinforced unpaved roads built over soft subgrades. In this type of construction the reinforcement is placed directly onto the subgrade prior to placement and compaction of a fill layer. It is generally accepted that in this application the reinforcement becomes increasingly effective as displacements become large, which means that this particular technique is best suited to the construction of roads where substantial surface rutting is acceptable.

It is clearly necessary that analytical methods which may be used to predict the load/deformation characteristics of reinforced unpaved roads are available to practising engineers for design purposes. Several simple design methods have therefore been proposed in recent years and these are generally based on simple analytical models of the reinforcement mechanisms. These design models are generally limited to the analysis of road behaviour during a single load application. The extension to the cyclic loading case is made (if at all) on the basis of empirical rules.

One of the first mechanistic models of the reinforced unpaved road was proposed by Barenberg et al. (1975). The suggested method was to limit the vertical stress at the base of the fill layer to $N_c c_u$ where N_c is a bearing capacity factor and c_u is the undrained shear strength of the subgrade. In the unreinforced case N_c should be set to 2.8 (being slightly less than π, the value corresponding to the elastic limit stress) and in the presence of reinforcement N_c could be increased to 5.0 (being slightly less that $\pi + 2$, which corresponds to plastic failure of the subgrade). The practical use of this simple approach was reported by Steward and Mohney (1982), who were involved with the design of unpaved forest roads. Barenberg's method was used as a starting point, but it was found to be necessary to adjust the thickness of the aggregate layer to obtain adequate performance under construction haul traffic.

A more refined model was proposed by Nieuwenhuis (1977) in which the subgrade was treated as an elastic foundation of the Winkler type. The stresses at the base of the fill layer were approximated by a hyperbolic cosine function and shear stresses at the reinforcement/soil interface were assumed to be zero. The shape of the reinforcement for the case of a single monotonic load was obtained by formulating and solving a one-dimensional membrane equation. This solution was then used to obtain the load/displacement response of the structure.

A much more realistic and useful design model was proposed by Giroud and Noiray (1981). This method considers the effect of subgrade plasticity and also includes some attempt to quantify the effect of traffic loading. A further feature of this design method is that it considers the interaction between the response of the wheels at both ends of the axle rather than considering each wheel in isolation. This mechanistic model is described in greater depth in Section 9.2.

An improved form of the Nieuwenhuis model was proposed by Sellmeijer et al. (1982) in which the original method was modified to include the effects of subgrade plasticity. The hyperbolic cosine approximation to the stresses at the base of the fill layer was abandoned in favour of the procedure first proposed by Giroud and Noiray (1981) in which the stresses were assumed to be constant over a rectangular area directly under the wheel. The Sellmeijer model is otherwise similar to the Nieuwenhuis method in that a membrane equation is formulated and solved to give the reinforcement profile for the case when frictional stresses acting on the reinforcement/soil interface are zero. No attempt is made in this design model to deal with the effect of traffic loading.

An alternative variation of the Nieuwenhuis method was proposed by Bourdeau et al. (1982). In this approach the idea of an elastic subgrade is retained, but the method is not limited to the case when the frictional stresses acting on the reinforcement are zero. The inclusion of shear stresses at the soil/reinforcement interface leads to a non-linear membrane equation which is solved using a finite difference scheme. The authors made no attempt to develop their approach into a complete design method, but instead suggested that it could be used to calculate the 'anchorage length' for the reinforcement.

A design method that has some of the characteristics of the Giroud and Noiray model but which treats each wheel load independently has been proposed by Sowers et al. (1982). In this approach, which is limited to the analysis of static loads, some attempt was made to calculate the variation of the strains in the reinforcement. The method is described in detail in Section 9.3.

As well as the use of analytical methods of design, some interest has been shown in the area of formulating numerical models of the reinforced unpaved road. One of the earliest attempts was described by Bell et al. (1977) in which a finite element method was used. The fill was treated as being elastic and an anisotropic elastic-perfectly plastic constitutive law was used to model the subgrade. An attempt was made to correlate the finite element results with the measured behaviour of a test road built over muskeg. The numerical predictions, however, tended to underestimate the effects of the reinforcement as observed in the tests.

A further application of the finite element method to a reinforced earth problem of this sort has been described by Boutrup and Holtz (1983). The particular problem studied was a low granular embankment built over a soft muskeg foundation and which both soil types were represented by a Drucker-Prager model. The numerical results indicated that the presence of the reinforcement would reduce both the differential settlements of the embankment and the magnitude of the shear stresses transmitted to the subgrade.

A detailed description of a finite element formulation suitable for the analysis of an axi-symmetric reinforced unpaved foundation is given by Zeevaert (1980). In this formulation, a Drucker-Prager work-hardening model was used to describe the constitutive behaviour of both frictional and cohesive soils. The plasticity model was based on the use of an associated flow rule, and the author noted that this was likely to predict unrealistically high dilation rates for the frictional soil. This formulation also included a shear modulus that increased with confining pressure, although this was not implemented in such a way as to exclude the possibility of non-conservative behaviour (Houlsby (1985)). The finite element discretization was based on the use of eight-noded quadrilateral elements with a nine-point Gaussian integration rule to model the soil, and two-noded membrane elements to model the reinforcement. Slip was allowed at the reinforcement/soil interface on the basis of a Coulomb friction law. An 'Updated Lagrangian' approach was used to define the deformation of the material, and the general formulation is described as being valid for large displacements. Since the formulation did not make use of an 'objective' stress rate, however, it was unable to model accurately effects of large rotation.

In addition to the theoretical work described above, there has been a considerable amount of activity in the area of model and full scale tests of reinforced unpaved roads. A good review of the work in this area is given by Love (1984). The main incentive for this experimental work is to obtain information regarding the deformation that occurs in structures of this type, which can then be used to improve the analytical design models. Although the results of these experimental programmes have given much insight into the behaviour of reinforced unpaved roads, instrumentation difficulties mean that little information is available regarding the variation of strains in the reinforcement, or the nature of the reinforcement/soil interface stresses.

These experimental data are also of considerable use in checking finite element predictions of the behaviour of reinforced unpaved roads. If a particular finite element formulation is proved to be reliable in this way, then it may be used to calculate the quantities that are difficult to measure accurately in the physical model.

1.2 A Finite Element Model for Reinforced Unpaved Roads

A finite element formulation that is capable of making accurate predictions of a reinforced unpaved road deforming under conditions of plane strain monotonic loading is described in Chapters 2,3,4 and 5 of this thesis. The computer implementation of this formulation has been carefully checked using a series of test problems, and this procedure is described in Chapter 6. The primary purpose of this thesis is to describe the finite element back-analysis of a series of tests performed by Love (1984) on a model reinforced unpaved road, and these calculations are described in detail in Chapter 7. The reinforcement mechanisms predicted by these numerical solutions are discussed in Chapter 8, and two existing analytical models of the reinforced unpaved road are compared with the finite element results in Chapter 9.

The finite element formulation described in this thesis is limited to the analysis of roads subjected to a single application of a quasi-static load, and is restricted to plane strain boundary conditions. Although this represents a simplified form of the general reinforced unpaved road problem, it is justified on the basis that this type of analysis can give useful insights into the mechanisms of reinforcement, which can then be used to understand the response under more complicated forms of loading. An additional advantage of the use of these loading conditions is that a considerable amount of plane strain monotonic loading model test data exists which can be used to validate the finite element formulation (e.g. Love (1984), Kinney (1979)).

It is established from the results of model and full scale tests performed on reinforced unpaved roads that the effects of the reinforcement become most apparent when deformations are large. In order to model this behaviour, the finite element formulation described in this thesis has been based on a theory in which the strains and displacements are not confined to being infinitesimal. The ability of this finite element method to model large strain and large displacement effects accurately is an important feature of the formulation.

In a typical reinforced unpaved road the fill is a frictional material and the subgrade is cohesive. In order to develop a realistic numerical model therefore, it is necessary to use constitutive laws appropriate to both these soil types. In this formulation, the von Mises yield criterion is used to model cohesive material, and the Matsuoka yield function (Matsuoka (1976)) is used as the basis of a plasticity model for frictional soil. These yield criteria have been chosen rather than the more usual Tresca and Mohr–Coulomb models on the basis that they do not contain 'singularities' where the yield function cannot be differentiated (except at the origin for the case of the Matsuoka yield function).

In this finite element formulation, two-dimensional elements are used to represent the soil, and one-dimensional elements to model the reinforcement. These reinforcement elements have zero bending stiffness, zero thickness and are linearly elastic with respect to Hencky strain. No slip is allowed at the reinforcement/soil interface, a procedure that may be justified on the basis that reinforcements are available (e.g. geogrids) that provide good interlock with the surrounding soil.

1.3 Conventions and Definitions

The conventions and definitions that are used in this thesis are:-

(i) Stress and strain rates are treated as tensile-positive unless otherwise noted.

(ii) All the theory described in this thesis relates specifically to the case of plane strain loading unless otherwise noted.

(iii) A Cartesian co-ordinate scheme is adopted in which z is the out-of-plane direction. The in-plane stresses are denoted σ_{xx}, σ_{yy} and τ_{xy}.

(iv) The three stress invariants are defined:-

$$I_1 = \sigma_{xx} + \sigma_{yy} + \sigma_{zz} \qquad (1.1)$$

$$I_2 = \sigma_{yy}\,\sigma_{zz} + \sigma_{xx}\,\sigma_{zz} + \sigma_{xx}\,\sigma_{yy} - \tau^2_{xy} \qquad (1.2)$$

$$I_3 = \sigma_{zz}\left[\sigma_{xx}\,\sigma_{yy} - \tau^2_{xy}\right] \qquad (1.3)$$

I'_1, I'_2 and I'_3 denote the equivalent deviatoric stress invariants.

(v) Cauchy stresses and Eulerian strain rates are defined with respect to a Cartesian co-ordinate system that translates with a material point but does not rotate.

(vi) It is necessary in the consideration of large displacement formulations to make a careful distinction between problems with finite displacement but small strain and rotation, and those where strains are large and material rotation needs to be considered (Yamada and Wifi (1977)). The formulation described in this thesis relates to this latter class of problem. In this thesis therefore, the descriptions 'finite displacement' and 'finite strain' should be considered to be synonymous and to refer to the case where rotations are large.

(vii) Some confusion exists in the current literature regarding the precise definition of the terms 'Total Lagrangian', 'Updated Lagrangian' and 'Eulerian' when used to define the co-ordinate systems that are used to describe the deformation. The following definitions are adopted in this thesis. 'Total Lagrangian' refers to a description of deformation in which strains are related to some reference state of the body. The 'Updated Lagrangian' approach refers to a description in which the reference state is updated as the calculation proceeds. This type of material description is often used with an incremental solution scheme in which case the reference state is updated at the end of each calculation step. In an 'Eulerian' description, the material strain rates are related to the instantaneous configuration. It is important to note that the Updated Lagrangian, and Eulerian approaches only become equivalent in the limit of zero step size.

1.4 Nomenclature

For convenience, the most frequently used symbols and their meanings are listed below:-

[B]	Matrix relating strain rate and nodal velocities
c	Shear strength in triaxial compression
c_{ps}	Plane strain shear strength
c_u	Undrained plane strain shear strength
[C]	Distortion rate matrix
d_{ij}	Deformation rate tensor
[D]	Material stiffness matrix
$[D]^e$	Elastic material stiffness matrix
$[D]^p$	Plastic material stiffness matrix
$[D]^{ep}$	Elasto-plastic material stiffness matrix
E	Young's modulus
$\dot{e}_{xx}$, $\dot{e}_{yy}$	Deviatoric Eulerian strain rates

$f(\underset{\sim}{\sigma})$	Yield function
$g(\underset{\sim}{\sigma})$	Plastic potential
G	Shear modulus
I_1, I_2, I_3	Stress invariants
I'_1, I'_2, I'_3	Deviatoric stress invariants
$[J]$	Jacobian matrix
$[K]$	Stiffness matrix
K	Bulk modulus
$[N]$	Shape function matrix
p_f	Footing pressure
p_n	Normal Pressure
p_v	Vertical pressure
$\underset{\sim}{P}$	Vector of nodal forces
$[R]$	Jaumann rotation matrix
s_{xx}, s_{yy}	Deviatoric Cauchy stresses
t	Time
u_i	Generalised velocity
U_i	Generalised nodal velocity
$\underset{\sim}{U}$	Vector of nodal velocities
$\dot{v}$	Volumetric strain rate
x_i	Generalised co-ordinate
X_i	Generalised nodal co-ordinate
$\underset{\sim}{X}$	Vector of nodal co-ordinates
α	Iso-parametric reference co-ordinate
β	Iso-parametric reference co-ordinate
γ	Density
γ_a	Degree of association

$\dot{\gamma}_{xy}$	Eulerian shear strain rate
δ	Footing displacement
δ_{ij}	Kronecker delta
$\dot{\epsilon}_{xx}$, $\dot{\epsilon}_{yy}$, $\dot{\epsilon}_{zz}$	Eulerian strain rates
$\dot{\epsilon}_{L}$	Longitudinal strain rate
$\underset{\sim}{\dot{\epsilon}}$	Vector of Eulerian strain rates
$\underset{\sim}{\dot{\epsilon}}^{e}$	Vector of elastic Eulerian strain rates
$\underset{\sim}{\dot{\epsilon}}^{p}$	Vector of plastic Eulerian strain rates
$\dot{\theta}_{xy}$	Clockwise rotation rate
ν	Poisson's ratio
σ_{ij}	Cauchy stress tensor
σ_{xx}, σ_{yy}, σ_{zz}	Cauchy stresses
σ_{L}	Longitudinal stress
σ_{1}, σ_{2}, σ_{3}	Principal Cauchy stresses
$\underset{\sim}{\sigma}$	Vector of Cauchy stresses
τ_{xy}	Cauchy shear stress
ϕ	Triaxial compression friction angle
ϕ_{ps}	Plane strain friction angle
ψ	Jacobian variation parameter
ψ_{ps}	Plane strain dilation angle
ω	Rotation rate
ω_{ij}	Spin tensor

CHAPTER 2 THE CHOICE OF FORMULATION OF A FINITE ELEMENT MODEL

2.1 Introduction

In this chapter, a review of some selected aspects of finite element theory is discussed with a view to the choice of a finite element formulation that is capable of modelling the reinforced unpaved road problem as defined in Chapter 1. An important feature of this problem is that displacements are large, so the factors involved in deriving finite element models for which strains are not confined to be infinitesimal are discussed at length. In addition, since it is a requirement that the formulation should be capable of modelling undrained clay, a discussion is included of the difficulties that can arise in the analysis of incompressible materials.

2.2 Specific Considerations for Large Displacement Analysis

2.2.1 Kinematical Descriptions

In the infinitesimal theory of elasto-plastic deformations, it is possible to define strain in a unique and unambiguous way. This is not true in large displacement theory however, since a variety of co-ordinate systems may be used to describe the motion and these tend to give rise to different strain definitions (Bathe et al. (1975), Gadala et al. (1984)).

Consider a body subjected to large displacements as shown in Figure 2.1. The motion begins at time $t = 0$ and ends at time $t = T$. The position of a typical material point, P_o, in the initial configuration is described

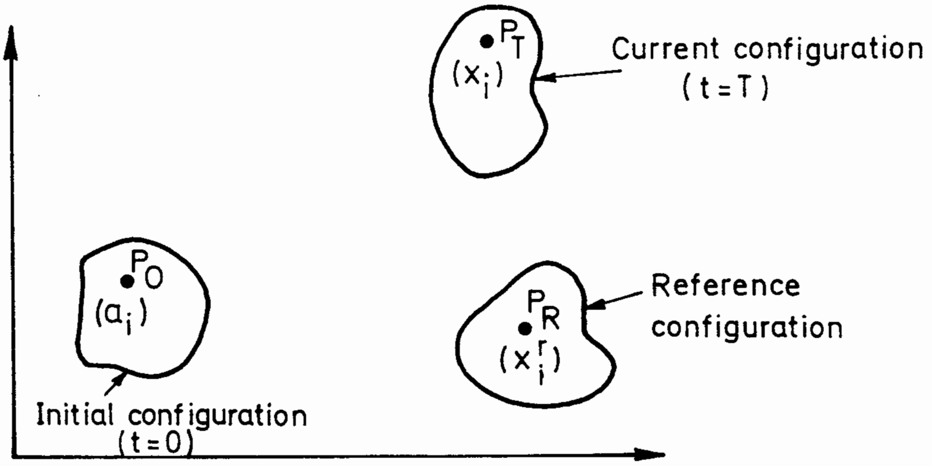

Figure 2.1: Finite Deformation of a Body

by the Cartesian co-ordinate a_i, and the same material point occupies position P_T in the current configuration which is described by the Cartesian co-ordinate x_i. Two separate approaches, termed Lagrangian and Eulerian, may be used to describe the kinematics of deformation of the body.

In the Lagrangian description, the co-ordinate x_i is related to x_i^r the co-ordinate describing the position of the material point in some reference configuration by a function of the form:-

$$x_i = x_i(x_i^r, t) \tag{2.1}$$

This approach lends itself to a description of the deformation in terms of Green-Lagrange strain which is given by the expression:-

$$E_{ij} = \frac{1}{2}\left\{\frac{\partial x_k}{\partial x_i^r}\frac{\partial x_k}{\partial x_j^r} - \delta_{ij}\right\} \tag{2.2}$$

where δ_{ij} is the Kronecker delta. Several possibilities exist for the choice of reference state. In a Total Lagrangian formulation, the reference state is chosen to represent the geometry at the start of the analysis, but other possibilities exist, for example the Updated Lagrangian description in which the reference state is updated as the calculation proceeds. A feature of the Lagrangian approach is that the equilibrium equation is written in terms of the reference configuration of the body. This requires the use of 2nd Piola-Kirchoff stress which is based on the reference configuration and is energetically conjugate with Green-Lagrange strain. This stress measure is required for mathematical consistency although it lacks any obvious physical interpretation.

The Lagrangian formulation is well suited to the analysis of materials for which the constitutive laws may be written in terms of the strains in the body, and where the unstrained configuration of the body may be identified. This is generally not the case in Soil Mechanics, since most plasticity theories are based on the state of stress rather than the deformation. Increments of Green-Lagrange strain cannot be added directly, which means that this strain measure is inconvenient for use in an incremental formulation.

One of the earliest finite element formulations valid for displacements of arbitrary magnitude was based on a Lagrangian description in which an elasto-plastic constitutive law was used to relate Green-Lagrange strain rate to the Jaumann rate of the 2nd Piola-Kirchoff stress (Hibbitt et al. (1970)). In this formulation, an additive decomposition of strain rate into elastic and plastic parts was used in the same way as in the infinitesimal theory. This generalization of the small strain case was discussed by Lee (1969) who argues that additive decomposition of the

Green-Lagrange strain rate is not valid, and suggests a multiplicative decomposition instead. This particular point is also mentioned by Nemat-Nasser (1979) and Lee and McMeeking (1980). Several other workers have published Lagrangian formulations including Zeevaert (1980) who describes a finite element method suitable for the analysis of the axi-symmetric reinforced unpaved road problem.

An alternative to the Lagrangian approach is the Eulerian description which, although currently less popular than the Lagrangian formulation, can sometimes lead to simpler forms of the finite element equations. The basis of the Eulerian approach is to consider the velocity of a material point, u_i, in the current configuration, to be related to the co-ordinates of the material point, x_i and the time t in a relationship of the form:-

$$u_i = u_i(x_i, t) \tag{2.3}$$

The deformation of the material may then be described by deformation rates obtained from the partial derivatives of the above expression:-

$$d_{ij} = \frac{\partial u_i}{\partial x_j} \tag{2.4}$$

This form of the kinematical equations is particularly well suited to the analysis of materials for which constitutive laws are conveniently written in terms of stress and strain rates as is often the case for problems in Soil Mechanics.

Kinematical descriptions of this type have been used by Seth (1935) and Murnaghan (1937) for the solution of large strain problems in elasticity, and by Osias and Swedlow (1974), McMeeking and Rice (1975), Carter et al. (1977) and Carter (1977) as the basis of large strain elasto-plastic finite element formulations.

The choice of kinematical description depends mainly on the form of the material behaviour that is being modelled, but may be influenced by the ease with which the appropriate material properties can be measured and, to a certain extent, on personal preference. The Lagrangian approach is best suited to those problems where the constitutive law may be written in terms of the total deformation of the material. The Eulerian description, however, is well suited to the analysis of materials for which the constitutive law is expressed in terms of the current stresses. A further contrast between these two approaches is that unlike Green-Lagrange strain, the strains obtained by integrating the Eulerian strain rates are not geometrically significant because of path dependence (Yamada and Wifi (1977)).

In spite of the fact that the Eulerian description is currently less popular that the Lagrangian approach, it is the author's opinion that Eulerian variables have much to recommend them, and these will therefore be used in the remainder of this dissertation.

2.2.2 Objective Stress Rates

For a mathematical description of material behaviour to be consistent within the framework of continuum mechanics, it is necessary that the stress rate used in the constitutive equation should be 'objective'. This condition requires that the stress rate must vanish identically under conditions of rigid body motion.

In a finite element analysis, it is desirable to calculate the Cauchy stress at each Gauss point as the calculation proceeds. The Cauchy stress rate, however, does not satisfy the condition of 'objectivity' as is illustrated by the following simple example.

Consider the prismatic rod shown in Figure 2.2 which is subjected to an axial force F.

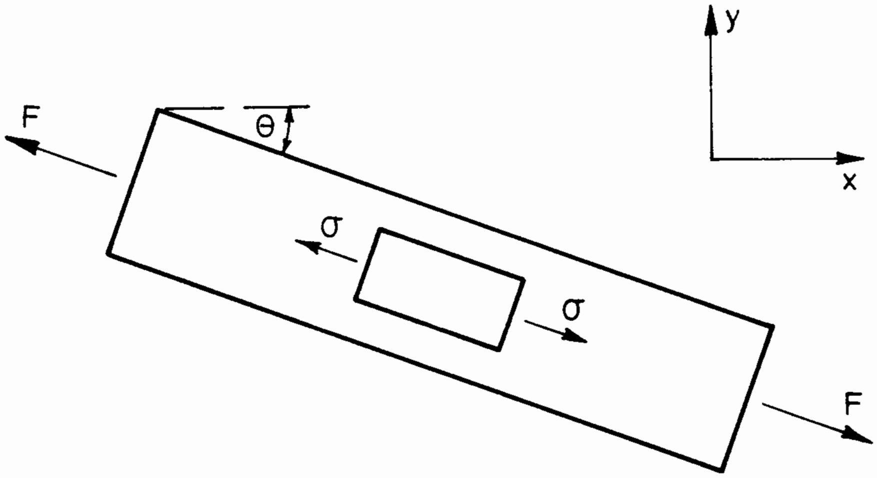

Figure 2.2: Rod Subjected to Axial Tension

The direct stress in the rod is:-

$$\sigma = \frac{F}{A} \tag{2.5}$$

where A is the cross sectional area. The components of Cauchy stress referred to the fixed co-ordinates x,y are:-

$$\sigma_{xx} = \frac{\sigma}{2} \left[1 + \cos(2\theta) \right] \tag{2.6}$$

$$\sigma_{yy} = \frac{\sigma}{2} \left[1 - \cos(2\theta) \right] \tag{2.7}$$

$$\tau_{xy} = \frac{-\sigma}{2} \sin(2\theta) \tag{2.8}$$

If the rod is subjected to a clockwise rotation rate ω with the force **F** kept constant, then the Cauchy stress rates obtained from the above equations are:-

$$\dot{\sigma}_{xx} = 2\, \tau_{xy}\, \omega \tag{2.9}$$

$$\dot{\sigma}_{yy} = -2\, \tau_{xy}\, \omega \tag{2.10}$$

$$\dot{\tau}_{xy} = (\sigma_{yy} - \sigma_{xx})\, \omega \tag{2.11}$$

Since these are not identically zero, it is clear that the Cauchy stress rates do not satisfy the conditions of 'objectivity'.

It may be shown (Prager (1961(a)) that the definition of 'objectivity' is not sufficiently restrictive to give a unique definition of stress rate. As a result, several different 'objective' stress rates appear in the literature, four of which are defined below:-

(a) Jaumann (1911) Stress Rate

$$\overset{\nabla}{\sigma}_{ij} = \dot{\sigma}_{ij} - \sigma_{ik}\, \omega_{jk} - \sigma_{jk}\, \omega_{ik} \tag{2.12}$$

The superior dot denotes the Cauchy stress rate, and ω_{ij} is the skew-symmetric spin tensor:-

$$\omega_{ij} = \frac{1}{2}\left[\frac{\partial u_i}{\partial x_j} - \frac{\partial u_j}{\partial x_i}\right] \tag{2.13}$$

(b) **Oldroyd (1950) Stress Rate**

$$\sigma'_{ij} = \dot{\sigma}_{ij} - \sigma_{ik}\frac{\partial u_j}{\partial x_k} - \sigma_{jk}\frac{\partial u_i}{\partial x_k} \tag{2.14}$$

(c) **Cotter and Rivlin (1955) Stress Rate**

$$\sigma''_{ij} = \dot{\sigma}_{ij} + \frac{\partial u_k}{\partial x_i}\sigma_{kj} + \frac{\partial u_k}{\partial x_j}\sigma_{ki} \tag{2.15}$$

(d) **Truesdell (1953) Stress Rate**

$$\sigma'''_{ij} = \dot{\sigma}_{ij} + \sigma_{ij}\frac{\partial u_k}{\partial x_k} - \sigma_{ik}\frac{\partial u_j}{\partial x_k} - \sigma_{jk}\frac{\partial u_i}{\partial x_k} \tag{2.16}$$

In recent years, the Jaumann definition has been almost universally adopted for use in large strain computations e.g. Eulerian finite element formulations of Osias and Swedlow (1974) and Carter (1977), and Lagrangian formulations by Hibbitt, Marcal and Rice (1970), Tseng and Lee (1985) and Taylor and Becker (1983). This popularity stems from the desirable feature of the Jaumann definition that vanishing of the stress rate implies stationary behaviour of the stress invariants, and therefore (for isotropic materials) stationary behaviour of the yield function. This condition is not satisfied by the other 'objective' stress rate definitions (Prager (1961a), (1961b)).

The Jaumann stress rate, however, suffers from the limitation that it can give rise to physically unrealistic solutions to problems in which large shear deformations occur. This effect is discussed at length by Dienes (1979), Johnson and Bammann (1984), Moss (1984) and Sowerby and Chu (1984), and may be illustrated by considering an initially rectangular element as it undergoes simple planar shear as shown in Figure 2.3.

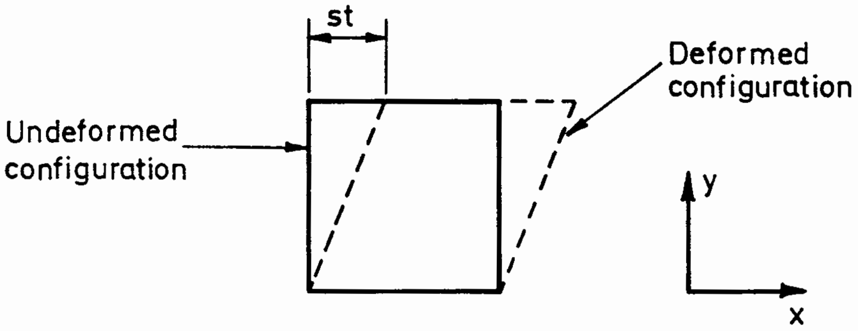

Figure 2.3: Simple Planar Shear

The deformation is described by the velocity field:-

$$u = s\,y \tag{2.17}$$

$$v = 0 \tag{2.18}$$

from which the instantaneous strain rates may be obtained (see Section 3.2):-

$$\dot{\epsilon}_{xx} = 0 \tag{2.19}$$

$$\dot{\epsilon}_{yy} = 0 \tag{2.20}$$

$$\dot{\gamma}_{xy} = s \tag{2.21}$$

$$\dot{e}_{xy} = \frac{s}{2} \tag{2.22}$$

The Jaumann stress rates are related to the instantaneous strain rates by the elastic rate equations giving the results:-

$$\overset{\nabla}{\sigma}_{xx} = \overset{\nabla}{\sigma}_{yy} = 0 \tag{2.23}$$

$$\overset{\nabla}{\tau}_{xy} = G\ s \tag{2.24}$$

The Cauchy stress rates derived from the definition of the Jaumann stress rate (equation (2.12)) are:-

$$\dot{\sigma}_{xx} = \tau_{xy}\ s \tag{2.25}$$

$$\dot{\sigma}_{yy} = -\tau_{xy}\ s \tag{2.26}$$

$$\dot{\tau}_{xy} = G\ s - \frac{s}{2}(\sigma_{xx} - \sigma_{yy}) \tag{2.27}$$

Equations (2.25), (2.26) and (2.27) may be integrated to give:-

$$\sigma_{xx} = \sigma_{xo} + \left[\frac{\sigma_{yo} - \sigma_{xo}}{2} + G\right]\left[1 - \cos(st)\right] + \tau_o \sin(st) \tag{2.28}$$

$$\sigma_{yy} = \sigma_{yo} - \left[\frac{\sigma_{yo} - \sigma_{xo}}{2} + G\right]\left[1 - \cos(st)\right] - \tau_o \sin(st) \tag{2.29}$$

$$\tau_{xy} = \tau_o \cos(st) + \left[\frac{\sigma_{yo} - \sigma_{xo}}{2} + G\right] \sin(st) \tag{2.30}$$

where σ_{xo}, σ_{yo} and τ_o are the initial values of σ_{xx}, σ_{yy} and τ_{xy}. For the case when initial stresses are zero, these equations reduce to those derived by Osias and Swedlow (1974).

The solution to the simple shear problem is periodic and therefore physically unrealistic for the case when shear deformations become very large. Dienes (1979) points out that this inconsistency arises from the fact that the rotational terms in the Jaumann definition are related to the vorticity of the velocity field rather than the true material rotation. In this same paper, Dienes proposes a modified form of the Jaumann stress rate in which the rotational terms are based on the true rotation rate, and uses this to perform a calculation equivalent to that described above. The solutions for the stresses in this case increase monotonically with time and are therefore more realistic than those derived using the Jaumann stress rate in its unmodified form. The two solutions are, to all intents and purposes, identical for the case when the shear strain is less than about unity, from which it may be inferred that the modification proposed by Dienes is only necessary when shear strains become very large.

In the finite element formulation described in this dissertation the original form of the Jaumann stress rate has been adopted, since the shear strains expected in the analysis are not sufficiently large to justify the additional complexity of the Dienes modification.

2.2.3 Element Stiffness Matrices

In an Eulerian formulation, it is possible to derive the element stiffness matrices in a way that retains much of the character of the equivalent small strain formulation, as illustrated below for the two-dimensional case.

If $\underset{\sim}{\dot{X}}$ is a vector of nodal velocities, then the strain rate vector $\underset{\sim}{\dot{\epsilon}}$ is obtained from an equation of the form:-

$$\underset{\sim}{\dot{\epsilon}} = [B]\, \underset{\sim}{\dot{X}} \tag{2.31}$$

where the [B] matrix is usually written in terms of a set of reference co-ordinates, which are related to the global co-ordinates by an iso-parametric mapping. The equation of virtual work (which is essentially an equilibrium equation) applied to a single element is:-

$$\underset{\sim}{P} = \iint_E [B]^T \underset{\sim}{\sigma} \;\det[J]\; d\alpha\; d\beta \tag{2.32}$$

where α, β are the reference co-ordinates, $\underset{\sim}{\sigma}$ is the stress vector consistent with the strain rate vector defined in equation (2.31), $\underset{\sim}{P}$ is the vector of consistent nodal forces and the integration is performed over the element. The Jacobian of the transformation from global to reference co-ordinates is [J].

Equation (2.32) may be differentiated to give the rate equation:-

$$\underset{\sim}{\dot{P}} = \iint_E \left\{ [B]^T \underset{\sim}{\dot{\sigma}} \det[J] \;+\; \left[[B]^{T^{\cdot}} \det[J] \right] \underset{\sim}{\sigma} \right\} d\alpha\; d\beta \tag{2.33}$$

Note that in this equation the superior dot associated with the second term in the integrand denotes the time derivative of the complete contents of the bracket. Equation (2.33) may be re-written:-

$$\dot{\underset{\sim}{P}} = \iint_E \left\{[B]^T [D] [B] \det[J] + [C]\right\} \dot{\underset{\sim}{X}} \, d\alpha \, d\beta \qquad (2.34)$$

where the material stiffness matrix [D] relates stress rate to strain rate:-

$$\dot{\underset{\sim}{\sigma}} = [D] \dot{\underset{\sim}{\epsilon}} \qquad (2.35)$$

and:-

$$[C] \dot{\underset{\sim}{X}} = ([B]^{T^{\cdot}} \det[J]) \underset{\sim}{\sigma} \qquad (2.36)$$

The stiffness equation, therefore, contains the conventional small displacement terms but additional terms are present, in the form of the [C] (distortion rate) matrix, that account for the rate of change of element geometry. For the case of continuum elements, the [C] matrix must be obtained by expanding the expression in equation (2.36) whereas for one dimensional elements a somewhat simpler method based on a modified material stiffness matrix may be adopted (see Chapters 3 and 5). The distortion rate matrix is non-symmetrical, which is a factor that needs to be considered in selecting a suitable algorithm to invert the global stiffness matrix.

2.2.4 Effect of Mesh Distortion

The mesh distortion that occurs during a large strain finite element analysis can seriously reduce the accuracy of the calculation. Since it is generally this effect that limits the displacements that can be accurately modelled by a given finite element formulation, it is necessary firstly to be able to detect errors of this sort and secondly to develop means by which this difficulty can be avoided.

The source of the error that arises as the mesh becomes distorted is the calculation of the element stiffness matrices. The stiffness matrix is derived from equation (2.34) and is given by:-

$$[K] = \iint_E \left\{ [B]^T [D] [B] \det[J] + [C] \right\} d\alpha \, d\beta \tag{2.37}$$

The elements of the [B] and [C] matrices are of the form:-

$$b_{ij} = \frac{f(\alpha, \beta)}{\det[J]} \qquad c_{ij} = h(\alpha, \beta, \sigma_{kl}) \tag{2.38}$$

where f and h are polynomial functions of α and β determined by the element shape functions, and σ_{kl} are the elements of the Cauchy stress tensor. Equation (2.37) is invariably evaluated using a Gaussian quadrature procedure in which the number of sampling points required for 'exact' integration is determined on the basis that det[J] is constant over the element which is only the case if the element sides are straight and the edge nodes lie at their prescribed positions on the element sides. As soon as the element becomes distorted, the value of det[J] ceases to be constant and the integrand of equation (2.37) is no longer a rational polynomial, which means that errors occur in the numerical integration. It should be noted that these errors in the evaluation of the element stiffness matrices are associated with element distortions, and are not affected by element aspect ratio*.

The errors associated with element distortion may be detected by inspecting the variation of det[J] over each element as the calculation proceeds. These variations may be quantified by considering the standard deviation of det[J]. A Jacobian variation parameter, ψ, may therefore be derived:-

$$\psi = \left[\frac{\iint_E \left[\det[J] - \overline{\det[J]} \right]^2 d\alpha\, d\beta}{\left(\overline{\det[J]} \right)^2} \right]^{1/2} \qquad (2.39)$$

where:-

$$\overline{\det[J]} = \frac{\iint_E \det[J]\, d\alpha\, d\beta}{\iint_E d\alpha\, d\beta} \qquad (2.40)$$

and the integrations are performed over the element. This Jacobian variation parameter can be checked for each element during the finite element analysis to ensure that the accuracy of the calculation of the element stiffness matrices remains within acceptable bounds.

---

* It is often cited that element aspect ratios should be kept as near unity as possible when preparing a finite element mesh. The above argument, however, shows that aspect ratio has no effect on the accuracy of the calculation of the element stiffness matrix. It is, of course, generally desirable that aspect ratios should be kept small to avoid the danger of ill-conditioning.

If an element becomes severely distorted during the calculation, it is necessary to stop the analysis since all subsequent results will be in doubt. This difficulty may then be dealt with either by refining the mesh in the region of distortion or by using a higher order quadrature rule for those elements that tend to become heavily deformed. This latter approach is to be preferred in any practical situation, and leads to the concept of 'over-integrating' those elements in the finite element mesh that are known to become heavily distorted during the calculation. A procedure of this sort is described by Cook (1981).

It is possible, in principle, to deal with the problem of mesh distortion by refining the mesh during the course of the analysis. In this sort of procedure, however, it is necessary to extrapolate the Gauss point stresses in order to obtain the stresses in the updated mesh. It is well known that this type of calculation is difficult and imprecise, so this procedure has not been attempted in the calculations described in this thesis.

2.3 Analysis of Incompressible Materials

It is well accepted that severe numerical difficulties arise when using the conventional displacement method to analyse incompressible, or near incompressible materials. These difficulties are caused by the additional kinematic constraints imposed on the nodal velocities by the incompressibility condition which reduce the number of free degrees-of-freedom in the finite element mesh. A particularly full analysis of this effect is presented by Sloan (1981). Since many of the common elasto-plastic constitutive laws used in Soil Mechanics require that incompressibility is satisfied throughout the material in the plastic regime, calculations in which incompressibility effects occur have considerable practical importance, and have been the subject of much research.

The effect of incompressibility constraints depends on the type of calculation being performed. In a collapse load calculation the effect of these additional kinematic constraints is to produce an over-stiff response. In these circumstances the finite element solution often severely overestimates the limit load, or in extreme cases exhibits no limit load at all (Nagtegaal et al. (1974), Sloan and Randolph (1982), Sloan (1981)). The alternative type of analysis is one in which the stresses at the Gauss points are calculated. In computations of this sort, the effect of incompressibility constraints is to produce a large scatter in the results. This effect has been illustrated by a series of numerical experiments performed by Naylor (1974) involving small strain analyses of a thick cylinder under internal pressure. The results show that when eight-noded quadrilateral elements are used with a nine-point integration rule, then as perfect incompressibility is reached a reduction of stress accuracy occurs that takes the form of stress oscillations across the element. Naylor shows that these inaccuracies are confined to the mean stress terms, with the deviatoric stresses determined accurately as perfect incompressibility is reached. A further discussion of the effects of incompressible material behaviour on the results of thick cylinder calculations is included in Section 6.7 of this thesis.

Four methods of dealing with the detrimental effect of incompressibility constraints may be identified, and these are described below.

A general approach that has been the subject of much previous research is to modify the original displacement method in such a way as to reduce the effects of these constraints. One possibility is to use a lower order of numerical integration in the evaluation of the element stiffness matrices than is required for exact integration*. This is the so-called 'reduced-integration' technique (Zienkiewicz (1977)). The effectiveness of using the eight-noded quadrilateral element with four Gauss points is often cited as an example of this advantages of this method ((Naylor (1974), Prevost and Hughes (1981)). A number of researchers have investigated a variant of the 'reduced-integration' approach in which different geometric expansions are used for the volumetric and deviatoric strain terms (Nagtegaal et al. (1974), Malkus (1976), Hinton et al. (1978), Marti and Cundall (1982)). This approach is described as 'selective-integration'.

It may be shown that a formulation based on 'reduced' or 'selective' integration is equivalent to a mixed method, i.e. an approach in which the primary variables are not of the same type (Hughes (1977), Malkus and Hughes (1978), Shimodaira (1985)). Although this formalizes the procedure, this cannot be used as an argument for the general suitability of these integration rules, since in any mixed method the possibility exists of element instability.

The hybrid method is a form of mixed method in which both stresses and displacements are used as primary variables (Pian (1973), Pian and Lee (1976), Spilker (1981)). There is some evidence to suggest that this type

---

* Exact integration in this context refers to the case when the Jacobian is constant across the element.

of formulation has several advantages over the conventional displacement approach, especially for the analysis of incompressible materials.

An alternative way of dealing with incompressibility constraints is described by Sloan and Randolph (1982) who show that as the order of an element is increased, the number of degrees-of-freedom per element increases faster than the number of incompressibility constraints. This work suggests that if the total number of degrees-of-freedom in a finite element mesh are held constant, then the total number of constraints can be reduced by using higher order elements. A satisfactory finite element solution should, therefore, be possible without having to resort to the use of 'reduced-integration'. This hypothesis was checked and confirmed by Sloan (1981) who performed a series of small strain collapse load calculations using fifteen-noded triangular elements.

A third approach to the problem of incompressibility constraints is based on the simple argument that the quality of a finite element solution is related to the difference between the number of degrees-of-freedom in the mesh and the number of incompressibility constraints. If element types are chosen for which the total number of degrees-of-freedom increases more rapidly than the number of incompressibility constraints as the mesh is refined, then solutions can always be improved simply by introducing more elements into the finite element mesh. According to Sloan (1981), the lowest order of triangular element suitable for this approach is linear strain for plane strain problems and cubic strain for the axi-symmetric case. Quadrilateral elements are less attractive with a minimum of a seventeen-noded element being necessary for 'full-integration' plane strain calculations.

A further effect that can be used to advantage, but has received little attention in the past, is that the number of incompressibility constraints may be reduced by using special arrangements of elements (Rice et al. (1979)). An example of this effect is discussed by Nagtegaal et al. (1974) in which four constant strain triangles are coalesced to form a quadrilateral and the total number of incompressibility constraints are shown to be three rather than four, the sum of the incompressibility constraints of the individual elements. This effect also occurs for the case of linear strain triangles as is illustrated by the series of thick cylinder test problems described in Section 6.7. An analysis of this effect for the six-noded triangle is given by Mercier (1979). Since the beneficial effect of these special arrangements is generally lost as the elements become distorted, the use of this approach is strictly limited to small displacement calculations, or those large displacement calculations in which the element shape is retained as the analysis proceeds. An example of this latter type of calculation is the cavity expansion analysis described in Section 6.8 in which quadrilateral 'super-elements' are used with considerable advantage.

In the finite element calculations described in this thesis, the third approach described above has generally been adopted, and the formulation has been based on the six-noded triangle which is the simplest element for which this philosophy is valid. The use of higher order elements would undoubtedly improve the efficiency of the formulation but this would be at the expense of considerable additional mathematical complexity.

The formulation described in this thesis is based on a displacement approach in which an iso-parametric method is used to derive the finite element equations. This type of approach has been adopted in favour of the more recently developed formulations (e.g. mixed and hybrid methods) since the displacement method has already been applied extensively to problems in geomechanics, and is therefore a suitable starting point for the development of a large strain finite element theory. It is argued in Section 2.2.4 that is is necessary to 'over-integrate' those elements that become severely distorted during the analysis. The use of 'reduced-integration' has therefore been avoided since it is undesirable to use elements for which the order of integration is critical.

2.4 Solution Schemes

In a finite element analysis where material and/or geometric non-linearities are present, it is necessary to choose a suitable algorithm for the solution of the resulting non-linear equations. Finite element analyses of this sort are invariably performed in a step-by-step fashion, and the purpose of the solution scheme is to ensure that equilibrium is approximately satisfied at the end of each increment. A good review of

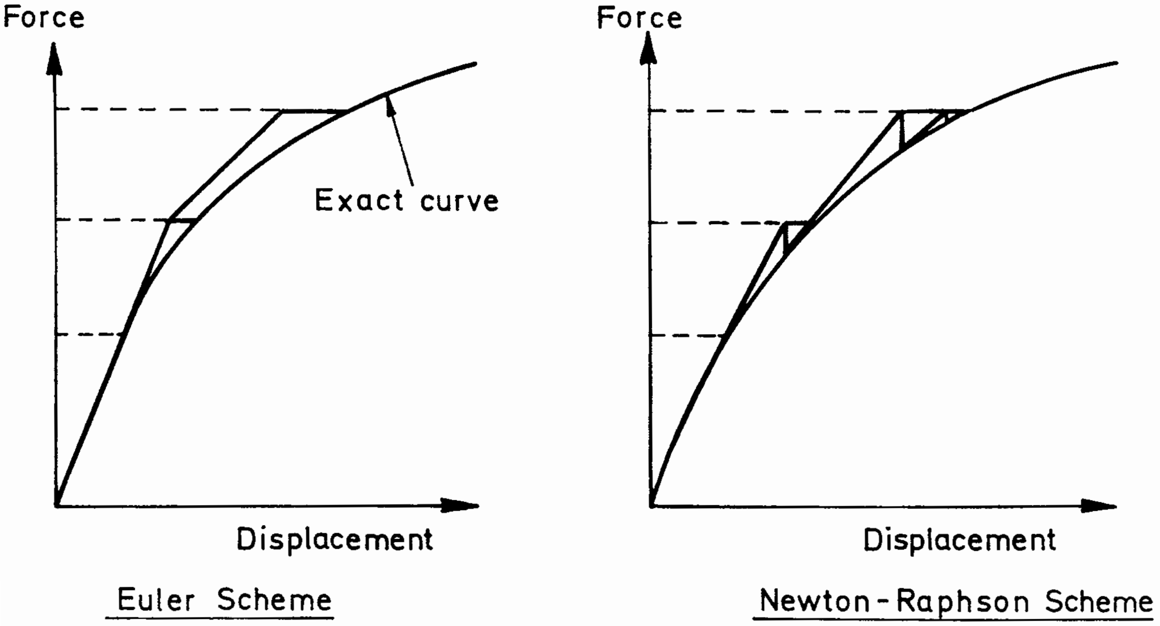

Figure 2.4: Solution Schemes

solution schemes of this sort is given by Stricklin and Haisler (1977).

Non-linear solution schemes can be divided into two broad groups which are illustrated in Figure 2.4 for the case of a single degree-of-freedom problem.

The simplest solution algorithm is the Euler scheme in which the exact curve is approximated by a series of straight lines having a slope equal to that of the exact curve at the start of the increment. This algorithm is described by Mondkar and Powell (1978) as a 'Step-by-Step Method'. The basic scheme may be improved by using the slope of the exact curve at the mid-point of the increment rather than at the start, with an iterative procedure being used to locate the mid-point. This latter procedure has been used by Carter (1977) in a series of large strain calculations. Another possibility is to retain the basic Euler scheme, but to provide an equilibrium check at the end of the increment and introduce a correction procedure. This type of scheme is described by Sloan (1981) as 'Modified Euler' and by Mondkar and Powell (1978) as 'Step-by-Step with Error Correction'.

An alternative to the Euler based schemes is the Newton-Raphson set of algorithms, the basic form of which is also illustrated in Figure 2.4. An approximation to the exact curve is again made based on the slope at the start of the increment but the approximation is then refined using an iterative procedure in which the stiffness is updated at each iteration. This scheme has the disadvantage for finite element calculations that the global stiffness matrix needs to be re-formed and inverted at each iteration which could lead to excessive computer time. A possible refinement is to use the stiffness matrix calculated at the start of the increment for all the iterations within that increment, a procedure described as 'Modified Newton-Raphson' (Sloan (1981)) or 'Initial Stress' (Thomas (1984)), Nayak and Zienkiewicz (1972)). A scheme of this sort has been adopted for large displacement finite element analyses by Zeevaert (1980).

The choice of solution scheme for a non-linear finite element formulation depends on the type of non-linearities present and the available computational facilities. For the large strain formulation described in this thesis the Modified Euler Scheme has been adopted, partly because it tends to be more robust than the Newton-Raphson scheme and partly because this algorithm has been shown to be efficient for the solution of small strain collapse problems (Sloan (1981)).

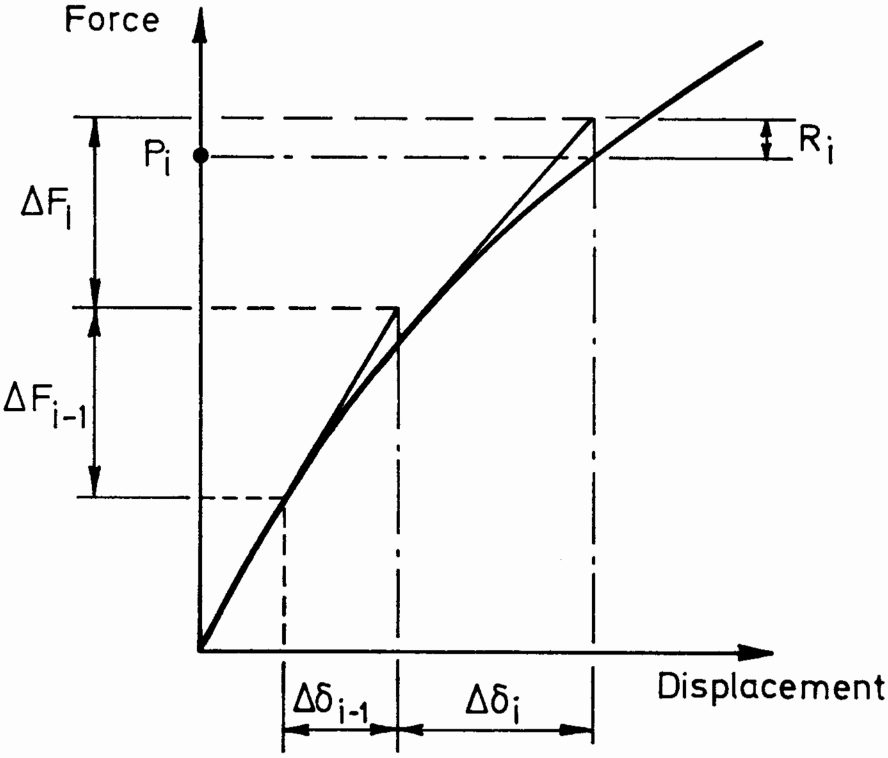

Figure 2.5: Modified Euler Scheme

The particular form of the Modified Euler Scheme used to obtain all of the finite element solutions presented in this dissertation is illustrated diagrammatically in Figure 2.5, again with reference to a single degree-of-freedom system.

At the start of the i^{th} load step, the individual element stiffness matrices are calculated, and then assembled and inverted using a Frontal solution algorithm to give a set of incremental nodal displacements $\Delta\delta_i$. The next stage is to calculate a set of stress increments $\Delta\underset{\sim}{\sigma}$ at each Gauss point, corresponding to the set of incremental nodal displacements $\Delta\delta_i$. The stress increments are obtained by performing an integration of the form:-

$$\Delta\underset{\sim}{\sigma} = \int_{t}^{t+\Delta t} [D]\, \dot{\underset{\sim}{\epsilon}}\, dt \qquad (2.41)$$

where [D] is the material stiffness matrix relating stress rate to strain rate, and $\dot{\underset{\sim}{\epsilon}}$ is a strain rate vector which, when integrated over the time step, is compatible with the incremental nodal displacements $\Delta\delta_i$. The increment begins at time t, and ends at time t + Δt. In general, a numerical integration scheme must be used to evaluate equation (2.41) but in some cases a closed form solution can be obtained and this is clearly preferable. A full description of these 'stress update' calculations is given in Chapter 4 for the continuum elements and Section 5.4 for the membrane elements. The final step in the solution scheme is to calculate the nodal loads equivalent to the updated stresses at the updated geometry, denoted by P_i in Figure 2.5. These forces are calculated from the virtual work expression given in equation (2.32). A set of unbalanced nodal loads

(R_i in Figure 2.5) are then calculated and then applied as an equilibrium correction during the next load increment.

A feature of the scheme described above is that the accuracy of the calculation is relatively insensitive to errors in the calculation of the element stiffness matrix. It is, however, vital that the equilibrium check be performed accurately.

2.5 Summary

The Lagrangian or the Eulerian description of the kinematics of deformation may be used as the basis of a large displacement finite element formulation. Although the Eulerian approach is currently the less popular of the two, it is well suited to the analysis of problems in Soil Mechanics and as such has been adopted in the formulation described in this dissertation.

For a mathematical model of material behaviour to be consistent within the theory of continuum mechanics it is necessary that an 'objective' stress rate be used in the constitutive equation. A variety of suitable stress rates have been proposed, but the most widely used is the Jaumann definition, which has been adopted in this thesis despite the fact that it can lead to physically unrealistic behaviour when shear strains are very large.

The analysis of the reinforced unpaved road requires the numerical modelling of the behaviour of undrained clay, which is incompressible. Numerical difficulties can arise in the analysis of materials of this sort due to the additional kinematic constraints imposed on the nodal velocities by the incompressibility condition. In all of the calculations described in this thesis, the six-noded triangular element has been used to model the continuum. This element may be shown to be suitable for the analysis of incompressible materials in plane strain.

Mesh distortion can lead to severe accuracy reductions in a large displacement finite element calculation. This may be dealt with by 'over-integrating' those elements that are known to become heavily distorted during the analysis.

CHAPTER 3 FORMULATION OF CONTINUUM ELEMENTS

3.1 Introduction

A large displacement finite element formulation for two-dimensional plane strain continuum elements is described in this chapter. The kinematics of deformation have been based on an Eulerian description and the Jaumann stress rate is used in the constitutive equation to satisfy the requirements of objectivity. The formulation is restricted to materials that are elastic perfectly-plastic with constant elastic parameters.

This formulation is applicable to iso-parametric triangular elements of arbitrary order, and has therefore been presented in a general form. Since the six-noded triangle has been used to model the continuum in all of the calculations described in this dissertation, the specific finite element equations for this particular element have been included in an appendix.

3.2 Stress and Strain Definitions

In an Eulerian approach, the kinematics of deformation may be described by strain rates which are defined in the same way as for the infinitesimal theory. This type of formulation, therefore, has the desirable feature that some aspects of the character of the small strain theory are preserved for the general case that the total deformation is finite.

Strain rates and the clockwise rotation rate are defined:-

$$\dot{\epsilon}_{xx} = \frac{\partial u}{\partial x} \tag{3.1}$$

$$\dot{\epsilon}_{yy} = \frac{\partial v}{\partial y} \tag{3.2}$$

$$\dot{\gamma}_{xy} = \frac{\partial u}{\partial y} + \frac{\partial v}{\partial x} \tag{3.3}$$

$$\dot{\theta}_{xy} = \frac{1}{2}\left[\frac{\partial u}{\partial y} - \frac{\partial v}{\partial x} \right] \tag{3.4}$$

where the velocities in the x and y directions are given by u, v. The corresponding Jaumann stress rates from equation (2.12) are:-

$$\overset{\nabla}{\sigma}_{xx} = \dot{\sigma}_{xx} - 2\tau_{xy}\dot{\theta}_{xy} \tag{3.5}$$

$$\overset{\nabla}{\sigma}_{yy} = \dot{\sigma}_{yy} + 2\tau_{xy}\dot{\theta}_{xy} \tag{3.6}$$

$$\overset{\nabla}{\sigma}_{zz} = \dot{\sigma}_{zz} \tag{3.7}$$

$$\overset{\nabla}{\tau}_{xy} = \dot{\tau}_{xy} + \dot{\theta}_{xy}(\sigma_{xx} - \sigma_{yy}) \tag{3.8}$$

The superior dot denotes the time derivative with respect to a set of stationary Cartesian axes.

3.3 Formulation of the Element Stiffness Matrix

The formulation of the element stiffness matrix is based on the iso-parametric method which is often used in the derivation of small strain finite element equations (Zienkiewicz (1979)). The usual small displacement theory is modified in this formulation to include the effects of large distortion and large rotation, and follows the general approach described in Section 2.2.3. In the derivation of this theory, the global Cartesian co-ordinates describing a point in the element are x, y and the fixed reference co-ordinates are α, β.

The vector of global co-ordinates of a typical point in the element, $\underset{\sim}{x}$, is related to the vector of global nodal co-ordinates, $\underset{\sim}{X}$, by:-

$$\underset{\sim}{x} = [N]\,\underset{\sim}{X} \tag{3.9}$$

where [N], the shape function matrix, is a function of α and β. The strain rate vector $\underset{\sim}{\dot{\epsilon}}$ is defined:-

$$\underset{\sim}{\dot{\epsilon}} = \begin{Bmatrix} \dot{\epsilon}_{xx} \\ \dot{\epsilon}_{yy} \\ \dot{\epsilon}_{zz} \\ \dot{\gamma}_{xy} \\ 2\dot{\theta}_{xy} \end{Bmatrix} \tag{3.10}$$

$$= [L]\,[N]\,\underset{\sim}{\dot{X}} \tag{3.11}$$

$$= [B]\,\underset{\sim}{\dot{X}} \tag{3.12}$$

where [L] is the operator matrix:-

$$[L] = \begin{bmatrix} \frac{\partial}{\partial x} & 0 \\ 0 & \frac{\partial}{\partial y} \\ 0 & 0 \\ \frac{\partial}{\partial y} & \frac{\partial}{\partial x} \\ \frac{\partial}{\partial y} & -\frac{\partial}{\partial x} \end{bmatrix} \qquad (3.13)$$

and $\dot{\underset{\sim}{x}}$ is the vector of global nodal velocities. Note that the strain rate vector includes the rotation rate as well as the strain rates. This proves to be a convenient way of including the Jaumann terms in equations (3.5),(3.6) and (3.8).

The Cauchy stress rate vector, $\dot{\underset{\sim}{\sigma}}$ is defined:-

$$\dot{\underset{\sim}{\sigma}} = \begin{bmatrix} \dot{\sigma}_{xx} \\ \dot{\sigma}_{yy} \\ \dot{\sigma}_{zz} \\ \dot{\tau}_{xy} \\ 0 \end{bmatrix} \qquad (3.14)$$

This stress rate vector is energetically conjugate to the strain rate vector defined in equation (3.10) (note the zero entry in the position corresponding to the rotation rate term in the strain rate vector).

The total strain rate may be decomposed into elastic and plastic components in the same way as for the infinitesimal theory:-

$$\underset{\sim}{\dot{\epsilon}} = \underset{\sim}{\dot{\epsilon}}^{e} + \underset{\sim}{\dot{\epsilon}}^{p} \tag{3.15}$$

where $\underset{\sim}{\dot{\epsilon}}^{e}$ is the elastic component, and $\underset{\sim}{\dot{\epsilon}}^{p}$ the plastic component. The Jaumann stress rate is related to the elastic strain rate by:-

$$\underset{\sim}{\overset{\nabla}{\sigma}} = [D]^{e}\, \underset{\sim}{\dot{\epsilon}}^{e} \tag{3.16}$$

where $[D]^{e}$ is the elastic material incremental stiffness matrix:-

$$[D]^{e} = \begin{bmatrix} K + \frac{4G}{3} & K - \frac{2G}{3} & K - \frac{2G}{3} & 0 & 0 \\ K - \frac{2G}{3} & K + \frac{4G}{3} & K - \frac{2G}{3} & 0 & 0 \\ K - \frac{2G}{3} & K - \frac{2G}{3} & K + \frac{4G}{3} & 0 & 0 \\ 0 & 0 & 0 & G & 0 \\ 0 & 0 & 0 & 0 & 0 \end{bmatrix} \tag{3.17}$$

The plastic strain rates are derived from the plastic potential $g(\underset{\sim}{\sigma})$:-

$$\underset{\sim}{\dot{\epsilon}}^{p} = \lambda \frac{\partial g}{\partial \underset{\sim}{\sigma}} \tag{3.18}$$

where λ is a scalar multiplier.

If $f(\underset{\sim}{\sigma}) = 0$ is the yield function then:-

$$\left[\frac{\partial f}{\partial \underset{\sim}{\sigma}}\right]^{T} \underset{\sim}{\overset{\nabla}{\sigma}} = 0 \tag{3.19}$$

Substituting equations (3.15),(3.16) and (3.18) into the above expression gives:-

$$\left[\frac{\partial f}{\partial \underset{\sim}{\sigma}}\right]^{T} \left[\; [D]^{e} \left\{ \dot{\underset{\sim}{\epsilon}} - \lambda \frac{\partial g}{\partial \underset{\sim}{\sigma}} \right\} \right] = 0 \qquad (3.20)$$

and:-

$$\lambda = \frac{\left[\frac{\partial f}{\partial \underset{\sim}{\sigma}}\right]^{T} [D]^{e} \; \dot{\underset{\sim}{\epsilon}}}{\left[\frac{\partial f}{\partial \underset{\sim}{\sigma}}\right]^{T} [D]^{e} \; \frac{\partial g}{\partial \underset{\sim}{\sigma}}} \qquad (3.21)$$

Equations (3.15),(3.16) and (3.18) may be used to derive a relationship between the Jaumann stress rate and the total strain rate:-

$$\overset{\nabla}{\underset{\sim}{\sigma}} = \left[\; [D]^{e} + [D]^{p} \; \right] \dot{\underset{\sim}{\epsilon}} \qquad (3.22)$$

$$= [D]^{ep} \; \dot{\underset{\sim}{\epsilon}} \qquad (3.23)$$

If the Gauss point stress lies on the yield surface, then the plastic stiffness matrix, $[D]^{p}$, is given by:-

$$[D]^{p} = \frac{-[D]^{e} \left[\frac{\partial g}{\partial \underset{\sim}{\sigma}}\right] \left[\frac{\partial f}{\partial \underset{\sim}{\sigma}}\right]^{T} [D]^{e}}{\left[\frac{\partial f}{\partial \underset{\sim}{\sigma}}\right]^{T} [D]^{e} \left[\frac{\partial g}{\partial \underset{\sim}{\sigma}}\right]} \qquad (3.24)$$

If the stress point lies inside the yield surface then $[D]^{p}$ is set to zero on the basis that the plastic strain rates are zero.

The rotation terms of equations (3.5), (3.6) and (3.8) may now be included in equation (3.23) to give an expression for the Cauchy stress rate:-

$$\dot{\underset{\sim}{\sigma}} = \left[\; [D]^{ep} + [R] \; \right] \dot{\underset{\sim}{\epsilon}} \qquad (3.25)$$

where [R] is the matrix:-

$$[R] \quad = \quad \begin{bmatrix} 0 & 0 & 0 & 0 & \tau_{xy} \\ 0 & 0 & 0 & 0 & -\tau_{xy} \\ 0 & 0 & 0 & 0 & 0 \\ 0 & 0 & 0 & 0 & \frac{1}{2}\left[\sigma_{yy} - \sigma_{xx}\right] \\ 0 & 0 & 0 & 0 & 0 \end{bmatrix} \tag{3.26}$$

Combining equations (3.12) and (3.25) gives:-

$$\underset{\sim}{\dot{\sigma}} = \Big[\, [D]^{ep} + [R] \, \Big] \, [B] \, \underset{\sim}{\dot{X}} \tag{3.27}$$

The principal of virtual work may now be used to obtain a set of nodal forces, $\underset{\sim}{P}$, that are consistent with the internal stresses in the element:-

$$\underset{\sim}{P} = \iint_E [B]^T \underset{\sim}{\sigma} \det[J] \, d\alpha \, d\beta \tag{3.28}$$

where [J] is the Jacobian of the transformation from global to reference co-ordinates.

Equation (3.28) may be differentiated to give an equation for the nodal force rates as described in Section 2.2.3 (see equation (2.34)). Substituting the expression for Cauchy stress rate (equation (3.27)) into equation (2.34) gives:-

$$\underset{\sim}{\dot{P}} = \iint_E [B]^T \Big[\, [D]^{ep} + [R] \, \Big] \, [B] \, \underset{\sim}{\dot{X}} \det[J] \, d\alpha \, d\beta \; + \; \iint_E [C] \, \dot{X} \; d\alpha \, d\beta \tag{3.29}$$

In order to evaluate the [C] (distortion rate) matrix, it is necessary to expand equation (2.36) on a term-by-term basis. The resulting matrix for the six-noded triangle is given in Appendix 3A, along with the other finite element equations for this particular element.

The incremental element stiffness matrix is thus:-

$$[K] = \iint_E [B]^T \Big[[D]^{ep} + [R] \Big] [B] \det[J] \, d\alpha \, d\beta + \iint_E [C] \, d\alpha \, d\beta \qquad (3.30)$$

This form of the stiffness matrix is similar to that derived from infinitesimal theory, but with the addition of the matrix [R] to deal with the effects of rotation, and the matrix [C] to deal with large distortion effects.

In finite element computer codes, the stiffness matrix is invariably calculated using a Gaussian quadrature scheme. In selecting the form of integration algorithm to be used, careful consideration needs to be given to the detrimental effects that element distortion can have on the accuracy of the calculation. Gaussian integration schemes are only exact if the determinant of the Jacobian is constant, thus the effect of mesh distortion is to introduce errors into the calculation of the element stiffness matrices (see Section 2.2.4).

In the calculations described in this thesis, the distortions of each element are monitored at each stage of the analysis using the parameter ψ, defined by equation (2.39), which is a measure of the variation in the determinant of the Jacobian matrix over the element. For those elements for which distortions are low (i.e. $\psi < 0.1$) a three-point Gauss rule, corresponding to 'exact' integration if the Jacobian is constant, is used to evaluate equation (3.30). A thirteen-point rule is used to integrate those elements that are known to become more severely distorted during the analysis.

3.4 Material Self-Weight

The effects of material self-weight are included in this formulation by first specifying the self-weight stresses (including the in-situ lateral stresses) at each Gauss point in the mesh. A set of consistent nodal loads are then calculated using the virtual work principal (equation (3.28)), and these are applied to the nodes at the start of the analysis.

3.5 Constitutive Laws

Two separate constitutive laws are required to model the behaviour of clay and sand in the finite element formulation. Since the main emphasis in this thesis is the exact modelling of large strain effects, the constitutive laws have been kept deliberately simple to avoid undue mathematical complexity in the formulation.

Ideal elastic perfectly-plastic behaviour has been adopted for both soil types. The fill material is assumed to be sufficiently permeable for zero pore pressures to occur during the loading in which case the 'total' and 'effective' stresses are identical. A 'total stress' approach is adopted for the clay on the assumption that the loading on the subgrade is sufficiently fast to give an undrained response.

The constitutive laws used in this thesis are derived on the basis that elastic moduli remain constant during the deformation. Although this is a convenient idealization, the use of variable elastic moduli could lead to a more accurate description of the material behaviour (especially for the sand). In deriving a theory in which elastic moduli are not constant, however, it is necessary to use a rigorous thermo-mechanical approach to ensure that the derived material behaviour is conservative. A theory of this sort has been developed for infinitesimal strains (Houlsby (1985)), but this is not readily generalized to include finite rotation effects.

The most common constitutive laws used in finite element models to represent cohesive and frictional soils are the Tresca and Mohr-Coulomb models (e.g Griffiths (1982), Sloan (1981)). These constitutive laws, however, contain discontinuous yield surfaces with 'edges' at which the yield function is not differentiable. Although these singularities are not often approached for plane strain conditions, they are important for a number of problems involving axi-symmetric loading (Sloan (1981)). These singularities are usually dealt with by 'rounding off' the corners of the yield function which, although effective, is mathematically inconvenient.

In the formulation described in this thesis, cohesive soil is modelled by the von Mises yield criterion, and the Matsuoka yield function (Matsuoka(1976)) is used as the basis of a plasticity model to represent the frictional material. Both of these constitutive laws have the advantage over the Tresca and Mohr-Coulomb models that they are everywhere differentiable (except at the origin for the case of the Matsuoka yield function). The relationship between these two sets of yield functions is illustrated in Figure 3.1 which shows sections through the yield loci in the 'π' plane for the special case that they coincide at the 'corners' of the Tresca and Mohr-Coulomb surfaces.

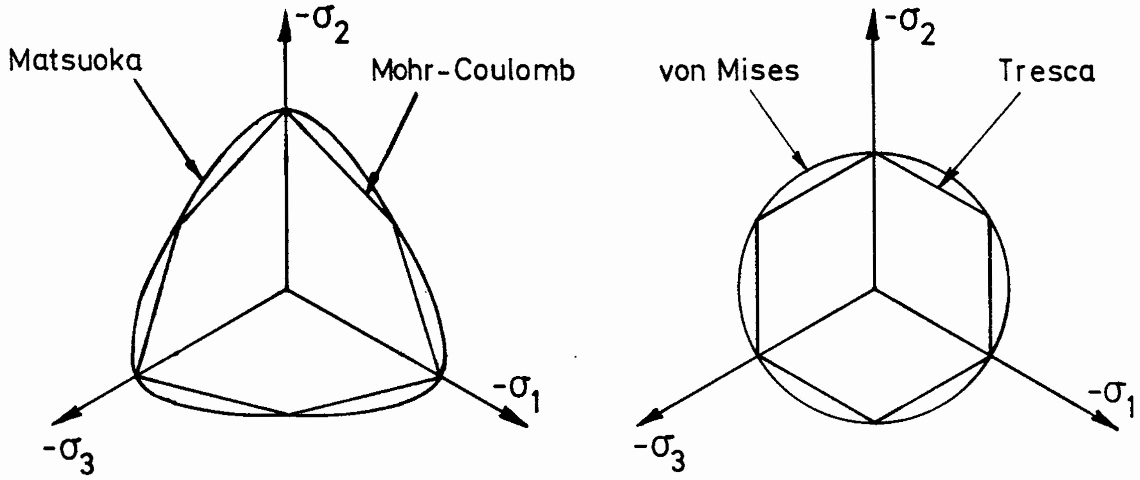

Figure 3.1: Comparison Between Yield Surfaces

In order to compare the results of plane strain analyses based on these two sets of constitutive laws, it is necessary to find correlations between the material properties used in the corresponding models. The plane strain cohesion, c_{ps}, and plane strain friction angle, ϕ_{ps}, will be used to obtain these relationships, and these are defined:-

$$c_{ps} = \frac{\sigma_1 - \sigma_3}{2} \tag{3.31}$$

$$\tan^2(\phi_{ps}) = \frac{(\sigma_1 - \sigma_3)^2}{4\sigma_1\sigma_3} \tag{3.32}$$

where σ_1 and σ_3 are the major and minor in-plane principal stresses respectively. In this section, values of c_{ps} and ϕ_{ps} defined above are related to the equivalent values of triaxial compression shear strength, c, and friction angle, ϕ, that are used in the von Mises and Matsuoka models. In deriving these relationships, which are restricted to the case of plane strain loading, two separate conventions are used. The stresses in a Cartesian frame are denoted σ_{xx}, σ_{yy}, σ_{zz} and τ_{xy}, where z is the out-of-plane direction, and the principal stresses are denoted σ_1, σ_2 and σ_3 where σ_2 again denotes the out-of-plane stress.

3.5.1 von Mises Plasticity

The von Mises yield function is defined as:-

$$f(\underset{\sim}{\sigma}) = (\sigma_{yy}- \sigma_{zz})^2 + (\sigma_{xx}- \sigma_{zz})^2 + (\sigma_{xx}- \sigma_{yy})^2 + 6\tau_{xy}^2 - 8c^2 \tag{3.33}$$

where c is the shear strength of the material in triaxial compression. An alternative form of the equation is:-

$$f(\underset{\sim}{\sigma}) \quad = \quad -6I_2' \; - \; 8c^2 \tag{3.34}$$

where I_2' is the second invariant of the deviatoric stresses.

The plastic strain rates are derived from an associated flow rule which gives zero plastic dilation rate and is therefore suitable for the analysis of undrained clay. In equation (3.24), therefore, $g(\underset{\sim}{\sigma}) = f(\underset{\sim}{\sigma})$ and the plastic material stiffness matrix is given by:-

$$[D]^p = \frac{-3G}{4c^2}\begin{bmatrix} (\sigma'_{xx})^2 & \sigma'_{xx}\,\sigma'_{yy} & \sigma'_{xx}\,\sigma'_{zz} & \sigma'_{xx}\,\tau_{xy} & 0 \\ \sigma'_{yy}\,\sigma'_{xx} & (\sigma'_{yy})^2 & \sigma'_{yy}\,\sigma'_{zz} & \sigma'_{yy}\,\tau_{xy} & 0 \\ \sigma'_{zz}\,\sigma'_{xx} & \sigma'_{zz}\,\sigma'_{yy} & (\sigma'_{zz})^2 & \sigma'_{zz}\,\tau_{xy} & 0 \\ \tau_{xy}\,\sigma'_{xx} & \tau_{xy}\,\sigma'_{yy} & \tau_{xy}\,\sigma'_{zz} & \tau_{xy}^2 & 0 \\ 0 & 0 & 0 & 0 & 0 \end{bmatrix} \qquad (3.35)$$

where the primes denote deviatoric stresses.

The associated flow rule may be used to show that, in the limit that the elastic strain rates are negligible in comparison with the plastic strain rates, then the principal stresses are related by:-

$$\sigma_2 = \frac{(\sigma_1 + \sigma_3)}{2} \qquad (3.36)$$

If a Poisson's ratio of approximately 0.5 is chosen, then the strain rates will be predominately plastic after the initial onset of yield. For this case, the von Mises yield function reduces to:-

$$(\sigma_1 - \sigma_3) = \frac{16c^2}{3} \qquad (3.37)$$

which may be combined with equation (3.31) to give a relationship between the triaxial compression shear strength, c, and the plane strain shear strength, c_{ps} :-

$$c_{ps} = \frac{2}{\sqrt{3}}\,c \qquad (3.38)$$

Equation (3.38) may be used to compare collapse loads calculated using the Tresca and von Mises yield functions.

3.5.2 Matsuoka Plasticity

The Matsuoka yield function (Matsuoka (1976)) may be written in terms of principal stresses:-

$$f(\underset{\sim}{\sigma}) = \frac{(\sigma_2 - \sigma_3)^2}{\sigma_2 \sigma_3} + \frac{(\sigma_1 - \sigma_3)^2}{\sigma_1 \sigma_3} + \frac{(\sigma_1 - \sigma_2)^2}{\sigma_1 \sigma_2} - 8\tan^2(\phi) \qquad (3.39)$$

where ϕ is the triaxial compression friction angle. Alternatively, in terms of stress invariants:-

$$f(\underset{\sim}{\sigma}) = \frac{I_1 I_2}{I_3} - \left[9 + 8\tan^2(\phi)\right] \qquad (3.40)$$

As is the case with the Mohr–Coulomb plasticity model, the use of an associated flow rule gives rise to an angle of dilation that is unrealistically high. The usual solution to this difficulty for the case of Mohr–Coulomb plasticity is to use a non-associated flow rule in which the dilation characteristics of the soil are specified independently from the friction angle (e.g. Baker and Desai (1982), Zienkiewicz et al. (1975)). This type of procedure has been used with considerable success in previous finite element models based on the Mohr–Coulomb criterion, and is adopted here to derive a plasticity model based on the Matsuoka yield function.

The use of a non-associated flow rule does, however, have some implications for the choice of solution algorithm. Firstly, the element stiffness matrices are not symmetric, which means that the whole of the global stiffness must be inverted rather than the more efficient process of inverting only half of a symmetric matrix*. A further effect of using a non-associated flow rule is that the general stability of the solution algorithm tends to deteriorate as the difference between the friction and dilation angles becomes large. This trend has been noted by Griffiths (1982) for the Mohr-Coulomb model, and has also been observed in the results of the collapse load calculations described in Section 6.9.2.

In deriving a mathematical model of material behaviour based on the Matsuoka yield criterion for which the dilation characteristics may be specified independently from the friction angle, it is useful to consider first the two limits of behaviour, case 'A' in which the flow rule is fully associated, and case 'B' in which the flow rule is associated in the 'π' plane with zero plastic volumetric strain rate.

For case 'A', the plastic potential is identical to the yield function and may be written in terms of stress invariants:-

$$g(\underset{\sim}{\sigma}) = \frac{I_1 I_2}{I_3} - \zeta \qquad (3.41)$$

---

* In the large strain formulation described in this thesis, the stiffness matrix is non-symmetric even if an associated flow rule is used (see Section 2.2.3). It is therefore necessary in this case to use a non-symmetric equation solver even if the flow rule is associated.

where:-

$$\zeta = 9 + 8\tan^2(\phi) \tag{3.42}$$

from which the plastic strain rates may be derived using equation (3.18).

In order to obtain a relationship between the triaxial compression and plane strain friction angles, it is necessary to consider the limiting case in which the elastic strain rates are negligible in comparison with the plastic strain rates. This implies that the out-of-plane plastic strain rate is zero, which is a condition that may be used to derive a relationship between the three principal stresses. This equation, in conjunction with the yield function, may then be used to obtain an expression for the plane strain friction angle.

For the case of full association, the flow rule may be used to obtain an expression for the out-of-plane strain rate:-

$$\dot{\epsilon}^p_2 = \lambda\frac{\partial g}{\partial \sigma_2} = \frac{\lambda}{I_3}\left[I_2 + I_1(\sigma_1 + \sigma_3) - \sigma_1\sigma_3\zeta \right] \tag{3.43}$$

where λ is a scalar multiplier. Equating this expression to zero gives a relationship between the out-of-plane stress σ_2, and the in-plane stresses σ_1 and σ_3:-

$$\sigma_2 = (\sigma_1 \sigma_3)^{1/2} \tag{3.44}$$

The plane strain friction angle ϕ_{ps} is defined in equation (3.32). This may be related to the triaxial compression friction angle, ϕ, by substituting equation (3.44) into the Matsuoka yield function (equation (3.39)) to give:-

$$2\sec^2(\phi) = \sec(\phi_{ps}) + \sec^2(\phi_{ps}) \tag{3.45}$$

A model of material behaviour for case 'B' may be obtained by deriving the plastic strain rates from the deviatoric terms of the fully associated plastic potential. In this case, the out-of-plane plastic strain rate is:-

$$\dot{\epsilon}^p_2 = \frac{2}{3}\frac{\partial g}{\partial \sigma_2} - \frac{1}{3}\frac{\partial g}{\partial \sigma_1} - \frac{1}{3}\frac{\partial g}{\partial \sigma_3} \tag{3.46}$$

$$= \frac{I_1\left[I_1 - 3\sigma_2\right] + \zeta\left[I_2 - 3I_3/\sigma_2\right]}{3I_3} \tag{3.47}$$

In the limit that the elastic strain rates are negligible in comparison with the plastic strain rates, then equation (3.47) may be set to zero to give a relationship between the three principal stresses:-

$$\sigma_2^2 = \frac{2\,\sigma_1^2\,\sigma_3^2}{\sigma_1^2 + \sigma_3^2} \tag{3.48}$$

Substituting equation (3.48) into the Matsuoka yield function (equation (3.39)) gives the relationship between the plane strain and triaxial compression friction angles for the case of zero dilation:-

$$\sec^2(\phi_{ps})\left[1 + \frac{1}{\left[1 + \sin^2(\phi_{ps})\right]^{1/2}}\right] = 2\sec^2(\phi) \tag{3.49}$$

The material behaviour for the case when the dilation rate lies between these two extremes is obtained by taking a weighted average of the plastic strain rates that give full and zero dilation. In tensorial notation, the plastic strain rates derived in this way are:-

$$\dot{\epsilon}^{p}_{ij} = \lambda \left[\frac{\partial g}{\partial \sigma_{ij}} - \frac{(1 - \gamma_a)}{3} \delta_{ij} \frac{\partial g}{\partial \sigma_{kk}} \right] \qquad (3.50)$$

where the repeated suffices imply summation, δ_{ij} is the Kronecker delta and $g(\underset{\sim}{\sigma})$ is the potential defined by equation (3.41). The variable γ_a may be considered to represent the 'degree-of-association'; for the case when γ_a is unity the behaviour reduces to the fully associated case, and when γ_a is zero, the dilation rate is zero. This model of material behaviour is incorporated into the finite element formulation described in Section 3.3 by replacing the derivatives of the plastic potential in equation (3.24) by the appropriate vector of plastic strain rates derived from equation (3.50).

In order to relate finite element calculations based on the Mohr-Coulomb model to analyses based on the Matsuoka yield criterion using the flow rule defined by equation (3.50), it is necessary to relate the Matsuoka parameters ϕ and γ_a to the angle of dilation and plane strain friction angle used in the Mohr-Coulomb model. Unfortunately, closed form equations relating these quantities cannot be derived except for the limiting cases of zero and full dilation in which relationships can be obtained that relate ϕ and ϕ_{ps} (see equations (3.45) and (3.49)).

A general correlation between the Mohr-Coulomb and Matsuoka constants may again be obtained by considering the limiting case for the

Matsuoka model in which the out-of-plane plastic strain rate is zero. The out-of-plane plastic strain rate may be derived from equation (3.50) which, if equated to zero, gives the identity:-

$$\sigma_2^3(1-\gamma_a)(\sigma_1^2+\sigma_3^2) + \sigma_2^2\Big[(1-\gamma_a)(\sigma_1^3+\sigma_3^3) + (1+2\gamma_a)(\sigma_1+\sigma_3)(\sigma_1\sigma_3)\Big]$$

$$+ 2(1-\gamma_a)\sigma_1^2\sigma_3^2\sigma_2 - (2+\gamma_a)\sigma_1^2\sigma_3^2(\sigma_1+\sigma_3) = 0 \qquad (3.51)$$

Since in this general case it is not possible to obtain an expression that can be used to eliminate σ_2 from the Matsuoka yield function, a numerical method must be used to calculate combinations of the parameters ϕ, ϕ_{ps} and γ_a that are consistent with equations (3.51), (3.32) and the Matsuoka yield function, equation (3.39). The plane strain dilation angle is given by the definition:-

$$\sin(\psi_{ps}) = \frac{\dot{\epsilon}_1^p + \dot{\epsilon}_3^p}{\dot{\epsilon}_1^p - \dot{\epsilon}_3^p} \qquad (3.52)$$

which may be related to ϕ and γ_a by substituting for the plastic strain rates using the appropriate terms of equation (3.50). Some selected comparisons between the Matsuoka and Mohr-Coulomb parameters calculated in this way are listed in Table 3.1.

In implementing this Matsuoka model in a finite element computer program, it is important to note that as well as the conical surface that represents the limit of elastic behaviour, the Matsuoka yield function defines additional surfaces that have no physical meaning. The surfaces defined by the Matsuoka yield criterion are illustrated in Figure 3.2, which shows the contours in the 'π' plane for which the yield function is

$\phi_{ps} = 20^\circ$

γ_a	ϕ	ψ_{ps}
0.0	17.71°	0.0°
0.2	17.61°	4.08°
0.4	17.53°	8.07°
0.6	17.46°	12.01°
0.8	17.42°	15.97°
1.0	17.41°	20.00°

$\phi_{ps} = 30^\circ$

γ_a	ϕ	ψ_{ps}
0.0	27.15°	0.0°
0.2	26.87°	6.24°
0.4	26.64°	12.19°
0.6	26.46°	18.02°
0.8	26.34°	23.89°
1.0	26.29°	30.00°

$\phi_{ps} = 40^\circ$

γ_a	ϕ	ψ_{ps}
0.0	37.02°	0.0°
0.2	36.55°	8.45°
0.4	36.13°	16.33°
0.6	35.77°	23.96°
0.8	35.51°	31.69°
1.0	35.39°	40.00°

$\phi_{ps} = 45^\circ$

γ_a	ϕ	ψ_{ps}
0.0	42.10°	0.0°
0.2	41.54°	9.56°
0.4	41.02°	18.37°
0.6	40.58°	26.88°
0.8	40.22°	35.51°
1.0	40.06°	45.0°

Table 3.1: Comparisons between Mohr-Coulomb and Matsuoka Plasticity Parameters

zero. Note that zones exist for which the yield function is negative but the stress state is not elastic. In calculating Gauss point stresses at the end of the calculation step, care should be exercised to ensure that the resulting stresses do not lie in one of these spurious zones and the material subsequently treated as elastic.

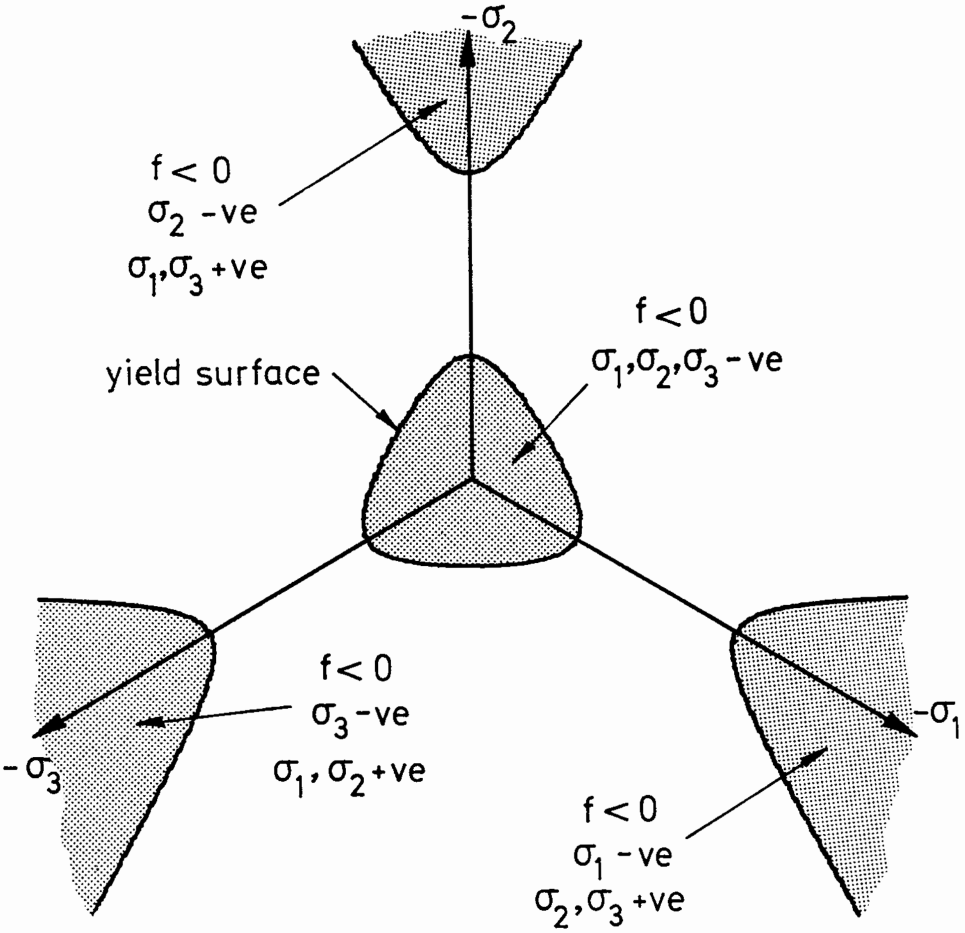

Figure 3.2: Matsuoka Yield Surface

A further consideration in any practical application of the Matsuoka model described in this section is that a singularity exists at the origin of stress space. When the stresses lie at this point the plastic stiffness matrix is undefined, because the denominator of equation (3.24) is zero. Since the origin may be considered to lie either on the yield surface or inside it, the procedure used in this formulation is to treat the Gauss point as being elastic if the stresses are zero.

APPENDIX 3A

Finite Element Equations for the Six-Noded Triangle

Consider the iso-parametric mapping shown in Figure 3A.1 for the six-noded triangular element.

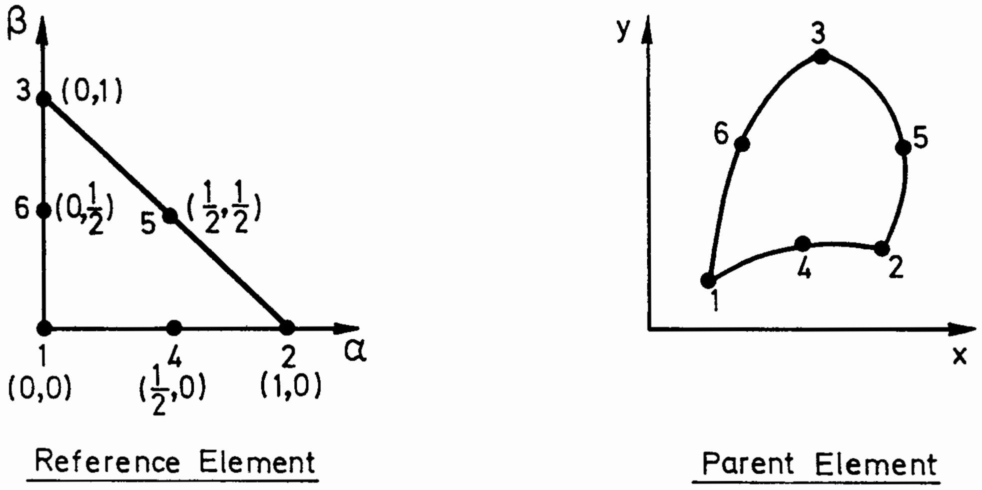

Figure 3A.1: Mapping for the Six-Noded Triangle

The vector of global nodal co-ordinates of a point in the element is:-

$$\underset{\sim}{x} = \begin{bmatrix} x \\ y \end{bmatrix} \tag{3A.1}$$

and the vector of global nodal co-ordinates is:-

$$\underset{\sim}{X} = \begin{bmatrix} X_1 \\ Y_1 \\ X_2 \\ \cdot \\ \cdot \\ \cdot \\ \cdot \\ \cdot \\ X_6 \\ Y_6 \end{bmatrix} \tag{3A.2}$$

where X_i, Y_i are the global co-ordinates of the i^{th} node. The shape function matrix, as defined by equation (3.9), is of the form:-

$$[N] = \begin{bmatrix} f_1 & o & f_2 & o & f_3 & o & f_4 & o & f_5 & o & f_6 & o \\ o & f_1 & o & f_2 & o & f_3 & o & f_4 & o & f_5 & o & f_6 \end{bmatrix} \qquad (3A.3)$$

where:-

$$\begin{aligned} f_1 &= 2(\alpha + \beta - 1)(\alpha + \beta - 1/2) & f_2 &= 2\alpha(\alpha - 1/2) \\ f_3 &= 2\beta(\beta - 1/2) & f_4 &= -4\alpha(\alpha + \beta - 1) \\ f_5 &= 4\alpha\beta & f_6 &= -4\beta(\alpha + \beta - 1) \end{aligned} \qquad (3A.4)$$

The 12 × 12 non-symmetrical [C] (distortion rate) matrix is:-

$$[C] = \begin{bmatrix} c_{1,1} & c_{1,2} & c_{1,3} & \cdots\cdots & c_{1,12} \\ c_{2,1} & c_{2,2} & c_{2,1} & \cdots\cdots & c_{2,12} \\ \vdots & \vdots & & & \vdots \\ c_{12,1} & c_{12,2} & \cdots\cdots & & c_{12,12} \end{bmatrix} \qquad (3A.5)$$

where:-

$$c_{2i,2j} = \tau_{xy} \det[J_{ij}] \qquad i=1,6 \quad j=1,6 \qquad (3A.6)$$

$$c_{2i,2j-1} = -\sigma_{yy} \det[J_{ij}] \qquad i=1,6 \quad j=1,6 \qquad (3A.7)$$

$$c_{2i-1,2j} = \sigma_{xx} \det[J_{ij}] \qquad i=1,6 \quad j=1,6 \qquad (3A.8)$$

$$c_{2i-1,2j-1} = -\tau_{xy} \det[J_{ij}] \qquad i=1,6 \quad j=1,6 \qquad (3A.9)$$

$$\det[J_{ij}] = \begin{vmatrix} \frac{\partial f_i}{\partial \alpha} & \frac{\partial f_j}{\partial \alpha} \\ \frac{\partial f_i}{\partial \beta} & \frac{\partial f_j}{\partial \beta} \end{vmatrix} \qquad (3A.10)$$

and f_i are the element shape functions.

4.1 Introduction

An important feature of the solution scheme described in this thesis is that it is necessary to perform an equilibrium check at the end of each calculation increment (see Section 2.4). This requires that the stresses at each Gauss point be updated by evaluating an integral of the form given in equation (2.41).

Three separate operations, in general, are needed to calculate the updated Gauss point stresses. Firstly, it is necessary to calculate the strain rates $\dot{\underset{\sim}{\epsilon}}$ which, when integrated over the time step, are compatible with the incremental displacements. This is achieved by obtaining a solution to the differential equation:-

$$\dot{\underset{\sim}{\epsilon}} = [L]\,\dot{\underset{\sim}{x}} \qquad (4.1)$$

where [L] is the operator matrix defined by equation (3.13) and $\dot{\underset{\sim}{x}}$ is a velocity vector at the Gauss point which is consistent with the displacements occurring during the calculation step. Since the basis of the finite element method is to calculate values of the primary variables at discrete times during the loading, no information is available regarding the way that these quantities vary during the calculation step. In order to obtain a solution to equation (4.1) therefore, it is necessary to make an arbitrary assumption about the nature of the variation of either the velocities or the strain rates during the increment. In the formulation described in this thesis, the assumption is made that the strain rates remain constant during the calculation step. This approach has the useful advantage that closed form solution can be obtained for the strain rates (see Section 4.2).

The second stage of the 'stress update' calculation is to obtain the incremental Gauss point stresses by integrating the constitutive equations. In some cases (e.g. elastic behaviour, and von Mises plasticity excluding the Jaumann terms), updated stresses may be obtained from a closed form solution, but for the other types of constitutive behaviour described in this thesis it is necessary to use a numerical integration scheme.

The third, and final, stage of the 'stress update' calculation is to correct the stresses back to the yield surface if a numerical scheme has been used to integrate the constitutive law.

4.2 Calculation of Gauss Point Strain Rates

In order to calculate a set of strain rates, and rotation rate, that are compatible with the incremental nodal displacements, the assumption is made that the strain rates and rotation rates are constant for a material point over the calculation step. The means that the velocity gradients ($\frac{\partial u}{\partial x}$ etc.) also remain constant. In the region of each Gauss point, the strain rates may be assumed to be spatially constant in which case equations (3.1) and (3.2) may be integrated to give:-

$$u = u_o + \left[\frac{\partial u}{\partial x}\right]x + \left[\frac{\partial u}{\partial y}\right]y \qquad (4.2)$$

$$v = v_o + \left[\frac{\partial v}{\partial y}\right]y + \left[\frac{\partial v}{\partial x}\right]x \qquad (4.3)$$

where u_o and v_o are constants, and the higher order terms due to the spatial variation of velocity gradients are neglected. Given that:-

$$u = \dot{x} \quad \text{and} \quad v = \dot{y} \qquad (4.4)$$

then equations (4.2) and (4.3) may be re-arranged to give a differential equation in x:-

$$\ddot{x} - \left[d_{xx} + d_{yy}\right]\dot{x} + \left[d_{xx}d_{yy} - d_{xy}d_{yx}\right]x - d_{xy}v_o + d_{yy}u_o = 0 \qquad (4.5)$$

where:-

$$\begin{bmatrix} \frac{\partial u}{\partial x} & \frac{\partial u}{\partial y} \\ \frac{\partial v}{\partial x} & \frac{\partial v}{\partial y} \end{bmatrix} = \begin{bmatrix} d_{xx} & d_{xy} \\ d_{yx} & d_{yy} \end{bmatrix} \qquad (4.6)$$

Equation (4.5) may be solved to give an equation for x:-

$$x = A_1 \exp(w_1 t) + A_2 \exp(w_2 t) + \frac{d_{xy} v_o - d_{yy} u_o}{d_{xx} d_{yy} - d_{xy} d_{yx}} \qquad (4.7)$$

where A_1 and A_2 are constants, t is the time and:-

$$w_1, w_2 = \frac{(d_{xx} + d_{yy}) \pm \left[(d_{xx} - d_{yy})^2 + 4\, d_{xy}\, d_{yx}\right]^{1/2}}{2} \qquad (4.8)$$

A similar solution exists for y:-

$$y = B_1 \exp(w_1 t) + B_2 \exp(w_2 t) + \frac{d_{yx} u_o - d_{xx} v_o}{d_{xx} d_{yy} - d_{xy} d_{yx}} \quad (4.9)$$

where:-

$$B_1 = \frac{A_1}{d_{xy}} (w_1 - d_{xx}) \text{ and } B_2 = \frac{A_2}{d_{xy}} (w_2 - d_{xx}) \quad (4.10)$$

The velocity gradients may be calculated by considering the Jacobian matrix of the transformation of the co-ordinates during the time step. If x^t, y^t are the Cartesian co-ordinates of a material point at the start of a calculation step, and $x^{t+\Delta t}$, $y^{t+\Delta t}$ are the co-ordinates of the point at the end, then the Jacobian of the transformation is:-

$$[J] = \begin{bmatrix} \frac{\partial x^{t+\Delta t}}{\partial x^t} & \frac{\partial x^{t+\Delta t}}{\partial y^t} \\ \frac{\partial y^{t+\Delta t}}{\partial x^t} & \frac{\partial y^{t+\Delta t}}{\partial y^t} \end{bmatrix} = \begin{bmatrix} D_{xx} & D_{xy} \\ D_{yx} & D_{yy} \end{bmatrix} \quad (4.11)$$

Equations (4.7) and (4.9) may be used to obtain expressions for the elements of the Jacobian matrix which, if the length of the time step is normalised to unity, are:-

$$D_{xx} = \frac{1}{w_2 - w_1} \left\{ (w_2 - d_{xx}) e^{w_1} - (w_1 - d_{xx}) e^{w_2} \right\} \quad (4.12)$$

$$D_{xy} = \frac{1}{w_2 - w_1} \left\{ d_{xy} (e^{w_2} - e^{w_1}) \right\} \quad (4.13)$$

$$D_{yx} = \frac{1}{w_2 - w_1} \left\{ d_{yx} \left(e^{w_2} - e^{w_1}\right)\right\} \qquad (4.14)$$

$$D_{yy} = \frac{1}{w_2 - w_1} \left\{(w_2 - d_{xx})e^{w_2} - (w_1 - d_{xx})e^{w_1}\right\} \qquad (4.15)$$

The individual elements of the Jacobian matrix defined above may be calculated independently by considering the geometry of the element at the start and finish of the calculation increment. Thus, from equations (4.12) to (4.15), four simultaneous equations are obtained which may be solved to give a set of strain rates and rotation rates which, if held constant over the time interval produce the prescribed deformation:-

$$\begin{aligned} \dot{\epsilon}_{xx} + \dot{\epsilon}_{yy} &= d_{xx} + d_{yy} \\ &= \log_e(\det[J]) \end{aligned} \qquad (4.16)$$

$$\begin{aligned} \dot{\epsilon}_{xx} - \dot{\epsilon}_{yy} &= d_{xx} - d_{yy} \\ &= F(D_{xx} - D_{yy}) \end{aligned} \qquad (4.17)$$

$$\begin{aligned} \dot{\gamma}_{xy} &= d_{xy} + d_{yx} \\ &= F\,(D_{xy} + D_{yx}) \end{aligned} \qquad (4.18)$$

$$\begin{aligned} 2\dot{\theta}_{xy} &= d_{xy} - d_{yx} \\ &= F\,(D_{xy} - D_{yx}) \end{aligned} \qquad (4.19)$$

The factor F depends on the value of the discriminant D where:-

$$D = (D_{xx} - D_{yy})^2 + 4\,D_{xy}\,D_{yx} \qquad (4.20)$$

If D > 0 then:-

$$F = \frac{\log_e \left[\dfrac{(D_{xx} + D_{yy}) + \sqrt{D}}{(D_{xx} + D_{yy}) - \sqrt{D}} \right]}{\sqrt{D}} \tag{4.21}$$

(Note, no solution exists for the case $D > (D_{xx} + D_{yy})^2$ in which case the Jacobian is negative.)

If D = 0 then:-

$$F = \frac{2}{(D_{xx} + D_{yy})} \tag{4.22}$$

If D < 0 then:-

$$F = \frac{2 \tan^{-1} \left[\dfrac{\sqrt{(-D)}}{D_{xx} + D_{yy}} \right]}{\sqrt{(-D)}} \tag{4.23}$$

4.3 Integration of Stress-Strain Laws

In the calculation of the updated Gauss point stresses, several cases of constitutive behaviour need to be considered and these are dealt with in turn. In addition, it is necessary to evaluate yield surface intersections for the case when the material changes state during the calculation step.

In this formulation, all stress increments are initially assumed elastic, regardless of the initial state. If the resulting stress point lies outside the yield surface, then the 'stress update' calculation is repeated using the appropriate elasto-plastic constitutive law; thus the possibility of elastic unloading is accounted for (Davis et al. (1974)).

The mean pressure p, and volumetric strain rate $\dot{v}$ are defined:-

$$p = \frac{1}{3}(\sigma_{xx} + \sigma_{yy} + \sigma_{zz}) \qquad \dot{v} = \dot{\epsilon}_{xx} + \dot{\epsilon}_{yy} + \dot{\epsilon}_{zz} \qquad (4.24)$$

where the superior dot denotes a time derivative with reference to a fixed Cartesian reference frame. Since the theory developed in this section relates to the plane-strain case only, $\dot{\epsilon}_{zz}$ is invariably zero. Deviatoric stresses s_{xx}, s_{yy} and deviatoric strain rates $\dot{e}_{xx}$ and $\dot{e}_{yy}$ are defined:-

$$s_{xx} = \sigma_{xx} - p \qquad \dot{e}_{xx} = \dot{\epsilon}_{xx} - \frac{\dot{v}}{3} \qquad (4.25)$$

$$s_{yy} = \sigma_{yy} - p \qquad \dot{e}_{yy} = \dot{\epsilon}_{yy} - \frac{\dot{v}}{3} \qquad (4.26)$$

In all of the solutions described in this section, the material deformation is defined by the strain rates derived in Section 4.2, in which the calculation increment is taken to occur during the time interval $0 \leqslant t \leqslant 1$.

4.3.1 Elastic Behaviour, Including Jaumann Rotation Terms

The mean pressure at time t is given by:-

$$p = p_o + K \dot{v} t \tag{4.27}$$

where p_o is the mean pressure at time t = 0 and K is the bulk modulus. The constitutive equation relates strain rates to Jaumann stress rates which, for elastic behaviour gives the following relationship between the deviatoric components:-

$$\overset{\nabla}{s}_{xx} = 2G \dot{e}_{xx} \tag{4.28}$$

$$\overset{\nabla}{s}_{yy} = 2G \dot{e}_{yy} \tag{4.29}$$

$$\overset{\nabla}{\tau}_{xy} = G \dot{\gamma}_{xy} \tag{4.30}$$

where G is the shear modulus.

The deviatoric forms of the Jaumann stress rates given in equations (3.5), (3.6) and (3.8) are:-

$$\overset{\nabla}{s}_{xx} = \dot{s}_{xx} - 2\tau_{xy} \dot{\theta}_{xy} \tag{4.31}$$

$$\overset{\nabla}{s}_{yy} = \dot{s}_{yy} + 2\tau_{xy} \dot{\theta}_{xy} \tag{4.32}$$

$$\overset{\nabla}{\tau}_{xy} = \dot{\tau}_{xy} + \dot{\theta}_{xy} (s_{xx} - s_{yy}) \tag{4.33}$$

Equations (4.31), (4.32) and (4.33) may be solved using the constitutive equations, (4.28), (4.29) and (4.30) to give a solution for the stresses:-

$$s_a = 2G\,\dot{e}_a\,t + s_{ao} \tag{4.34}$$

$$s_b = s_{bo}\cos(2\omega t) + 2G\dot{e}_b\left[\frac{\sin(2\omega t)}{2\omega}\right] + 2\tau_o\sin(2\omega t) + 2G\dot{\gamma}_{xy}\left[\frac{1-\cos(2\omega t)}{2\omega}\right] \tag{4.35}$$

$$\tau_{xy} = \tau_o\cos(2\omega t) + G\dot{\gamma}_{xy}\left[\frac{\sin(2\omega t)}{2\omega}\right] - \frac{1}{2}s_{bo}\sin(2\omega t) - G\dot{e}_b\left[\frac{1-\cos(2\omega t)}{2\omega}\right] \tag{4.36}$$

where:-

$$s_a = s_{xx} + s_{yy} \qquad \dot{e}_a = \dot{e}_{xx} + \dot{e}_{yy} \tag{4.37}$$

$$s_b = s_{xx} - s_{yy} \qquad \dot{e}_b = \dot{e}_{xx} - \dot{e}_{yy} \tag{4.38}$$

$$\omega = \dot{e}_{xy} \tag{4.39}$$

and s_{ao}, s_{bo}, τ_o are the values at the start of the calculation step. When the rotation rate is very small (i.e. $\omega \to 0$), the use of equations (4.35) and (4.36) could lead to significant 'roundoff' errors since the evaluation of these expressions involves dividing by the rotation rate. In this case, expanded equations in which the rotation terms appear only in the numerator should be used to avoid this difficulty. If an expansion is used in which only the first order rotation terms are retained, then equations (4.35) and (4.36) reduce to:-

$$s_b = s_{bo} + 2G\,\dot{e}_b\,t + 4\tau_o\,\omega\,t + 2G\,\dot{\gamma}_{xy}\,\omega\,t^2 \tag{4.40}$$

$$\tau_{xy} = \tau_o + G\,\dot{\gamma}_{xy}\,t - s_{bo}\,\omega\,t - G\,\dot{e}_b\,\omega\,t^2 \tag{4.41}$$

4.3.2 von Mises Plasticity, Jaumann Terms Excluded

A closed form solution exists for the case of von Mises plasticity when the Jaumann terms are not included (Booker (1984)). Although this solution is not applicable to the general large strain case, it may be used to solve problems where material rotation does not occur (for example the cavity expansion analysis described in Section 6.8), and to check the numerical scheme described in Section 4.3.3 for the special case when the rotation rates are zero.

The volumetric behaviour is always elastic and the mean pressure may be derived from equation (4.27). The solution for the deviatoric stresses is:-

$$s_{xx}\,\eta = 2G\,\dot{e}_{xx}\,\xi + s_{xo} \tag{4.42}$$

$$s_{yy}\,\eta = 2G\,\dot{e}_{yy}\,\xi + s_{yo} \tag{4.43}$$

$$\tau_{xy}\,\eta = G\,\dot{\gamma}_{xy}\,\xi + \tau_o \tag{4.44}$$

where:-

$$\xi = \left[\frac{\alpha}{\beta}\right] \sinh\left[\frac{\beta}{\alpha}t\right] + \left[\frac{\alpha}{\beta}\right] \chi \cosh\left[\frac{\beta}{\alpha}t\right] - \left[\frac{\alpha}{\beta}\right] \chi \tag{4.45}$$

$$\eta = \cosh\left[\frac{\beta}{\alpha}t\right] + \chi \sinh\left[\frac{\beta}{\alpha}t\right] \tag{4.46}$$

$$\alpha = \frac{2c}{\sqrt{3}} \tag{4.47}$$

$$\beta^2 = 4G^2 \left[\dot{e}_{xx}^2 + \dot{e}_{xx}\,\dot{e}_{yy} + \dot{e}_{yy}^2 + \frac{\dot{\gamma}_{xy}^2}{4}\right] \tag{4.48}$$

$$2\alpha\,\beta\,\chi = 2G\left[s_{xo}(2\dot{e}_{xx} + \dot{e}_{yy}) + s_{yo}(2\dot{e}_{yy} + \dot{e}_{xx}) + \tau_o\,\dot{\gamma}_{xy}\right] \tag{4.49}$$

and s_{xo}, s_{yo}, τ_o are the values of the stresses at the start of the calculation increment.

4.3.3 von Mises Plasticity, Including Jaumann Rotation Terms

Since the solution described in Section 4.3.2 is not readily extended to include the Jaumann rotation terms, it is necessary to use a numerical method to integrate the constitutive law for the case of von Mises plasticity when rotation effects are present.

The algorithm used in this formulation is based on a Runge-Kutta integration scheme in which the updated stresses are evaluated by dividing the calculation step into a number of 'sub-increments'. In order to improve the efficiency of this calculation, a procedure is used in which the size of the 'sub-increments' are varied automatically in order to perform the integration at each of the Gauss points to a specified accuracy. In this algorithm, which is described by Sloan (1984), an estimate is made of the errors occurring at each 'sub-increment'. The magnitude of the error is then used to determine the size of the following 'sub-increment', or, if the error is unacceptable, the size of the sub-increment is reduced, and the calculation repeated.

4.3.4 Matsuoka Plasticity

No known closed form solution exists for the 'stress update' calculation in which the constitutive law is based on the Matsuoka plasticity model described in Section 3.5.2. In this case, the calculation is performed using the 'error control' algorithm described in Section 4.3.3.

4.4 Calculation of Yield Surface Intersections

For the case when the material becomes plastic during the calculation step, it is necessary to find the point in the increment at which yield surface intersection occurs. The increment is then split into two parts and the 'stress update' calculation for the elastic and plastic parts performed independently.

4.4.1 von Mises Plasticity

The elastic equations derived in Section 4.3.1 may be combined with the von Mises yield function (equation (3.33)) to give an equation that defines the time t at which intersection with the von Mises yield locus occurs:-

$$A_1 + A_2 t + A_3 t^2 + A_4 \frac{(1 - \cos(2\omega t))}{\omega^2} + A_5 \frac{\sin(2\omega t)}{\omega} = \frac{16c^2}{3} \quad (4.50)$$

where the constants A_1 to A_5 are defined in Appendix 4A. For the case of small rotation, this equation reduces to:-

$$A_1 + (A_2 + 2A_5)t + (A_3 + 2A_4)t^2 = \frac{16c^2}{3} \qquad (4.51)$$

The above equation may be used to calculate the time, t, at which the yield surface intersection occurs for the case when the rotation rate is very small. For the general case, an approximate solution to equation (4.50) is obtained from equation (4.51), which is then refined using a Newton-Raphson iteration scheme.

4.4.2 Matsuoka Plasticity

The Matsuoka yield function (equation 3.39) may be re-cast in the form:-

$$\zeta I'_3 + p I'_2 (\zeta - 3) + p^3 (\zeta - 9) = 0 \qquad (4.52)$$

where ζ is defined in equation (3.42) and p, the mean pressure, is defined in equation (4.24).

From the elastic equations derived in Section 4.3.1 for the case when rotation effects are absent:-

$$I'_3 = a_0 + a_1 (2Gt) + a_2 (2Gt)^2 + a_3 (2Gt)^3 \qquad (4.53)$$

$$pI'_2 = b_0 + b_1 (2Gt) + b_2 (2Gt)^2 + b_3 (2Gt)^3 \qquad (4.54)$$

$$p^3 = c_0 + c_1(2Gt) + c_2(2Gt)^2 + c_3(2Gt)^3 \qquad (4.55)$$

where the constants in the above expression are defined in Appendix 4B.

If the Jaumann rotation terms are excluded, therefore, an exact solution to the yield surface intersection may be obtained by solving the cubic equation defined by equations (4.52) to (4.55), taking care to select the appropriate root. For the case when the Jaumann rotation terms are included, the zero rotation case is used to give an initial estimate of the intersection which is then refined using a Newton-Raphson iteration scheme.

4.5 Yield Surface Correction

In any numerical integration scheme used to perform 'stress update' calculations in the plastic regime, the possibility exists that the final stress state will not lie on the yield surface within acceptable bounds. The usual practice is to deal with these offending stress states by correcting them back to the yield surface. The choice of correction algorithm is largely arbitrary, and generally has little effect on the results of the calculation if an accurate scheme is used to perform the numerical integration of the constitutive law.

In this formulation, all stresses obtained by numerical integration of the constitutive law are corrected if they lie outside the yield surface at the end of the calculation step. In performing this correction, the principal directions are kept fixed and any adjustment is made to the values of the principal stresses. For the von Mises case, the stresses are adjusted in a direction in stress space normal to the yield surface. In the Matsuoka case however, this correction procedure leads to severe mathematical difficulties that are avoided if the stresses are adjusted in a direction normal to an 'expanded' yield surface that passes through the uncorrected stress point. This means that the direction of correction may be written in terms of the known stresses. A scheme of this sort is only suitable for cases when the corrections are small, since if errors are large the possibility exists that the normal to the 'expanded' yield surface does not intersect the true yield locus as shown in Figure 4.1.

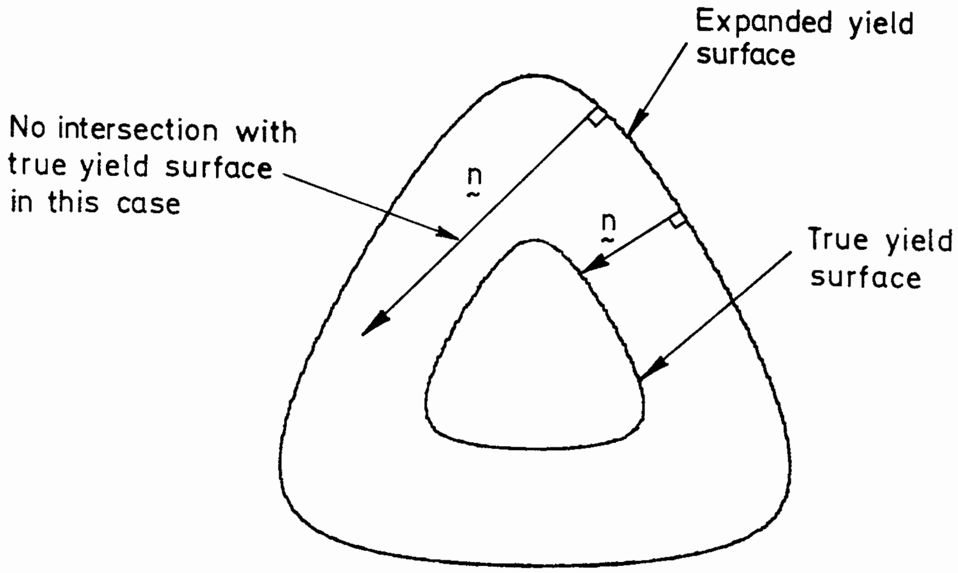

Figure 4.1: Matsuoka Yield Surface Correction

4.5.1 von Mises Plasticity

If $(\sigma^c_1, \sigma^c_2, \sigma^c_3)$ are a set of principal stresses that lie on the yield surface, then a vector normal to the surface that passes through this stress point is:-

$$\underset{\sim}{n} = (2\sigma_1^C - \sigma_2^C - \sigma_3^C)\,\underset{\sim}{a}_1 + (2\sigma_2^C - \sigma_1^C - \sigma_3^C)\,\underset{\sim}{a}_2 + (2\sigma_3^C - \sigma_1^C - \sigma_2^C)\,\underset{\sim}{a}_3 \tag{4.56}$$

where $\underset{\sim}{a}_1$, $\underset{\sim}{a}_2$, $\underset{\sim}{a}_3$ are unit vectors in directions corresponding to σ_1^C, σ_2^C and σ_3^C. If $(\sigma_1, \sigma_2, \sigma_3)$ are a set of stresses that lie outside the yield surface, then the corresponding corrected stresses are:-

$$\underset{\sim}{\sigma}^C = \underset{\sim}{\sigma} + \lambda\,\underset{\sim}{n} \tag{4.57}$$

where λ is a scalar. Substituting equation (4.57) into the von Mises yield expression (equation (3.33)) gives:-

$$\sigma_i^C = \frac{\sigma_i + (\chi - 1)\left[\dfrac{\sigma_1 + \sigma_2 + \sigma_3}{3}\right]}{\chi} \tag{4.58}$$

where:-

$$\chi = 1 + 3\lambda = \left[\frac{-3I_2'}{4c^2}\right]^{1/2} \tag{4.59}$$

and I_2' is the second invariant of the deviator of the uncorrected stresses.

4.5.2 Matsuoka Plasticity

The yield surface correction for Matsuoka plasticity is calculated in a similar way to the von Mises case except that the correction is performed in a direction normal to an expanded yield surface passing through the uncorrected stress point. The expanded yield surface is defined by the friction angle ϕ^e where:-

$$\frac{(\sigma_2 - \sigma_3)^2}{\sigma_2 \sigma_3} + \frac{(\sigma_1 - \sigma_3)^2}{\sigma_1 \sigma_3} + \frac{(\sigma_1 - \sigma_2)^2}{\sigma_1 \sigma_2} = 8\tan^2(\phi^e) \qquad (4.60)$$

The vector normal to the expanded yield surface is:-

$$\underset{\sim}{n} = n_1 \underset{\sim}{a}_1 + n_2 \underset{\sim}{a}_2 + n_3 \underset{\sim}{a}_3 \qquad (4.61)$$

where $\underset{\sim}{a}_1$, $\underset{\sim}{a}_2$ and $\underset{\sim}{a}_3$ are unit vectors in the directions of the principal axes, and n_1, n_2 and n_3 are defined in Appendix 4C.

The corrected stresses are defined by equation (4.57) which may be substituted into the Matsuoka yield function (equation(3.39)) to give a cubic equation in the scalar multiplier, λ:-

$$A_0 + A_1\lambda + A_2\lambda^2 + A_3\lambda^3 = 0 \qquad (4.62)$$

where the constants A_0 to A_3 are defined in Appendix 4C.

It is possible that when stresses are small, one or more of the principal stresses may be positive (i.e. tensile) if a numerical scheme is used to calculate the updated stresses. In this case it is not possible to correct the stresses back to the yield surface using the above approach since an appropriate expanded yield surface does not exist. This situation is dealt by correcting the stresses back to the origin of stress space, a procedure that may be justified on the grounds that tensile stresses arise only when the magnitude of the stresses is very small if an accurate numerical integration scheme is used.

APPENDIX 4A

von Mises Yield Surface Intersection

Equation (4.50) defines the time, t, at which intersection with the von Mises yield surface occurs for an elastic stress increment. The constants in this expression are:-

$$A_1 = 3s_{ao}^2 + s_{bo}^2 + 4\tau_o^2 \tag{4A.1}$$

$$A_2 = 12G\, s_{ao}\, \dot{e}_a \tag{4A.2}$$

$$A_3 = 12G^2\, \dot{e}_a^2 \tag{4A.3}$$

$$A_4 = 2\omega G \left[2\tau_o\, \dot{e}_b - s_{bo}\, \dot{\gamma}_{xy}\right] + 2G^2 \left[\dot{\gamma}_{xy}^2 + \dot{e}_b^2\right] \tag{4A.4}$$

$$A_5 = 2G \left[2\tau_o\, \dot{\gamma}_{xy} + s_{bo}\, \dot{e}_b\right] \tag{4A.5}$$

where:-

$$s_{ao} = s_{xo} + s_{yo} \qquad \dot{e}_a = \dot{e}_{xx} + \dot{e}_{yy} \tag{4A.6}$$

$$s_{bo} = s_{xo} - s_{yo} \qquad \dot{e}_b = \dot{e}_{xx} - \dot{e}_{yy} \tag{4A.7}$$

The deviatoric strain rates, $\dot{e}_{xx}$ and $\dot{e}_{yy}$, are defined by the procedure described in Section 4.2, and s_{xo}, s_{yo} and τ_o are the values of the stresses at the start of the calculation increment.

APPENDIX 4B

Matsuoka Yield Surface Intersection

Equation (4.52) defines the time, t, at which intersection with the Matsuoka yield surface occurs for an elastic stress increment. The constants in this expression are:-

$$a_o = \frac{s_{ao}}{4}\left[4\tau_o^2 + s_{bo}^2 - s_{ao}^2\right] \tag{4B.1}$$

$$a_1 = \dot{e}_a \tau_o^2 + \dot{\gamma}_{xy} \tau_o s_{ao} - \frac{s_{ao}}{2}\left[\dot{e}_a s_{ao} - \dot{e}_b s_{bo}\right] - \frac{\dot{e}_a}{4}\left[s_{ao}^2 - s_{bo}^2\right] \tag{4B.2}$$

$$a_2 = s_{ao}\frac{\dot{\gamma}_{xy}^2}{4} + \dot{\gamma}_{xy} \tau_o \dot{e}_a - \frac{\dot{e}_a}{2}\left[\dot{e}_a s_{ao} - \dot{e}_b s_{bo}\right] - \frac{s_{ao}}{4}\left[\dot{e}_a^2 - \dot{e}_b^2\right] \tag{4B.3}$$

$$a_3 = -\frac{\dot{e}_a}{4}\left[\dot{e}_a^2 - \dot{e}_b^2 - \dot{\gamma}_{xy}^2\right] \tag{4B.4}$$

$$b_o = -p_o\left[\frac{3s_{ao}^2 + s_{bo}^2 + 4\tau_o^2}{4}\right] \tag{4B.5}$$

$$b_1 = -\frac{K\dot{v}}{2G}\left[\frac{3s_{ao}^2 + s_{bo}^2 + 4\tau_o^2}{4}\right] - p_o\left[\frac{3\dot{e}_a s_{ao} + \dot{e}_b s_{bo}}{2} + \dot{\gamma}_{xy} \tau_o\right] \tag{4B.6}$$

$$b_2 = \frac{-K\dot{v}}{2G}\left[\frac{3\dot{e}_a s_{ao} + \dot{e}_b s_{bo}}{2} + \dot{\gamma}_{xy} \tau_o\right] - \frac{p_o}{4}\left[3\dot{e}_a^2 + \dot{e}_b^2 + \dot{\gamma}_{xy}^2\right] \tag{4B.7}$$

$$b_3 = \frac{-K\dot{v}}{2G} \left[\frac{3\dot{e}_a^2 + \dot{e}_b^2 + \dot{\gamma}_{xy}^2}{4}\right] \tag{4B.8}$$

$$c_o = p_o^3 \tag{4B.9}$$

$$c_1 = 3p_o^2 \frac{K\dot{v}}{2G} \tag{4B.10}$$

$$c_2 = 3p_o \left[\frac{K\dot{v}}{2G}\right]^2 \tag{4B.11}$$

$$c_3 = \left[\frac{K\dot{v}}{2G}\right]^3 \tag{4B.12}$$

and:-

$$s_{ao} = s_{xo} + s_{yo} \qquad \dot{e}_a = \dot{e}_{xx} + \dot{e}_{yy} \tag{4B.13}$$

$$s_{bo} = s_{xo} - s_{yo} \qquad \dot{e}_b = \dot{e}_{xx} - \dot{e}_{yy} \tag{4B.14}$$

The deviatoric strain rates, $\dot{e}_{xx}$ and $\dot{e}_{yy}$, are defined by the procedure described in Section 4.2, and s_{xo}, s_{yo} and τ_o are the values of the stresses at the start of the calculation increment. The volumetric strain rate, $\dot{v}$, is defined in equation (4.24) and p_o is the value of the mean pressure (also defined in equation (4.24)) at the start of the increment.

APPENDIX 4C

Matsuoka Yield Surface Correction

The normal to the expanded yield surface defined by equation (4.60) is:-

$$\underset{\sim}{n} = n_1 \underset{\sim}{a}_1 + n_2 \underset{\sim}{a}_2 + n_3 \underset{\sim}{a}_3 \qquad (4C.1)$$

$$\begin{aligned} &= \left[(\sigma_2 - \sigma_3)^2 - 4\sigma_2\sigma_3 + 2\sigma_1(\sigma_2 + \sigma_3) - 8\sigma_2\sigma_3 \tan^2(\phi^e)\right]\underset{\sim}{a}_1 \\ &+ \left[(\sigma_1 - \sigma_3)^2 - 4\sigma_1\sigma_3 + 2\sigma_2(\sigma_1 + \sigma_3) - 8\sigma_1\sigma_3 \tan^2(\phi^e)\right]\underset{\sim}{a}_2 \qquad (4C.2) \\ &+ \left[(\sigma_2 - \sigma_1)^2 - 4\sigma_1\sigma_2 + 2\sigma_3(\sigma_1 + \sigma_2) - 8\sigma_1\sigma_2 \tan^2(\phi^e)\right]\underset{\sim}{a}_3 \end{aligned}$$

where σ_1, σ_2 and σ_3 are are set of stresses that lie on the expanded yield surface.

The value of the scalar multiplier, λ, that satisfies equation (4.57) for the case of Matsuoka plasticity is defined by equation (4.62). The constants in this expression are:-

$$A_o = \sigma_1(\sigma_2 - \sigma_3)^2 + \sigma_2(\sigma_1 - \sigma_3)^2 + \sigma_3(\sigma_1 - \sigma_2)^2 - 8\tan^2(\phi)\sigma_1\sigma_2\sigma_3 \qquad (4C.3)$$

$$\begin{aligned} A_1 &= \left[(\sigma_2 - \sigma_3)^2 - 4\sigma_2\sigma_3 + 2\sigma_1(\sigma_2 + \sigma_3) - 8\sigma_2\sigma_3 \tan^2(\phi)\right]n_1 \\ &+ \left[(\sigma_1 - \sigma_3)^2 - 4\sigma_1\sigma_3 + 2\sigma_2(\sigma_1 + \sigma_3) - 8\sigma_1\sigma_3 \tan^2(\phi)\right]n_2 \qquad (4C.4) \\ &+ \left[(\sigma_2 - \sigma_1)^2 - 4\sigma_1\sigma_2 + 2\sigma_3(\sigma_1 + \sigma_2) - 8\sigma_1\sigma_2 \tan^2(\phi)\right]n_3 \end{aligned}$$

$$\begin{aligned} A_2 = & \left[(n_2 - n_3)^2 - 4n_2n_3 + 2n_1(n_2 + n_3) - 8n_2n_3 \tan^2(\phi)\right]\sigma_1 \\ & + \left[(n_1 - n_3)^2 - 4n_1n_3 + 2n_2(n_1 + n_3) - 8n_1n_3 \tan^2(\phi)\right]\sigma_2 \\ & + \left[(n_2 - n_1)^2 - 4n_1n_2 + 2n_3(n_1 + n_2) - 8n_1n_2 \tan^2(\phi)\right]\sigma_3 \end{aligned} \tag{4C.5}$$

$$A_3 = n_1(n_2 - n_3)^2 + n_2(n_1 - n_3)^2 + n_3(n_1 - n_2)^2 - 8\tan^2(\phi)\, n_1n_2n_3 \tag{4C.6}$$

where n_1, n_2, n_3 are the terms of the vector defined in equation (4C.2), and ϕ is the triaxial compression friction angle defining the true yield surface.

CHAPTER 5 FORMULATION OF MEMBRANE ELEMENTS

5.1 Introduction

This chapter is devoted to a description of a formulation for one-dimensional elements with zero bending stiffness. The finite element equations, which are valid for displacements of an arbitrary magnitude, are developed in a similar manner to the continuum element formulation described in Chapter 3 in that an Eulerian description of deformation is used, and the stiffness equations are derived using an iso-parametric approach.

The Eulerian description of deformation leads naturally to the use of Hencky (or logarithmic) strain to define the material behaviour of the membrane. The formulation described in this chapter has therefore been based on a material that is linearly elastic with respect to this particular strain measure. It should be noted that the stiffness equations derived using this approach will, in general, be different from those derived for a material that is linearly elastic with respect to some alternative strain definition.

The formulation described in this chapter is applicable to membrane elements of arbitrary order and is therefore presented in a general form. The specific equations for the case of the three-noded element are presented in Appendix 5A.

In practical applications of the reinforced earth technique, either flat sheets of material (i.e. geotextiles) or open grids (i.e. geogrids) are generally used as reinforcement and it is important to make the following distinction between the behaviour of these two types of materials. Under boundary conditions that ensure global plane strain deformation, the individual ribs in a geogrid will actually deform in plane stress, whereas a geotextile will deform in plane strain. In this formulation, the reinforcement is considered to be a flat sheet of material with the plane stress condition used to model a geogrid, and plane strain conditions for a geotextile. The adjustment that needs to be made between these two classes of behaviour is indicated in the description of the formulation.

This mathematical model does not allow slip to occur at the soil/reinforcement interface. This is an accurate description when the reinforcement is a geogrid which provides good interlock with the surrounding soil, but a rather less satisfactory assumption for a geotextile. This restriction means that the finite element solutions presented in this thesis should be interpreted as relating specifically to geogrids, or any other form of reinforcement which may be assumed to be perfectly rough.

5.2 Strain Definitions

In order to develop the relationships between strain rates and nodal velocities, consider a one-dimensional iso-parametric membrane element with N nodes. Each node has two degrees of freedom. The global co-ordinates of a point in the element are x, y and these are mapped onto a single reference co-ordinate α, as shown in Figure 5.1.

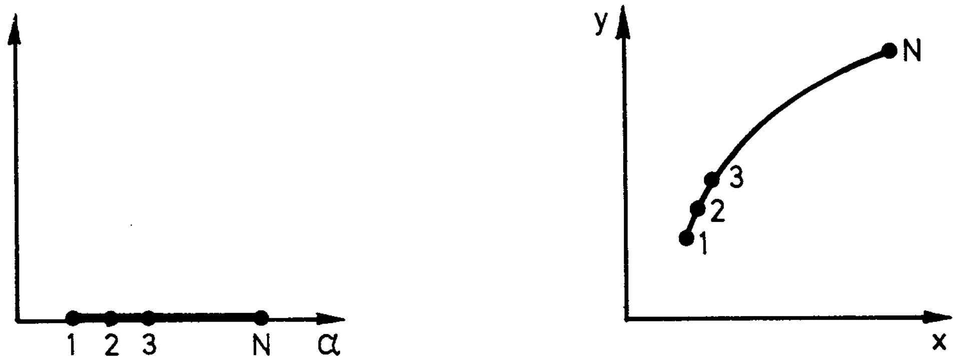

Reference Element

Parent Element

Figure 5.1: Mapping for Membrane Element

The vector of global co-ordinates of a typical point in the element, $\underset{\sim}{x}$, is related to the vector of global nodal co-ordinates $\underset{\sim}{X}$, by:-

$$\underset{\sim}{x} = [N]\,\underset{\sim}{X} \qquad (5.1)$$

where [N], the shape function matrix, is a function of α.

Figure 5.2 shows the displacement of an infinitesimal portion of the membrane during an infinitesimal time step dt. Cartesian co-ordinates are denoted by x, y and u, v are the velocities in the x, y directions.

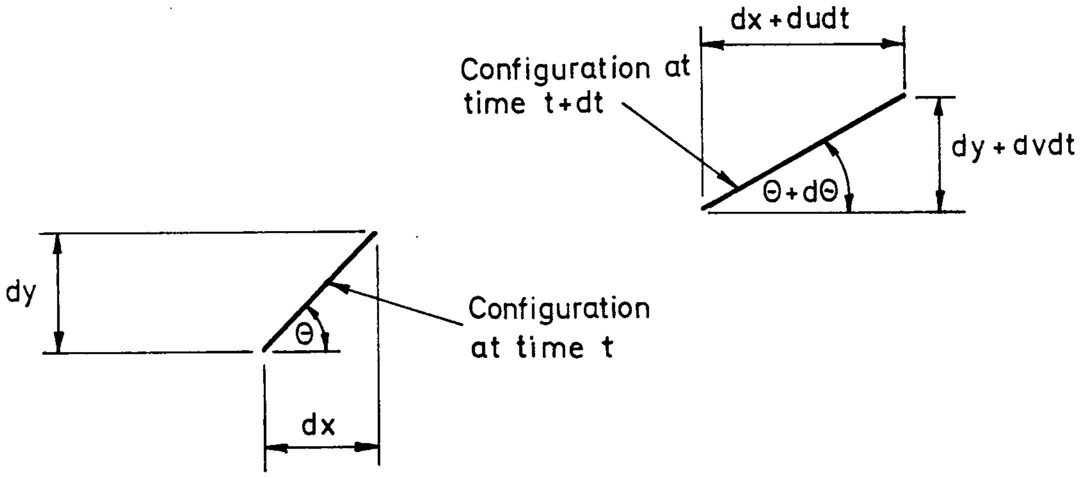

Figure 5.2: Displacements in a Membrane

The fractional increase in length of the portion is:-

$$\frac{\left[(dx + dudt)^2 + (dy + dvdt)^2\right]^{1/2} - \left[dx^2 + dy^2\right]^{1/2}}{\left[\ dx^2 + dy^2\ \right]^{1/2}}$$

$$= \frac{dxdu + dydv}{dx^2 + dy^2}\, dt \qquad (5.2)$$

where higher order displacement terms are ignored. The longitudinal Hencky strain rate, $\dot{\epsilon}_L$, can therefore be written:-

$$\dot{\epsilon}_L = \frac{d\epsilon_L}{dt} = \frac{\frac{dx}{d\alpha}\frac{du}{d\alpha} + \frac{dy}{d\alpha}\frac{dv}{d\alpha}}{\left[\frac{dx}{d\alpha}\right]^2 + \left[\frac{dy}{d\alpha}\right]^2} \qquad (5.3)$$

where the superior dot denotes differentiation with respect to time.

If $\underset{\sim}{u} = \begin{bmatrix} u \\ v \end{bmatrix}$ and $\underset{\sim}{x} = \begin{bmatrix} x \\ y \end{bmatrix}$ then:-

$$\dot{\epsilon}_L = \frac{(\underset{\sim}{u}')^T \underset{\sim}{x}'}{(\underset{\sim}{x}')^T \underset{\sim}{x}'} \qquad (5.4)$$

where the primes denote differentiation with respect to α.

From equation (5.1):-

$$\underset{\sim}{x}' = [N'] \underset{\sim}{X} \qquad (5.5)$$

also:-

$$\underset{\sim}{u}' = [N'] \underset{\sim}{U} \qquad (5.6)$$

where $\underset{\sim}{U}$ is the nodal velocity vector. Substituting equations (5.5) and (5.6) into equation (5.4) gives:-

$$\dot{\epsilon}_L = \frac{\underset{\sim}{U}^T [N']^T [N'] \underset{\sim}{X}}{\underset{\sim}{X}^T [N']^T [N'] \underset{\sim}{X}} \qquad (5.7)$$

In the rest of this chapter, the denominator of this expression will be denoted by J^2, where J can be interpreted as representing the Jacobian of the transformation from parent to reference co-ordinates.

It follows that:-

$$\dot{J} = \frac{\underset{\sim}{U}^T [N']^T [N'] \underset{\sim}{X}}{J} \qquad (5.8)$$

thus equation (5.7) can be written in the form:-

$$\dot{\epsilon}_L = \frac{\dot{J}}{J} \qquad (5.9)$$

This equation can be integrated exactly over a finite time increment Δt to give:-

$$\Delta\epsilon_L = \log_e \left[\frac{J_{t+\Delta t}}{J_t} \right] \qquad (5.10)$$

where $\Delta\epsilon_L$ is a finite Hencky strain increment at a point, $J_{t+\Delta t}$ is the value of the Jacobian calculated at the end of the load step, and J_t the value at the beginning.

From the principle of virtual work:-

$$\underset{\sim}{U}^T \underset{\sim}{P} = \int_E \dot{\epsilon}_L \, \sigma_L \, dV \qquad (5.11)$$

where $\underset{\sim}{U}^T$ are a set of virtual nodal velocities, and $\dot{\epsilon}_L$ is the compatible longitudinal strain rate. $\underset{\sim}{P}$ is the vector of nodal forces in equilibrium with the longitudinal stress, σ_L, and the integration is performed over the element.

The elemental volume dV may be written as:-

$$dV = A \, J \, d\alpha \qquad (5.12)$$

where A is the cross-sectional area of the membrane. Substituting equations (5.7) and (5.12) into the virtual work expression gives:-

$$\underset{\sim}{U}^T \underset{\sim}{P} = \int_E \frac{\underset{\sim}{U}^T [N']^T [N'] \underset{\sim}{X}}{J^2} \, \sigma_L A J \, d\alpha \qquad (5.13)$$

Since this expression must hold for arbitrary velocities $\underset{\sim}{U}^T$ it follows that:-

$$\underset{\sim}{P} = \int_E \frac{[N']^T [N'] \underset{\sim}{X}}{J} \, \sigma_L A \, d\alpha \qquad (5.14)$$

Differentiating equation (5.14) with respect to time, and noting that $\dot{\underset{\sim}{X}} = \underset{\sim}{U}$, gives the rate equation:-

$$\dot{\underset{\sim}{P}} = \int_E [N']^T[N'] \left[\frac{\underset{\sim}{U}\sigma_L}{J} + \frac{\underset{\sim}{X}\dot{\sigma}_L}{J} - \frac{\underset{\sim}{X}\sigma_L\dot{J}}{J^2} + \frac{\underset{\sim}{X}\sigma_L\dot{A}}{J\,A} \right] A\, d\alpha \tag{5.15}$$

For a membrane deforming in plane strain and assuming that stresses normal to the membrane are small compared to the in-plane stresses (i.e. that the membrane is thin), the longitudinal stress rate $\dot{\sigma}_L$ is related to the longitudinal strain rate by:-

$$\dot{\sigma}_L = \frac{E}{1 - \nu^2}\,\dot{\epsilon}_L \tag{5.16}$$

$$= \frac{E\,\underset{\sim}{X}^T[N']^T[N']\underset{\sim}{U}}{(1 - \nu^2)\,J^2} \tag{5.17}$$

where E is the Young's modulus of the membrane material, and ν is the Poisson's ratio.

The proportional area change can be written in terms of the longitudinal strain rate:-

$$\frac{\dot{A}}{A} = \frac{-\nu}{1 - \nu}\,\dot{\epsilon}_L \tag{5.18}$$

Equation (5.15) may be re-written using equations (5.8), (5.17) and (5.18) to give:-

$$\underset{\sim}{\dot{P}}=\int_E [N']^T[N'] \left[\frac{\sigma_L}{J} + \left\{ \frac{E}{(1-\nu^2)} - \sigma_L - \frac{\sigma_L \nu}{(1-\nu)} \right\} \frac{\underset{\sim}{X}\underset{\sim}{X}^T[N']^T[N']}{J^3} \right] A\,\underset{\sim}{U}d\alpha \quad (5.19)$$

Re-arranging the terms gives:-

$$\underset{\sim}{\dot{P}}=\int_E \left[\frac{[N']^T[N']\underset{\sim}{X}E^*\underset{\sim}{X}^T[N']^T[N'] + \sigma_L\left\{[N']^T J^2 [N'] - [N']^T[N']\underset{\sim}{X}\underset{\sim}{X}^T[N']^T[N']\right\}}{J^3} \right] A\underset{\sim}{U}d\alpha \quad (5.20)$$

where:-

$$E^* = \frac{E}{1-\nu^2} - \frac{\sigma_L \nu}{1-\nu} \quad (5.21)$$

For a membrane deforming in plane stress, then the longitudinal stress rate is related to the longitudinal strain rate by:-

$$\dot{\sigma}_L = E\,\dot{\epsilon}_L \quad (5.22)$$

and the proportional area change is:-

$$\frac{\dot{A}}{A} = -2\nu\,\dot{\epsilon}_L \quad (5.23)$$

In this case it may be shown that the nodal force rate is given by an expression of the form of equation (5.20), but with the modification:-

$$E^* = E - 2\nu\,\sigma_L \quad (5.24)$$

The second term of the integrand of equation (5.20) may be written:-

$$\sigma_L\left\{ [N']^T\left\{J^2[I] - [N']\underset{\sim}{X}\underset{\sim}{X}^T[N']^T\right\}[N'] \right\}A\underset{\sim}{U} \tag{5.25}$$

where [I] is the identity matrix. This may then be re-arranged as follows:-

$$J^2[I] - [N']\underset{\sim}{X}\underset{\sim}{X}^T[N']^T = [x' \; y']\begin{bmatrix} x' \\ y' \end{bmatrix}\begin{bmatrix} 1 & 0 \\ 0 & 1 \end{bmatrix} - \begin{bmatrix} x' \\ y' \end{bmatrix}[x' \; y'] \tag{5.26}$$

$$= \begin{bmatrix} y'^2 & -x'y' \\ -x'y' & x'^2 \end{bmatrix} \tag{5.27}$$

$$= [Z]\,\underset{\sim}{x'}\,\underset{\sim}{x'}^T[Z]^T \tag{5.28}$$

where [Z] is the matrix:-

$$[Z] = \begin{bmatrix} 0 & -1 \\ 1 & 0 \end{bmatrix} \tag{5.29}$$

which represents a 90° anti-clockwise rotation. The rate equation thus becomes:-

$$\underset{\sim}{\dot{P}} = \int_E \left[\frac{E^*[N']^T[N']\underset{\sim}{X}\underset{\sim}{X}^T[N']^T[N'] + \sigma_L[N']^T[Z][N']\underset{\sim}{X}\underset{\sim}{X}^T[N']^T[Z]^T[N']}{J^3}\right]\underset{\sim}{U}A\,d\alpha \tag{5.30}$$

which can be decomposed further into:-

$$\underset{\sim}{\dot{P}} = \int_E \left[[N']^T[N']\underset{\sim}{X} \quad [N']^T[Z][N']\underset{\sim}{X}\right]\begin{bmatrix} E^* & 0 \\ 0 & \sigma_L \end{bmatrix}\begin{bmatrix} \underset{\sim}{X}^T[N']^T[N'] \\ \underset{\sim}{X}^T[N']^T[Z]^T[N'] \end{bmatrix}\frac{\underset{\sim}{U}\,A\,d\alpha}{J^3} \tag{5.31}$$

The incremental element stiffness matrix may, therefore, be written:-

$$[K] = \int_E [B]^{*T}[D]^*[B]^* \, dV \tag{5.32}$$

where $[D^*]$ is the augmented stiffness matrix:-

$$[D]^* = \begin{bmatrix} E^* & 0 \\ 0 & \sigma_L \end{bmatrix} \tag{5.33}$$

and $[B^*]$ is the matrix:-

$$[B]^* = \frac{1}{J^2} \begin{bmatrix} \underset{\sim}{X}^T[N']^T[N'] \\ \underset{\sim}{X}^T[N']^T[Z]^T[N'] \end{bmatrix} \tag{5.34}$$

Equation (5.32) is a convenient expression for the incremental stiffness equation for two reasons. Firstly it is cast in exactly the same form as the usual small displacement equations, so that existing small displacement software could be fairly easily modified to use this formulation. Secondly, it is economical of computer time to evaluate the single expression of equation (5.32) rather than the equivalent four terms of equation (5.15).

In order to evaluate equation (5.32), it is necessary to calculate the value of A, the cross-sectional area of the membrane, at each of the Gauss points. This is best achieved by updating the Gauss point areas as the analysis proceeds. For plane <u>strain</u> conditions, equation (5.18) may be integrated to give:-

$$\log_e\left[\frac{A}{A_o}\right] = -\frac{\nu}{1-\nu}\,\Delta\epsilon_L \tag{5.35}$$

where A_o is the area at the start of the calculation step, A is the area at the end and $\Delta\epsilon_L$, the Hencky strain increment, is given by equation (5.10). For plane stress loading, the appropriate rate relationship is equation (5.23) which is integrated to give:-

$$\log_e\left[\frac{A}{A_o}\right] = -2\nu\,\Delta\epsilon_L \qquad (5.36)$$

The [B] matrix generally relates a nodal velocity vector $\underset{\sim}{U}$ to a strain rate vector $\underset{\sim}{\dot{\epsilon}}$ in an equation of the form:-

$$\underset{\sim}{\dot{\epsilon}} = [B]\,\underset{\sim}{U} \qquad (5.37)$$

If this equation is expanded using the $[B]^*$ matrix derived earlier, then the resulting strain rate vector is:-

$$\underset{\sim}{\dot{\epsilon}} = \frac{1}{J^2}\begin{bmatrix} x'u' + y'v' \\ -y'u' + x'v' \end{bmatrix} \qquad (5.38)$$

It is useful to consider the significance of the two terms in the new strain rate vector. The first term represents the longitudinal strain rate $\dot{\epsilon}_L$, from equation (5.4). The second term can be identified with anti-clockwise rotation rate. The nodal force rate can therefore be partly associated with longitudinal straining, and partly with element rotation.

In general, it is necessary to use a numerical integration method to evaluate the element stiffness matrix. It should be noted, however, that severe element distortions can lead to excessive errors in this integration, and that the accuracy may be improved by increasing the number of Gauss points (see Section 2.2.4). In the computations described in this thesis, the three-noded element has been used with a three-point Gaussian integration rule (note that two Gauss points are sufficient for the case when the Jacobian does not vary along the element). To ensure that the element distortions do not become too large for this integration rule to be accurate, the Jacobian variation parameter, defined by equation (2.39), is monitored for each element as the calculation proceeds.

The finite element equations for the specific case of the three-noded element are given in Appendix 5A.

5.4 Stress Update Calculations

In order to perform a general equilibrium check at the end of the calculation increment, it is necessary to calculate the updated Gauss point stresses. This is achieved by integrating the appropriate constitutive equations and is a considerably simpler procedure than the equivalent calculation for two-dimensional elements (see Chapter 4).

For plane strain conditions, equation (5.16) may be integrated to give:-

$$\sigma_L = \sigma_{Lo} + \frac{E}{1 - \nu^2} \Delta\epsilon_L \qquad (5.39)$$

where σ_{Lo} is the longitudinal Gauss point stress at the start of the calculation increment, σ_L is the stress at the end and $\Delta\epsilon_L$ is given by equation (5.10). For plane stress loading the appropriate rate relationship is equation (5.22) which is integrated to give:-

$$\sigma_L = \sigma_{Lo} + E\,\Delta\epsilon_L \tag{5.40}$$

Since this membrane element has zero bending stiffness, it is appropriate to assume that it can sustain no compression since it would buckle. It is also necessary to ensure that the possibility of tensile stresses re-occurring during the analysis is accounted for. In this formulation therefore, the first step in the 'stress-update' calculation is to compute the updated Hencky strain (from equation (5.10)). If this is positive, then the updated stress is calculated using the appropriate elastic relationship. If the Hencky strain is negative, then the Gauss point stress is set to zero.

5.5 Calculation of Interface Stresses

In order to investigate the mechanism of reinforcement in an unpaved road it is necessary to calculate the stresses acting at the interface of the reinforcement and the surrounding soil. In this thesis, the interface stresses are calculated from the nodal forces that are consistent with the internal stresses in the neighbouring continuum elements.

Consider the edge of the six-noded continuum element with normal stress p, and tangential stress q shown in Figure 5.3. If F_{ix} is the force at node i in the x direction equivalent to the stresses in the element, then from the principle of virtual work:-

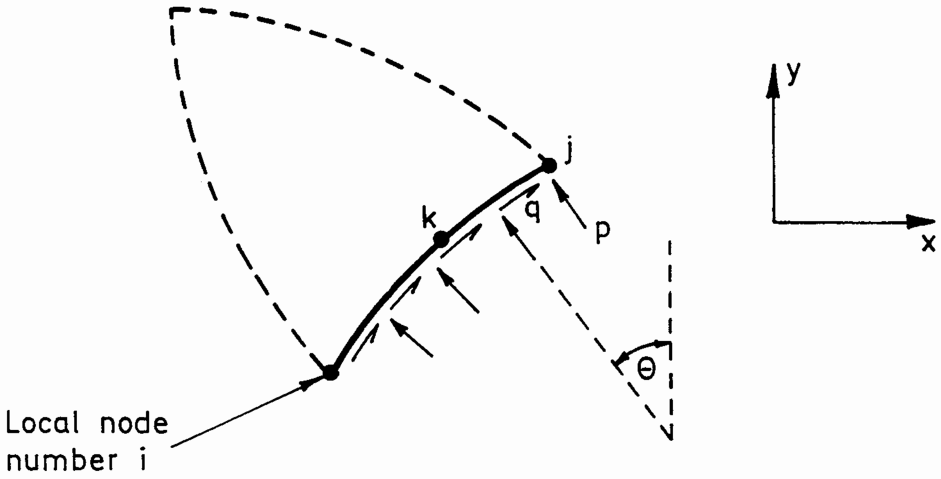

Figure 5.3: Interface Stresses for the Six-Noded Triangle

$$F_{ix} = \int \left[q \cos(\theta) - p \sin(\theta)\right] f_i \, ds \qquad (5.41)$$

similarly:-

$$F_{iy} = \int \left[p \cos(\theta) + q \sin(\theta)\right] f_i \, ds \qquad (5.42)$$

where f_i is the shape function associated with node i and the integration is performed over the edge of the element.

For the case of the six-noded triangle, the nodal forces that are consistent with the internal stresses may be used to define a linear variation of interface stress along each element side. Six nodal forces act on any given element edge; two of these (corresponding to the mid-side node) are associated with interface stresses acting on one side of the element and the remaining four (corresponding to the corner nodes) are associated with stresses acting on two sides. In order to calculate linear variations of interface stress, it is necessary to compute the proportions of the corner nodal forces that correspond to the stresses acting on the element side of interest. This introduces a complication into the calculation that is avoided if the mid-side nodal forces are used to define a constant interface stress, which is the approach used in this formulation. On this basis, the relationship between the interface stresses and the forces associated with the node at the mid-side of the edge is:-

$$q = \frac{3}{2} \frac{F_{kx}(X_j - X_i)^2 + F_{ky}(Y_j - Y_i)^2}{(X_j - X_i)^2 + (Y_j - Y_i)^2} \tag{5.43}$$

$$p = \frac{3}{2} \frac{F_{ky}(X_j - X_i)^2 - F_{kx}(Y_j - Y_i)^2}{(X_j - X_i)^2 + (Y_j - Y_i)^2} \tag{5.44}$$

It should be noted that this approach does not evaluate correctly the component of interface stress due to material self weight. This simple method has been adopted in this thesis, however, on the basis that in the reinforced unpaved road the effect of material self weight on the soil reinforcement interface stresses is negligible.

APPENDIX 5A

Finite Element Equations for the Three-Noded Membrane Element

Consider the iso-parametric mapping between the parent and reference elements shown in Figure 5A.1.

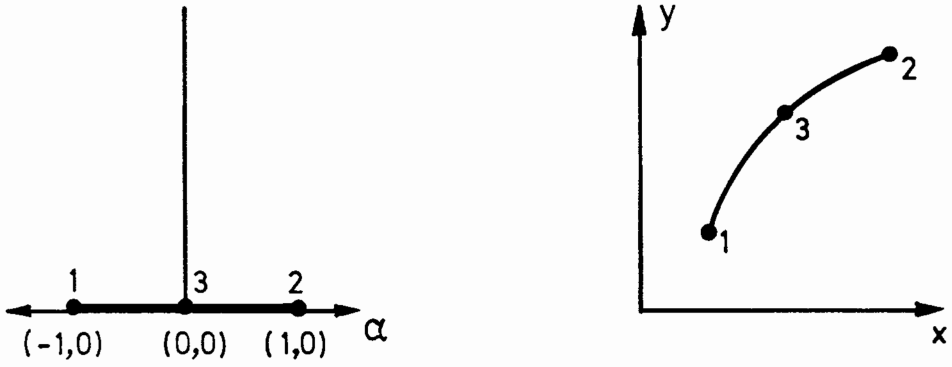

Reference Element

Parent Element

Figure 5A.1: Mapping for Three-Noded Membrane Element

The vectors $\underset{\sim}{x}$ and $\underset{\sim}{X}$ appearing in equation 5.1 are defined as:-

$$\underset{\sim}{x} = \begin{bmatrix} x \\ \\ y \end{bmatrix} \qquad \underset{\sim}{X} = \begin{bmatrix} X_1 \\ Y_1 \\ X_2 \\ Y_2 \\ X_3 \\ Y_3 \end{bmatrix} \qquad (5A.1)$$

where X_i, Y_i are the global co-ordinates of the i^{th} node. In this case the shape function matrix is:-

$$[N] = \begin{bmatrix} f_1 & o & f_2 & o & f_3 & o \\ o & f_1 & o & f_2 & o & f_3 \end{bmatrix} \qquad (5A.2)$$

where:-

$$f_1 = \frac{-\alpha}{2}(1 - \alpha) \qquad f_2 = \frac{\alpha}{2}(1 + \alpha) \qquad f_3 = (1 + \alpha)(1 - \alpha) \qquad (5A.3)$$

The matrix $[B]^*$ defined by equation (5.31) is given by:-

$$[B]^* = \begin{bmatrix} x'f_1' & y'f_1' & x'f_2' & y'f_2' & x'f_3' & y'f_3' \\ -y'f_1' & x'f_1' & -y'f_2' & x'f_2' & -y'f_3' & x'f_3' \end{bmatrix} \qquad (5A.4)$$

where:-

$$J^2 = (x')^2 + (y')^2 \qquad (5A.5)$$

and the primes denote differentiation with respect to α.

CHAPTER 6 VERIFICATION OF THE FINITE ELEMENT PROGRAM

6.1 Introduction

In any calculations involving computational methods, it is important that the mathematical formulation and the corresponding computer code be rigorously checked against test problems which have known solutions. This procedure is of added importance for the large displacement calculations presented in this thesis, since predictions are made that fall well outside the usual scope of finite element analysis of problems in Soil Mechanics.

In addition to acting as a general check on the correctness of the computer code, a systematic study of test cases such as these can give a useful insight into the limitations of the numerical techniques and models chosen for the analysis. The simple shear problem, for example, which is described in Section 6.3, illustrates the limitations of the Jaumann stress rate for large strain computations. The nature of the Jaumann stress rate in the context of this particular problem is discussed in greater depth in Section 2.2.2.

Three groups of test problems are described in this section. The first set of problems involve deformations that are homogeneous and have closed form solutions even for the finite deformation case. This first group includes finite compression, shear and extension problems for an elasto-plastic continuum (Sections 6.2 to 6.5) and a large extension, large rotation problem for a plane strain membrane (Section 6.6). Secondly, the results of a large strain cavity expansion analysis are presented. This is a rare example of a large strain problem which involves non-homogeneous deformations but has a known analytic solution. Thirdly, the results of a series of small strain collapse load calculations are described. Since the analysis of an unpaved road is essentially a large strain collapse problem, it is vital that the finite element formulation is first used to make a study of the small strain cases in order to develop confidence in the large strain predictions.

The usual tension-is-positive convention has been adopted in this chapter, with the exception of the derivation of closed form solutions to the compression problems described in Section 6.2 in which compression is reckoned positive in order to clarify the presentation of the diagrams.

6.2 Finite Homogeneous Compression

The use of simple homogeneous deformation test problems to check the implementation of large plane strain finite element formulations was first suggested by Osias and Swedlow (1974) who presented a test case involving finite homogeneous extension with zero initial stresses. This test case was developed by Carter (1977) to include finite compression as well as the effect of initial stress. In this latter work, a solution is obtained for the elastic perfectly-plastic case, with the plastic behaviour defined by a model based on the Mohr-Coulomb yield criterion.

In this section, a series of finite homogeneous compression test problems is described. Compression rather than extension has been chosen for study since this is the type of behaviour that generally occurs in problems in Soil Mechanics. The analytical solutions for elastic material behaviour are the same as those derived by Carter (1977) and are developed here to include the elasto-plastic case for both the von Mises and Matsuoka plasticity models described in Section 3.5.

In all these test problems the responses are highly non-linear and depend on the initial stresses. These non-linearities arise because of the large displacement effects involved in these calculations and may be understood in terms of a simple example. Consider a compression analysis in which an initial lateral compressive stress exists and axial compression is applied. As the axial length reduces, then for zero change in the lateral force the lateral compressive stress must increase thus introducing a non-linearity into the analysis. The behaviour described by this analysis may well not be representative of any real process, but this procedure is of considerable use in testing the finite element formulation and the solution algorithm.

In all these homogeneous deformation calculations, the material has a square elevation at the start of the analysis. A symmetrical finite element mesh consisting of four six-noded triangles formed from the diagonals of the square is used as the basis of the numerical calculation. This mesh is adopted instead of a simpler mesh consisting of two triangular elements, since the asymmetry of this latter arrangement can lead to inaccurate results.

6.2.1 Elastic Behaviour

In this calculation, increments of compressive force which cause large deformations are applied to an elastic material.

Consider the square section of unit depth with initial compressive forces in the x and y directions of P_o and Q_o respectively shown in Figure 6.1. During the deformation, which occurs over a time interval T, Q_o is increased to Q but P_o is held constant.

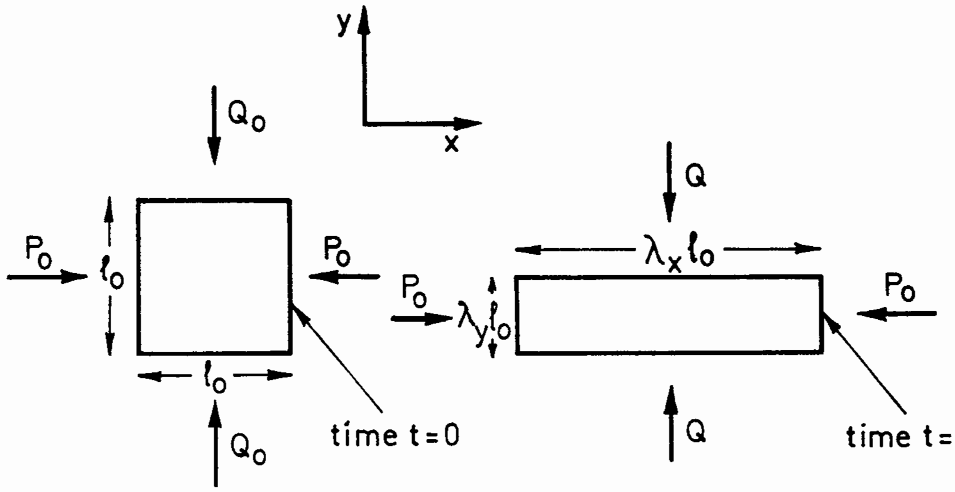

Figure 6.1: Homogeneous Compression

The plane strain rate equations of elasticity are:-

$$\dot{\sigma}_{xx} = \frac{E}{(1+\nu)(1-2\nu)} \left[(1-\nu)\,\dot{\epsilon}_{xx} + \nu\,\dot{\epsilon}_{yy}\right] \tag{6.1}$$

$$\dot{\sigma}_{yy} = \frac{E}{(1+\nu)(1-2\nu)} \left[(1-\nu)\,\dot{\epsilon}_{yy} + \nu\,\dot{\epsilon}_{xx}\right] \tag{6.2}$$

Integrating these equations with respect to time gives:-

$$\sigma_{xx} = \frac{-E}{(1+\nu)(1-2\nu)} \left[(1-\nu)\log_e(\lambda_x) + \nu\log_e(\lambda_y)\right] + \frac{P_o}{l_o} \tag{6.3}$$

$$\sigma_{yy} = \frac{-E}{(1+\nu)(1-2\nu)} \left[(1-\upsilon)\ \log_e(\lambda_y) + \upsilon\ \log_e(\lambda_x)\right] + \frac{Q_o}{l_o} \qquad (6.4)$$

where the extension ratios in the x and y directions, λ_x and λ_y, are defined:-

$$\int_0^T \dot{\epsilon}_{xx}\, dt = -\log_e(\lambda_x) \quad \text{and} \quad \int_0^T \dot{\epsilon}_{yy}\, dt = -\log_e(\lambda_y) \qquad (6.5)$$

If the force in the x direction is held constant, then:-

$$P_o = \sigma_{xx}\, \lambda_y\, l_o \qquad (6.6)$$

Substituting equation (6.6) into (6.3) gives:-

$$\lambda_x = \exp\left[\frac{P_o\ (\lambda_y - 1)}{\mu\ \lambda_y l_o (1-\nu)} - \frac{\upsilon}{1-\upsilon}\ \log_e(\lambda_y)\right] \qquad (6.7)$$

where:-

$$\mu = \frac{E}{(1+\nu)(1-2\nu)} \qquad (6.8)$$

Given that $Q = \sigma_{yy} l_o \lambda_x$, equations (6.4) and (6.7) together define the relationship between Q and λ_y. This relationship is plotted with the results of finite element calculations for the same problem in Figure 6.2, for three different values of P_o. In the finite element calculations, prescribed displacements were applied to the upper boundary in such a way that the increment of $(1/\lambda_y)$ was held constant ot 0.28 for each calculation step. Figure 6.2 shows that in this case, the numerical and analytical solutions are almost identical.

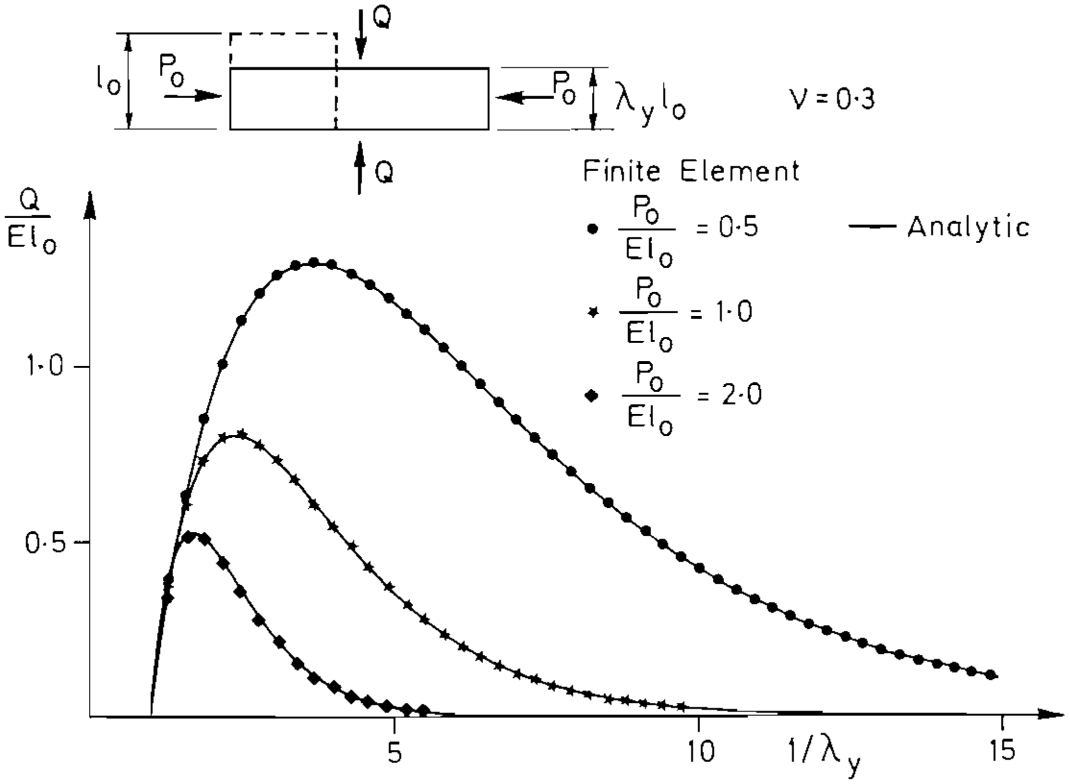

Figure 6.2: Homogeneous Elastic Compression

6.2.2 Elastic Perfectly-Plastic Behaviour: von Mises Plasticity

Consider again the initially square section of Figure 6.1. In order to obtain a simple analytical solution to the homogeneous compression problem for the elasto-plastic case it is necessary to ensure that the elastic strain rates are zero after yielding has occurred. For the case of von Mises plasticity with an associated flow rule, this condition is only satisfied if the Poisson's ratio is 0.5 (see Section 3.5.1). Since the Poisson's ratio cannot be set exactly to 0.5 if the bulk modulus is to remain finite, a slightly lower value must be used which means that in the finite element solution the condition of zero elastic volumetric strain is only approximately satisfied.

In the test calculation described here, the square section is initially stress free and is loaded in the y direction only. The elastic rate equations, therefore, reduce to:-

$$\dot{\sigma}_{xx} = 0 \tag{6.9}$$

$$\dot{\sigma}_{yy} = \frac{E}{1-\nu^2} \dot{\epsilon}_{yy} \tag{6.10}$$

$$\dot{\sigma}_{zz} = \nu \dot{\sigma}_{yy} \tag{6.11}$$

Integrating equations (6.9), (6.10) and (6.11) gives:-

$$\sigma_{xx} = 0 \tag{6.12}$$

$$\sigma_{yy} = - \frac{E}{1-\nu^2} \log_e(\lambda_y) \tag{6.13}$$

$$\sigma_{zz} = \nu \sigma_{yy} \tag{6.14}$$

where the extension ratio λ_y is defined in equation (6.5). Substitution of equations (6.12) and (6.14) into the von Mises yield function (equation (3.33)) gives the value of σ_{yy} at which yield will initially occur:-

$$\sigma_{yy} = \frac{\pm 2c}{(1 - \nu + \nu^2)^{1/2}} \tag{6.15}$$

If the Poisson's ratio is taken to be 0.5, then in both the elastic and plastic regimes the extension ratios are related by the constant volume condition:-

$$\lambda_x \lambda_y = 1 \tag{6.16}$$

The load in the y direction is:-

$$Q = \sigma_{yy} \lambda_x l_o \tag{6.17}$$

Thus in the elastic regime from equations (6.13), (6.16) and (6.17):-

$$Q = -\frac{4E}{3\lambda_y} \log_e(\lambda_y) \tag{6.18}$$

and in the plastic regime, from equations (6.15), (6.16) and (6.17) (taking the positive solution in equation (6.15)):-

$$Q = \frac{4c}{\sqrt{3}\,\lambda_y} \tag{6.19}$$

The relationship between Q and λ_y, defined by equations (6.18) and (6.19) is plotted in Figure 6.3 for three different values of (E/c). The results of finite element calculations, in which a Poisson's ratio of 0.495 is used to approximate the incompressibility condition, have been plotted for comparison. Since the condition of zero elastic volumetric strains is only enforced approximately in the finite element calculation, the agreement with the analytical relationship is not exact. The effects of this approximation are most apparent for E/c = 0 (corresponding to an infinite strength) which is to be expected since in this particular calculation the material behaviour is wholly elastic. As E/c increases, the response becomes dominated by plastic behaviour for which the incompressibility condition is enforced exactly in the finite element solution thus the errors are reduced. In spite of the fact that in this case the finite element solution is inexact, this test does act as a general check on the implementation of the von Mises model.

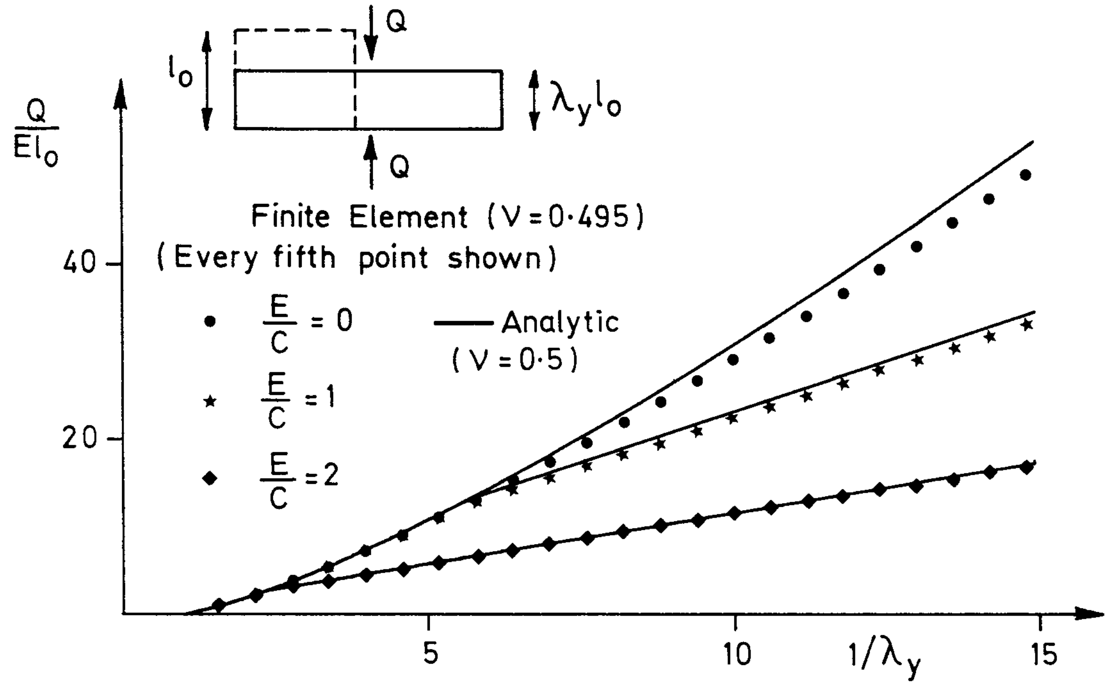

Figure 6.3: Homogeneous Compression, von Mises Plasticity

6.2.3 Elastic Perfectly-Plastic Behaviour: Matsuoka Plasticity

In this test problem a square element having initial compressive stresses is sheared by imposing additional tensile forces in the y direction. For the case when the in-plane compressive stresses are equal and the out-of-plane stress is given by the elastic plane strain condition then:-

$$\sigma_{xo} = \sigma_o \qquad (6.20)$$

$$\sigma_{yo} = \sigma_o \tag{6.21}$$

$$\sigma_{zo} = 2\nu\, \sigma_o \tag{6.22}$$

where σ_{xo}, σ_{yo} and σ_{zo} are the initial stresses in the x, y and z directions and σ_o is a constant. If a tensile force increment is applied in the y direction with zero force increment in the x direction, then from the geometry of Figure 6.1 and from equation (6.7), the extension ratios in the elastic regime are related by:-

$$\lambda_x = \exp\left[\frac{\sigma_o(\lambda_y - 1)}{\mu\, \lambda_y(1-\nu)} - \frac{\nu}{1-\nu}\log_e(\lambda_y)\right] \tag{6.23}$$

and the force in the y direction is:-

$$Q = \sigma_{yy}\, \lambda_x\, l_o \tag{6.24}$$

where λ_x is given by equation (6.23) and σ_{yy} is obtained by combining equations (6.23) and (6.4):-

$$\sigma_{yy} = -\frac{\nu\, \sigma_o(\lambda_y - 1)}{\lambda_y(1-\nu)} - \frac{\mu}{1-\nu}(1-2\nu)\log_e(\lambda_y) \tag{6.25}$$

In order to obtain a simple analytic solution for the load/displacement response when the material has yielded, it is again necessary to choose a set of parameters which ensure that the elastic strain rates are zero in the plastic regime. For this to be the case, the out-of-plane stress must be the same function of the in-plane stresses for both elastic and fully plastic behaviour.

The value of the out-of-plane stress when the deformation is plastic is a function of the dilation characteristics of the model (see Section 3.5.2) and can only be obtained in closed form for the full association or the zero dilation cases discussed in Section 3.5.2. Since zero dilation provides a more severe test of the formulation it is adopted here for the purpose of this particular test problem.

For the in-plane stresses to lie on the yield surface:-

$$\sigma_1 = \frac{(\sigma_1 + \sigma_3)}{2}\left[1 + \sin(\phi_{ps})\right] \tag{6.26}$$

$$\sigma_3 = \frac{(\sigma_1 + \sigma_3)}{2}\left[1 - \sin(\phi_{ps})\right] \tag{6.27}$$

where ϕ_{ps} is the plane strain friction angle and σ_1, σ_3 are the in-plane principal stresses. Thus, from equation (3.48) the out-of-plane stress for the case of zero elastic strain rate is:-

$$\sigma_2^2 = \frac{\left[\sigma_1 + \sigma_3\right]^2\left[\sin^2(\phi_{ps}) - 1\right]^2}{4\left[1 + \sin^2(\phi_{ps})\right]} \tag{6.28}$$

For the out-of-plane stress to be the same function of stress ratio in both the elastic regime at initial yield and the fully plastic regime, the required Poisson's ratio is given by:-

$$\nu^2 = \frac{\left[\sin^2(\phi_{ps}) - 1\right]^2}{4\left[1 + \sin^2(\phi_{ps})\right]} \tag{6.29}$$

The Matsuoka plasticity model described in Section 3.5.2 is based on the use of the triaxial compression friction angle to define the yield surface. It is therefore necessary to use equation (6.29) in conjunction with equation (3.49) to obtain a set of consistent values of ν and ϕ. For the purposes of this example, the following parameters have been chosen:-

$$\phi = 31.04^\circ \qquad \nu = 0.3 \qquad \phi_{ps} = 34.0^\circ$$

If material parameters are chosen that satisfy equations (6.29) and (3.49), then initial yield will occur when the stresses are related by:-

$$\sigma_{yy} = \sigma_{xx} \frac{\left[1 - \sin(\phi_{ps})\right]}{\left[1 + \sin(\phi_{ps})\right]} \tag{6.30}$$

where in this case, since the force in the x direction is constant:-

$$\sigma_{xx} = \frac{\sigma_o}{\lambda_y} \tag{6.31}$$

Equations (6.31), (6.30), (6.25) and (6.23) can therefore be used to calculate $\lambda_y^{(y)}$ and $\lambda_x^{(y)}$, which are the values of the extension ratios λ_x and λ_y at initial yield. Since the material properties are chosen to ensure that elastic strain rates are zero after initial yield and that the plastic volumetric strain rate is zero, the area remains constant after yield has occurred. In the plastic regime therefore, the extension ratios λ_x and λ_y are related by the expression:-

$$\lambda_x \lambda_y = \lambda_x^{(y)} \lambda_y^{(y)} \tag{6.32}$$

The in-plane stresses are given by equations (6.30) and (6.31), and the force Q is given by the expression:-

$$Q = \frac{\sigma_o \left[1 - \sin(\phi_{ps})\right] \left[\ \lambda_y^{(y)} \quad \lambda_x^{(y)}\right]}{(\lambda_y)^2 \left[1 + \sin(\phi_{ps})\right]} \tag{6.33}$$

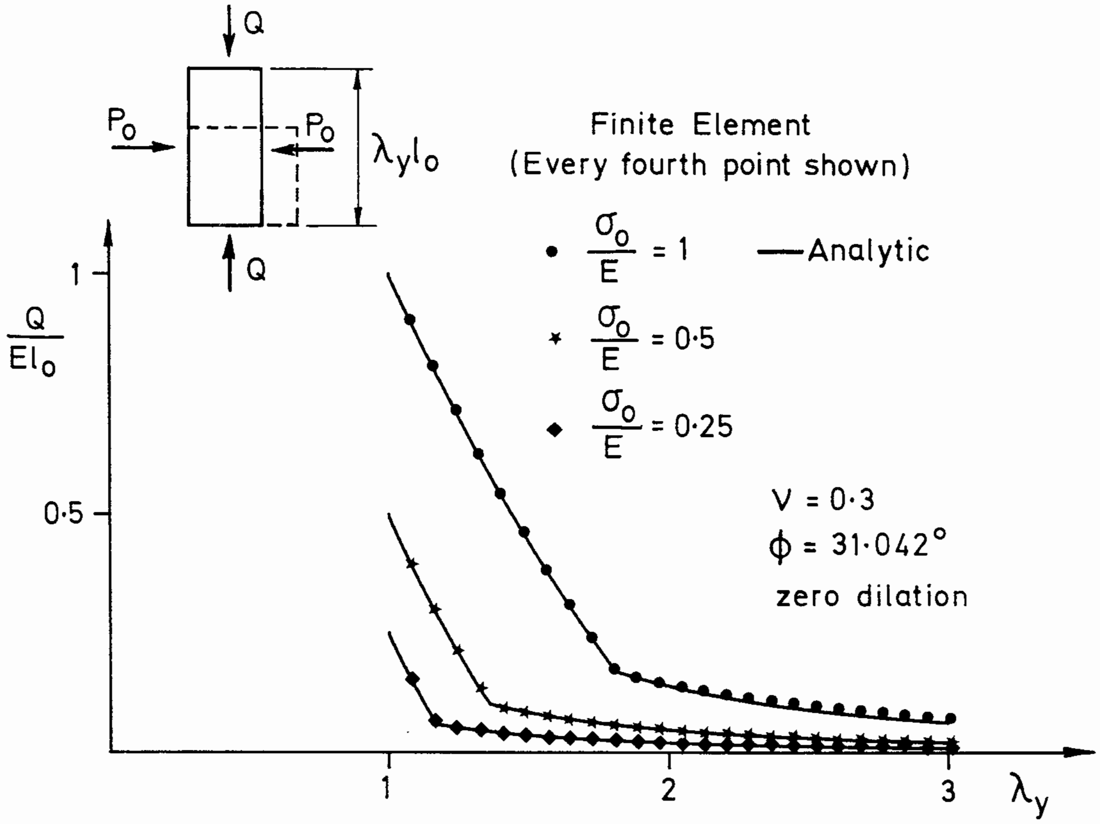

Figure 6.4: Homogeneous Compression, Matsuoka Plasticity

The analytical procedure described in this section may be used to calculate the relationship between Q and λ_y for this particular test problem. This relationship has been plotted in Figure 6.4 for three values of initial stress, and compared with the results of the corresponding finite element calculations.

6.3 Finite Homogeneous Shear

This test case, first proposed by Osias and Swedlow (1974), is used here to check the implementation of the Jaumann stress rate in the finite element formulation. The simple shear test problem is also of considerable interest in illustrating the limitations of the Jaumann stress rate in large displacement computations, and in this context is discussed in Section 2.2.2. The original solution to the simple shear problem described by Osias and Swedlow (1974) was for the case of zero initial stress. This solution is generalized in Section 2.2.2, and used here to check the results of a finite element analysis of this problem.

The equations relating shear displacements to the in-plane stresses derived in Section 2.2.2 (equations (2.28), (2.29) and (2.30)) are plotted in Figure 6.5 for the case of zero initial stress and Figure 6.6 for the case when one of the initial stresses is non-zero. Finite element solutions to these problems are superimposed on these plots. The numerical solutions, which agree well with the exact curves, were obtained by providing a total of 25 displacement steps to the initially square element to provide constant increments of tan(γ).

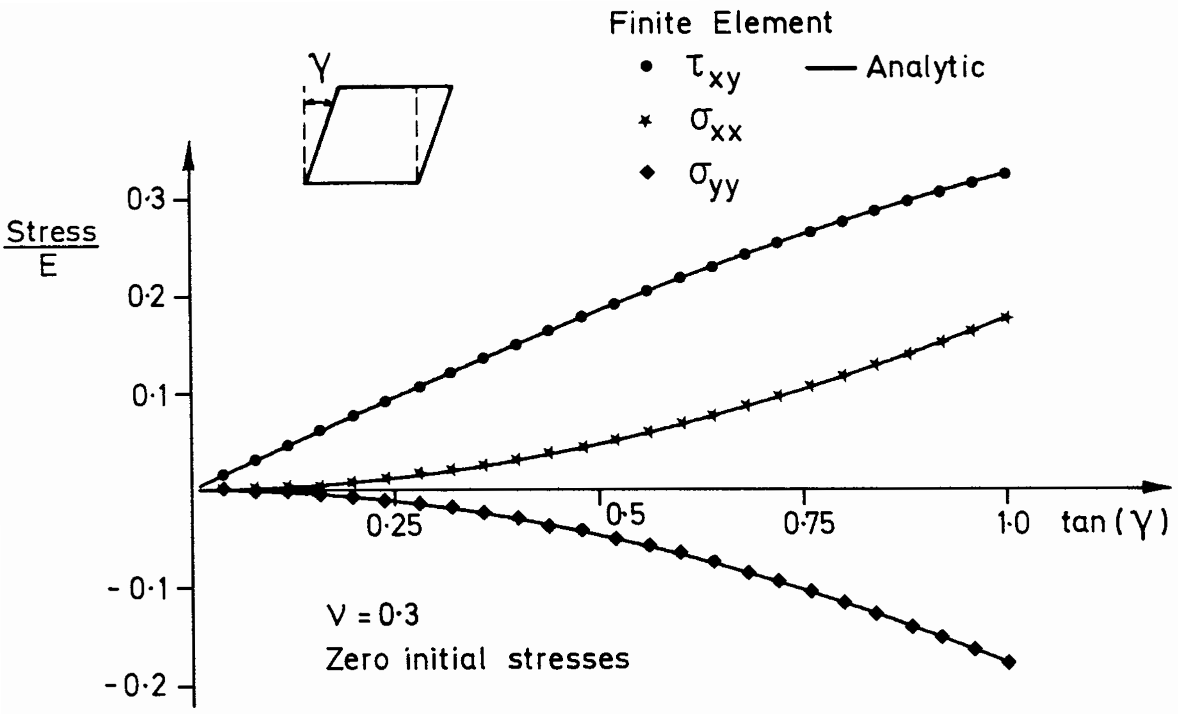

Figure 6.5: Simple Shear with Zero Initial Stress

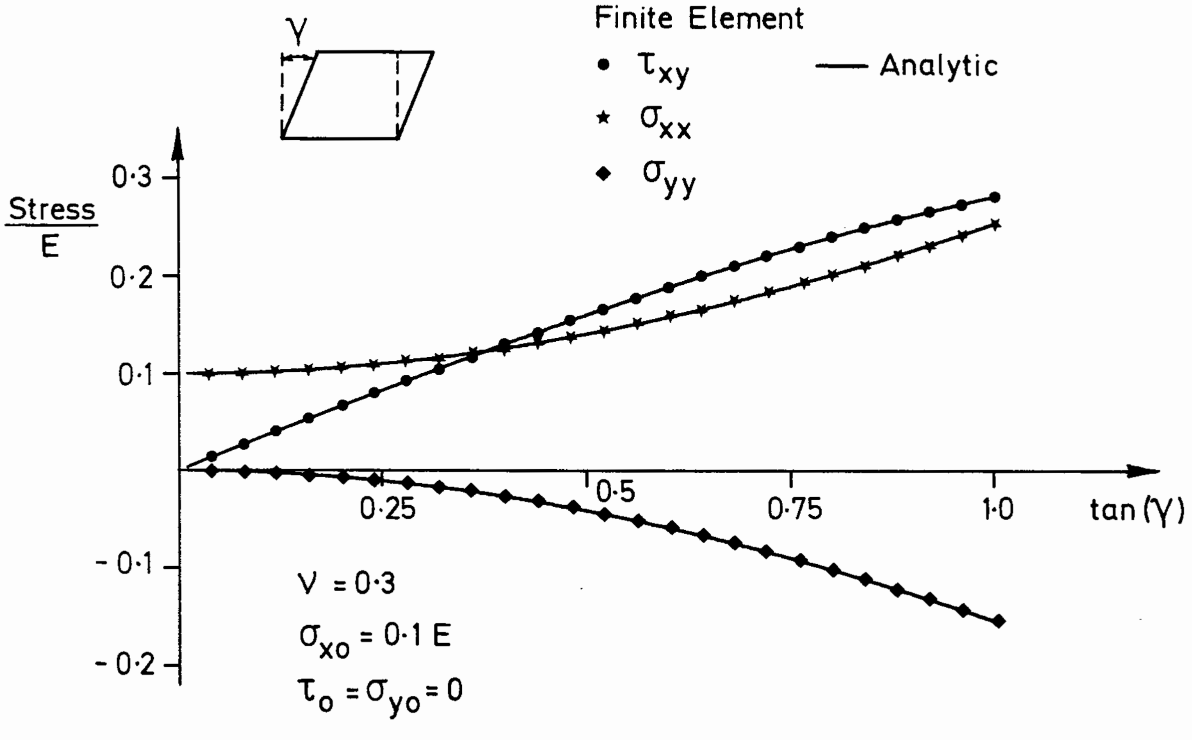

Figure 6.6: Simple Shear with Initial Stress

6.4 Simultaneous Rotation and Extension: Elasticity

This test problem was used as an additional check on the implementation of the Jaumann stress rate, and consists of the analysis of an element of material that is simultaneously rotated and extended.

Displacements are imposed on the boundary of the square section shown in Figure 6.7 such that sides A remain the same length, sides B increase in length by a factor λ_y and the section rotates through a clockwise angle θ. The section is subjected to an initial force in the x direction of P_o.

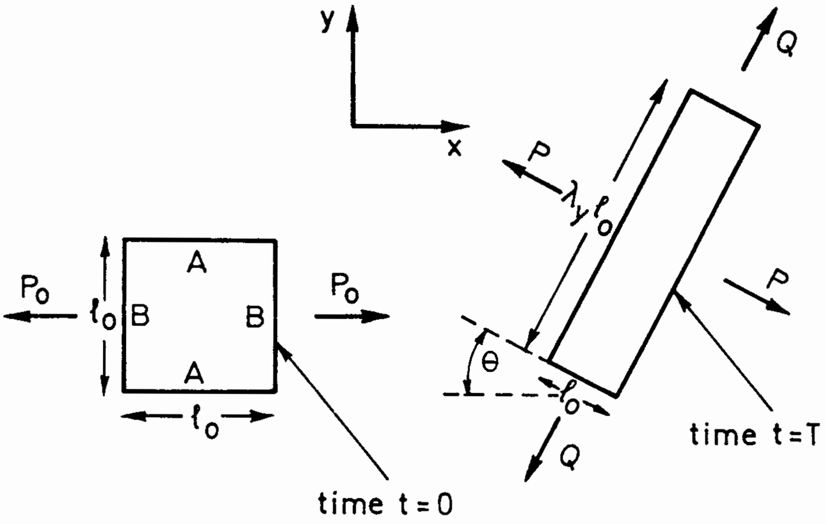

Figure 6.7: Simultaneous Rotation and Extension

From equations (6.3) and (6.4), adopting the convention that tensile forces are positive, the in-plane forces are given by:-

$$P = \mu \nu \log_e(\lambda_y) l_o \lambda_y + P_o \lambda_y \tag{6.34}$$

$$Q = \mu (1-\nu) \log_e(\lambda_y) l_o \tag{6.35}$$

where μ is defined by equation (6.8). The relationship defined by equations (6.34) and (6.35) is plotted and compared with the corresponding finite element solution in Figure 6.8 for one particular case of initial force.

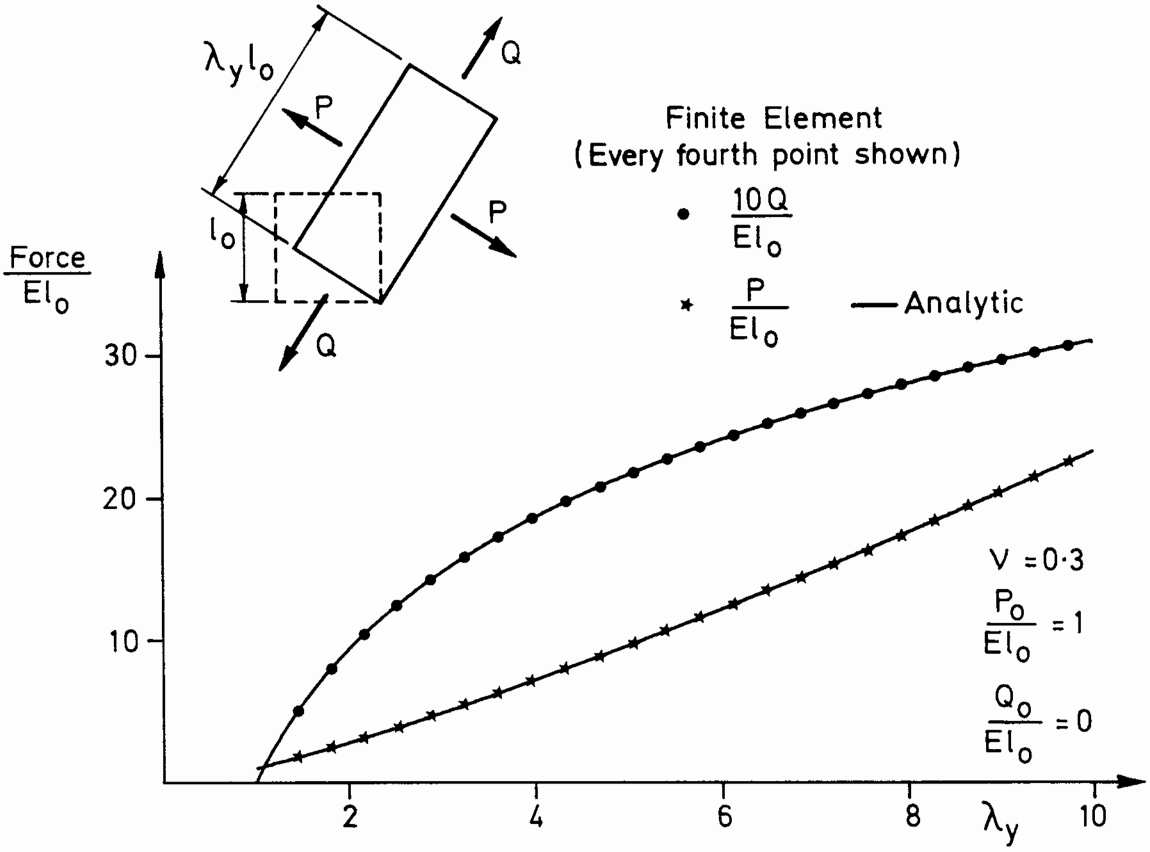

Figure 6.8: Simultaneous Rotation and Extension

6.5 An Elastic Unloading Test Problem: von Mises Plasticity

In this test problem, an element of material is first compressed and then expanded, with a rotation superimposed on the deformation.

Consider a square section which has linear displacements prescribed to the corners such that it is caused to rotate through 90° as shown in

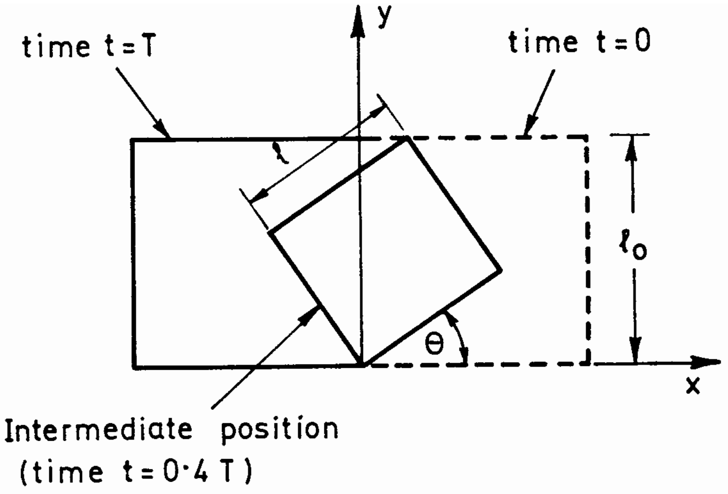

Figure 6.9: Simultaneous Rotation and Compression

Figure 6.9. The section retains its square shape during the deformation, but in-plane stresses arise due to the changes in area. Clearly in this case the two in-plane principal stresses are equal, and for the case of von Mises plasticity, the plastic volumetric strains are zero. Since after the first 45^{o} of rotation the area of the section increases, this test case may be used to check the finite element formulation under conditions of elastic unloading by choosing material parameters for which yielding occurs during the compression phase.

The elastic behaviour may be defined in terms of the mean pressure and volumetric strain, and the deviatoric stresses and strains:-

$$\dot{p} = K \dot{v} \tag{6.36}$$

$$\dot{s}_{xx} = 2G \dot{e}_{xx} \tag{6.37}$$

$$\dot{s}_{yy} = 2G \dot{e}_{yy} \tag{6.38}$$

Jaumann terms are absent in these equations since the in-plane principal stresses are equal.

For the case of zero initial stress, these equations may be integrated to give:-

$$p = K\, v \tag{6.39}$$

$$s_{xx} = 2G\, e_{xx} \tag{6.40}$$

$$s_{yy} = 2G\, e_{yy} \tag{6.41}$$

Substituting equations (6.40) and (6.41) into the von Mises yield function (equation (3.33)), and noting that in this case the in-plane deviatoric strains are equal gives the position of the element at which yielding will initially occur:-

$$\log_e \left\{\frac{l}{l_o}\right\} = -\frac{c}{G} \tag{6.42}$$

The in-plane deviatoric stresses at the onset of yield are:-

$$s_{xx} = s_{yy} = \frac{-2c}{3} \tag{6.43}$$

and will remain constant while the deformation remains plastic. Thus, if yield occurs during the first 45° of rotation (i.e. if $2c < G \log_e(2)$) then the deviatoric stresses are given by equation (6.43) at the mid-point of the deformation. As the rotation is continued, the section expands and elastic unloading occurs. At the end of the deformation, therefore, the in-plane deviatoric stresses may be obtained by integrating equations (6.37) and (6.38), with the initial stresses given by equation (6.43):-

$$s_{xx} = s_{yy} = G \log_e(2) - \frac{2c}{3} \qquad (6.44)$$

The mean pressure will, of course, be zero at the end point of the calculation.

The finite element formulation has been checked using this test problem, but since the numerical and analytical solutions are indistinguishable when plotted, the results of these calculations are not presented here.

6.6 A Membrane Element Test Problem

In this test problem, simultaneous rotation and extension is applied to two plane-strain membrane elements as shown in Figure 6.10.

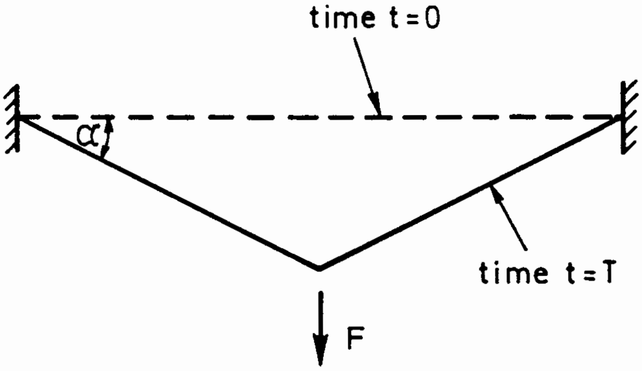

Figure 6.10: Membrane Element Test Problem

The membrane, which is initially horizontal and stress free, is loaded centrally as shown in the figure. If the membrane is linearly elastic with respect to Hencky strain, then the relationship between the force F and the angle α is:-

$$F = \frac{-2EA_o}{1 - \nu^2} \left[\cos(\alpha)\right]^{\frac{\nu}{1-\nu}} \sin(\alpha) \log_e\left[\cos(\alpha)\right] \qquad (6.45)$$

where A_o is the initial cross-sectional area of the membrane and E is the Young's modulus of the membrane material.

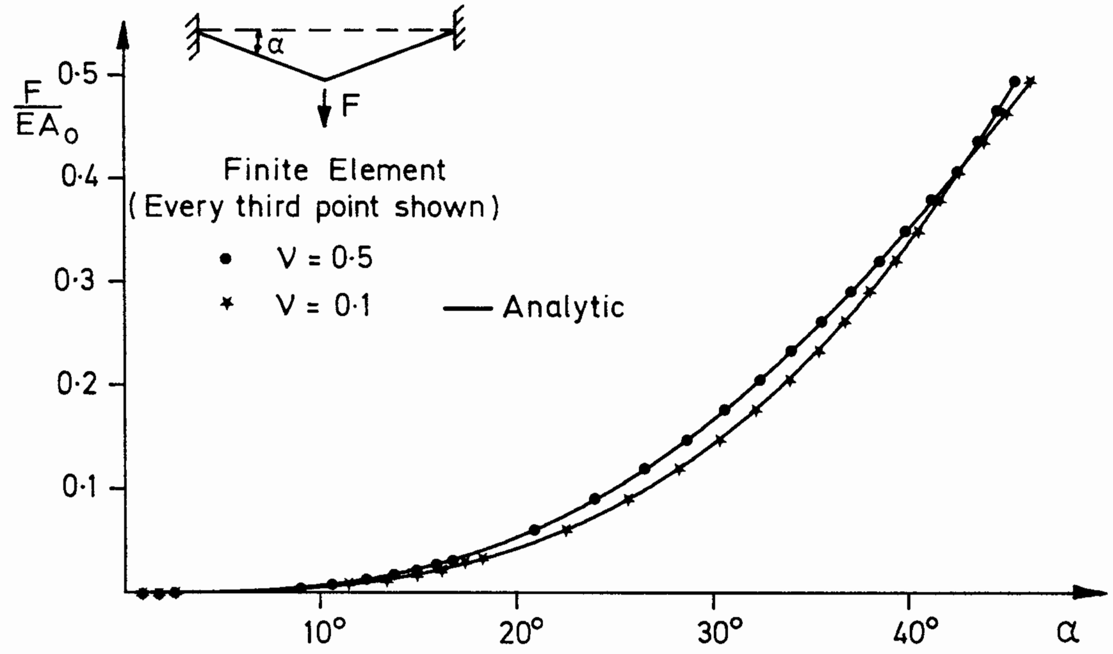

Figure 6.11: Membrane Element Test Problem

In the initial state the structure has zero lateral stiffness, thus in the finite element calculation it is necessary to apply a series of displacement increments to all the nodes in the structure at the start of the analysis. As the membrane begins to deform, the lateral stiffness increases and it is then possible to continue the analysis by applying load increments to the central node only. In the analyses presented here the size of the load increments was increased during the course of the calculation to compensate for the increased stiffness of the structure as a result of its deformation. Comparisons between finite element solutions to this problem and the relationship defined by equation (6.45) are plotted in Figure 6.11 for two separate values of Poisson's ratio.

6.7 Small Strain Elastic Thick Cylinder Analysis

A series of small strain elastic thick cylinder finite element analyses using different finite element meshes are presented in this section. The purpose of this series of calculations is to investigate the effects of mesh topology on the quality of the calculated stresses for this particular problem, and to use the results to choose an appropriate mesh layout for the large strain cavity expansion analysis described in Section 6.8. The small strain thick cylinder problem is not a severe test of this finite element formulation, but it may be used to illustrate the fact that variations in mesh topology can have an important effect on the quality of the results when the material behaviour is near incompressible.

Four meshes have been used in this study and are shown in Figure 6.12. In the finite element analyses, a radial displacement of 0.03 per cent is prescribed to the inner boundary and the calculation of the Gauss point stresses performed in a single displacement increment for Poisson's ratio values of 0.3, 0.4 and 0.48.

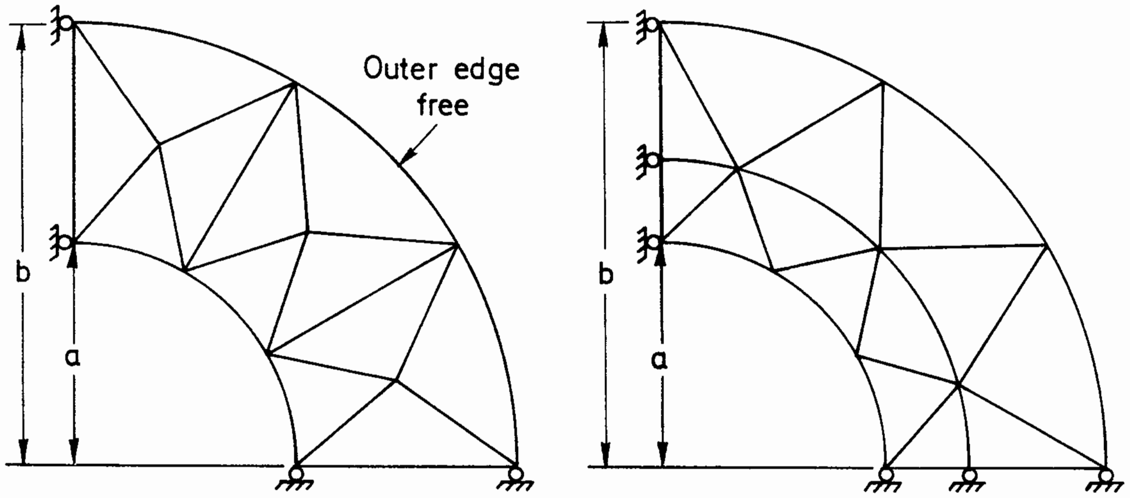

Mesh 1
12 elements (66 D.O.F.)
b=2a

Mesh 2
14 elements (78 D.O.F.)
b=2a

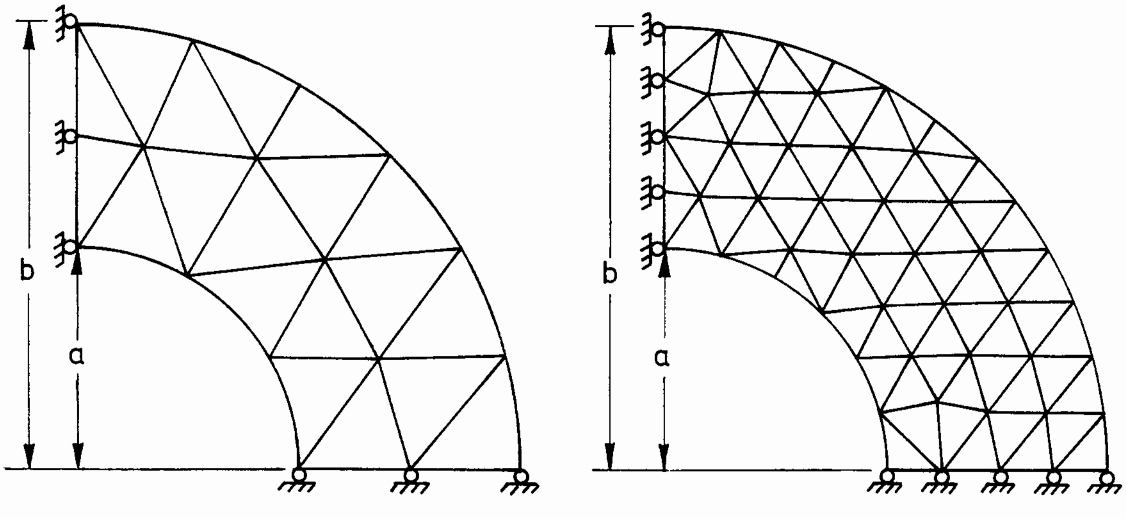

Mesh 3
19 elements (104 D.O.F.)
b=2a

Mesh 4
74 elements (348 D.O.F.)
b=2a

Figure 6.12: Meshes for Thick Cylinder Analysis

The quality of the principal stresses produced by the finite element calculations are characterized by the r.m.s. error:-

$$\text{r.m.s. error} = \frac{1}{n}\left[\frac{[\,\sigma'(r) - \sigma(r)\,]^2}{\sigma^2(r)} \right]^{1/2} \tag{6.46}$$

where $\sigma'(r)$ is a Gauss point stress from the finite element calculation, r is the radius of the Gauss point, $\sigma(r)$ is the exact value of the stress at radius r calculated from elasticity theory and the total number of Gauss points in n. The r.m.s. error for the radial stresses is plotted in Figure 6.13: the errors for the other two principal stresses have not been plotted since these show identical trends.

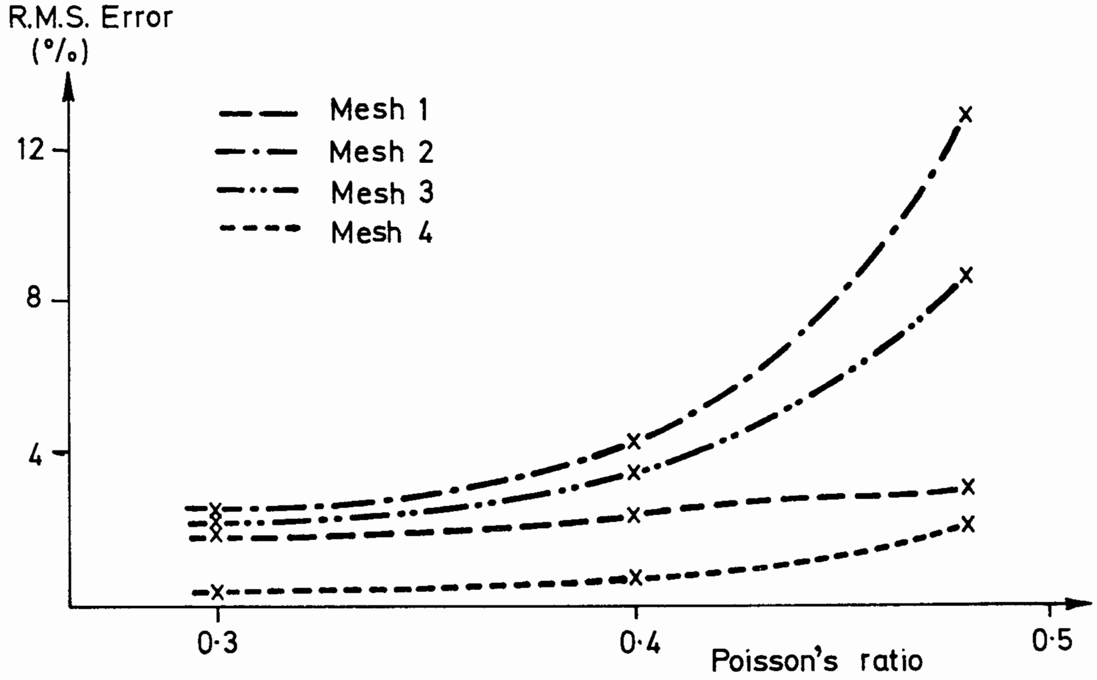

Figure 6.13: Errors in Radial Stresses

The results of this numerical experiment have several interesting features. Firstly, in all cases the r.m.s error increases as Poisson's ratio approaches 0.5. These errors arise because the incompressibility condition imposes additional constraints on the nodal velocities, thus reducing the number of 'free' degrees-of-freedom in the mesh (see Section 2.3). A further feature of the results is that Mesh 1 performs rather better than Mesh 2 and Mesh 3 in spite of the fact that it has a smaller number of degrees-of-freedom. It is also clear from Figure 6.13 that the rate of increase of r.m.s error with Poisson's ratio is smallest for Mesh 1. These trends arise because the total number of kinematic constraints imposed on the nodal velocities by the incompressibility condition are reduced by virtue of the special arrangement of elements used in the Mesh 1. This effect has been reported by Nagtegaal et al. (1974) for the case of the constant strain triangle and is discussed at greater length in Section 2.3 of this dissertation.

Sloan (1981) shows that for an infinite number of six-noded triangular elements with three-point integration, the total number of degrees-of-freedom per element is four, and the incompressibility condition imposes three constraints. The effect of increasing Poisson's ratio from a low number to approximately 0.5, therefore, is to reduce the number of free degrees-of-freedom by a factor of four. This implies that as a general rule of thumb, an approximately incompressible analysis will yield results comparable in quality to a compressible analysis only if the element density is quadrupled. This trend is indeed observed in the results presented here, Mesh 3, with nineteen elements, producing data at low Poisson's ratio that compares with the high Poisson's ratio data produced by Mesh 4, with seventy four elements.

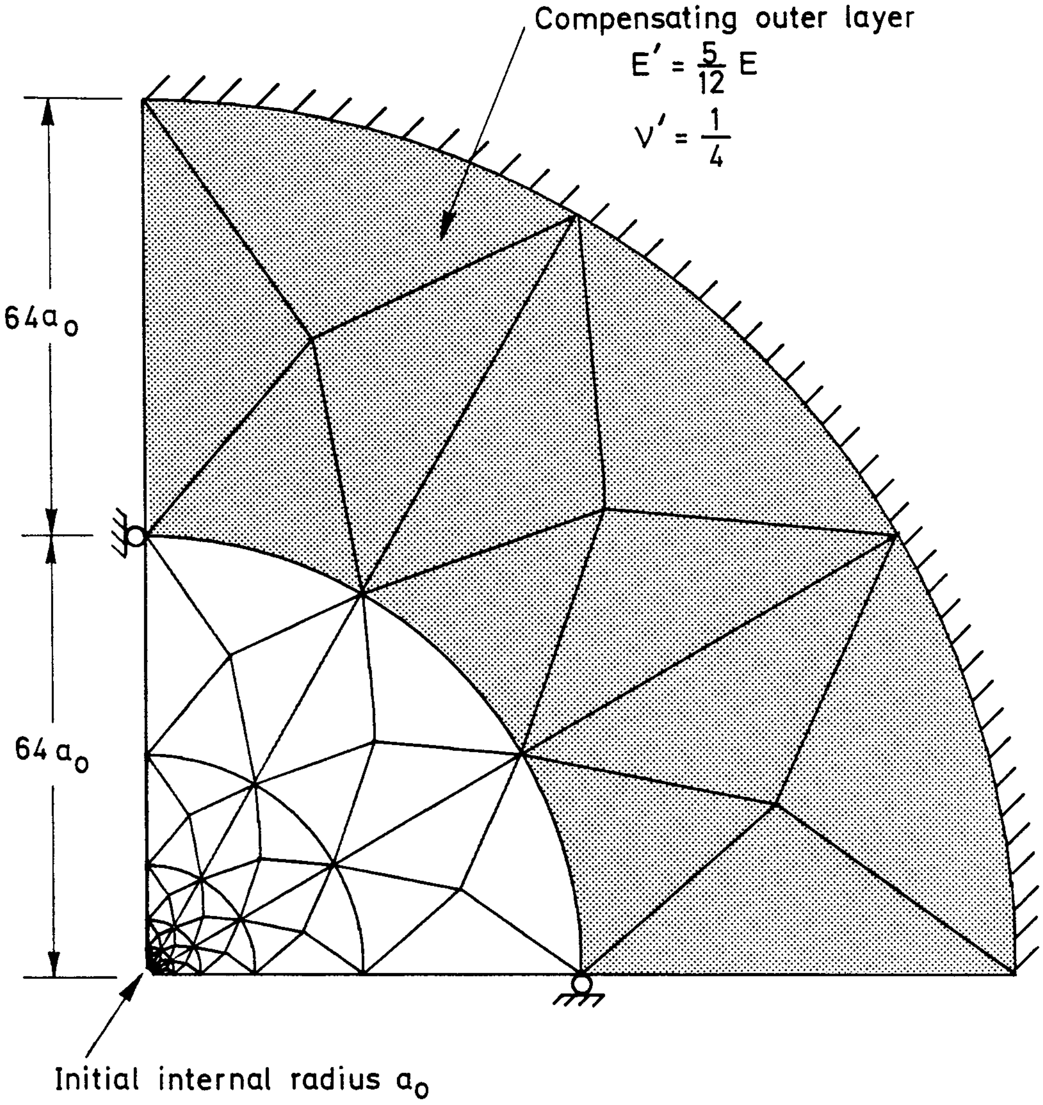

Figure 6.14: Mesh for Cavity Expansion

The analysis of plane strain cavity expansion in a von Mises material is a rare example of a large strain problem with a known closed form solution for the stresses. Since the analysis also involves non-homogeneous deformations it represents a severe test of the finite element formulation. This problem has been studied theoretically by Gibson and Anderson (1961) for an elastic-perfectly plastic Tresca material (with small strain in the elastic region) and by Sagaseta (1984) for an elastic perfectly-plastic von Mises material using large strain analysis throughout. This latter solution, which is summarized in Appendix 6A, is used here to check the solution obtained from a finite element analysis of this problem. The Sagaseta solution is for a material that is incompressible in the elastic regime, and this feature is approximated in the finite element calculations by using a Poisson's ratio of 0.49.

In order to optimise the accuracy of the finite element calculation it is desirable to avoid as far as possible the detrimental effects of the additional kinematic constraints imposed by the incompressibility condition. Since the cavity expansion problem described here is radially symmetric, the shape of the elements is preserved during the calculation, and it is possible to use special arrangements of elements to reduce the effects of the incompressibility condition (see Section 2.3). With this in mind, the mesh for the cavity expansion analysis is developed from the special arrangement of elements that was found to be successful for the small strain radial expansion problem described in Section 6.7 (see Figure 6.14).

Since the Sagaseta cavity expansion analysis is based on a continuum of infinite extent, it is necessary to add a correcting layer to the perimeter of the mesh to simulate the infinite boundary. The outer edge of this correcting layer is fixed and has material properties:-

$$\nu' = 0.25 \quad \text{and} \quad E' = \frac{5E}{12}$$

where E is the Young's modulus of the inner mesh and the outer radius of the layer is arbitrarily chosen to be twice the inner radius. Details of the calculation of the material properties of the correcting layer are given in Appendix 6B.

In the finite element solution presented here, an expansion ratio of four is applied to the radius of the cavity and the calculation performed in 400 displacement increments. The ratio (G/c) used in the analysis was 112 and six-noded triangular elements with a three-point integration rule were used to represent the continuum.

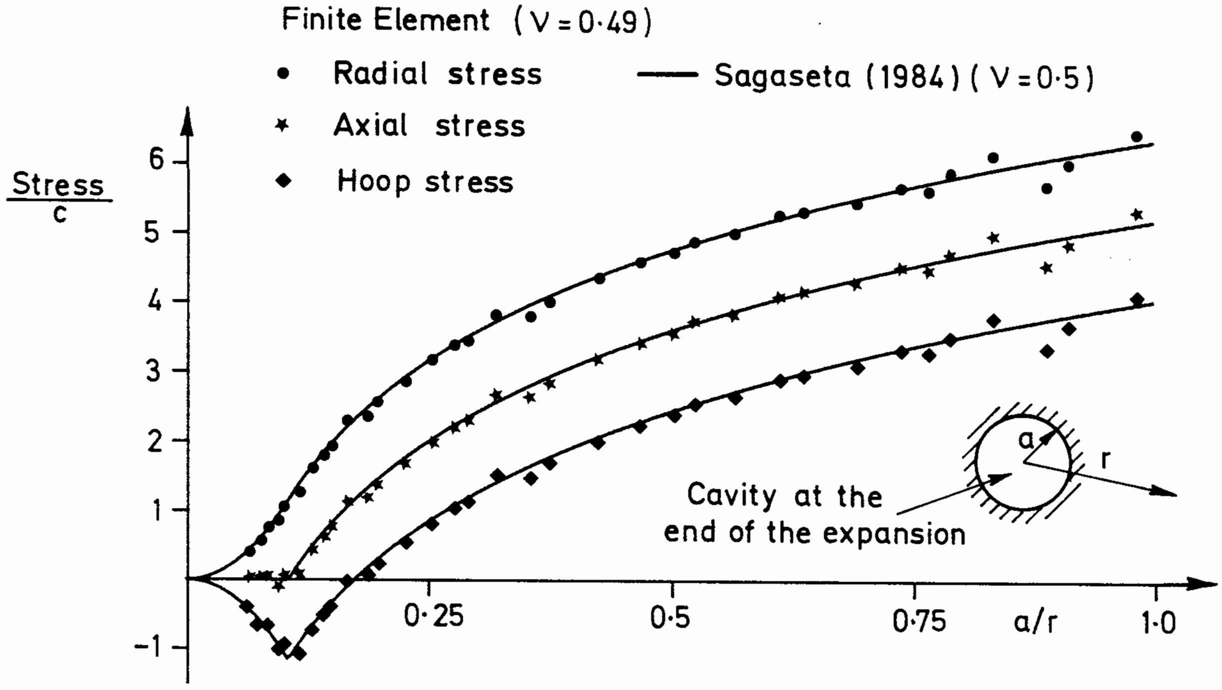

Figure 6.15: Results of Cavity Expansion

The results of the calculation are plotted in Figure 6.15 and the agreement with the Sagaseta solution is surprisingly good given that a Poisson's ratio of 0.49 rather than 0.5 was used, and that the element sides are curved which means that the three-point Gauss rule is insufficient to calculate the element stiffness matrices exactly. Some scatter of the results is apparent near the inner boundary (a/r = 1). This is due to the fact that since the nodes on the inner boundary have prescribed displacements this area of the mesh is heavily constrained. It is likely that this scatter would be reduced if the calculation were repeated using force rather than displacement control on this boundary.

A repeat of this finite element calculation in which an arbitrary arrangement of triangles was used for the mesh resulted in a large scatter in the results. The scatter could be considerably reduced by using a 'selective' integration element based on the formulation developed by Nagtegaal and de Jong (1981) in which three Gauss points are used to integrate the deviatoric stress components and a single Gauss point used for the mean stress. The use of a formulation that relies on this type of integration scheme is not desirable for general large strain analysis, however, since it may be necessary to 'over-integrate' those elements that become heavily distorted during the analysis in order to preserve the accuracy of the element stiffness matrices (see Section 2.2.4).

6.9 Small Strain Collapse Problems

Finite element solutions to collapse problems have a well known tendency to overestimate limit loads or in severe cases to show no limit load at all, even though one is known to exist (Toh and Sloan (1980), Sloan (1981)). This difficulty is associated with the finite discretization involved in the analysis, and is exacerbated by incompressible material behaviour. Since the analysis of an unpaved road is a large strain collapse problem, it is necessary to check that the proposed formulation is capable of predicting collapse loads for cases where displacements are small before progressing to the large displacement cases.

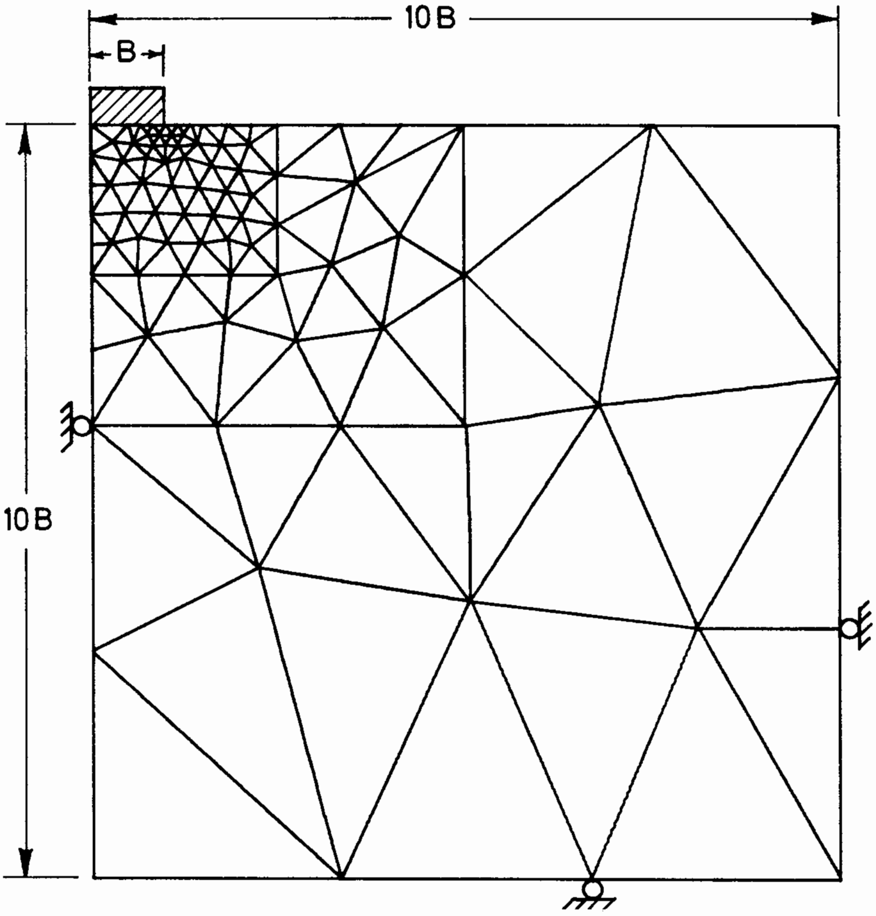

Figure 6.16: Mesh for Collapse Load Calculations

In all the calculations presented in this section, the mesh shown in Figure 6.16 has been used. The analyses are displacement controlled, in which the nodes at the base of the footing are constrained laterally for the rough footing cases, and for the smooth footing cases these lateral restraints are removed. The footing pressure is obtained simply by dividing the sum of the vertical forces on the footing nodes by the footing width.

A good review of the previous work in the area of collapse load calculations is given by Griffiths (1982).

6.9.1 von Mises Material

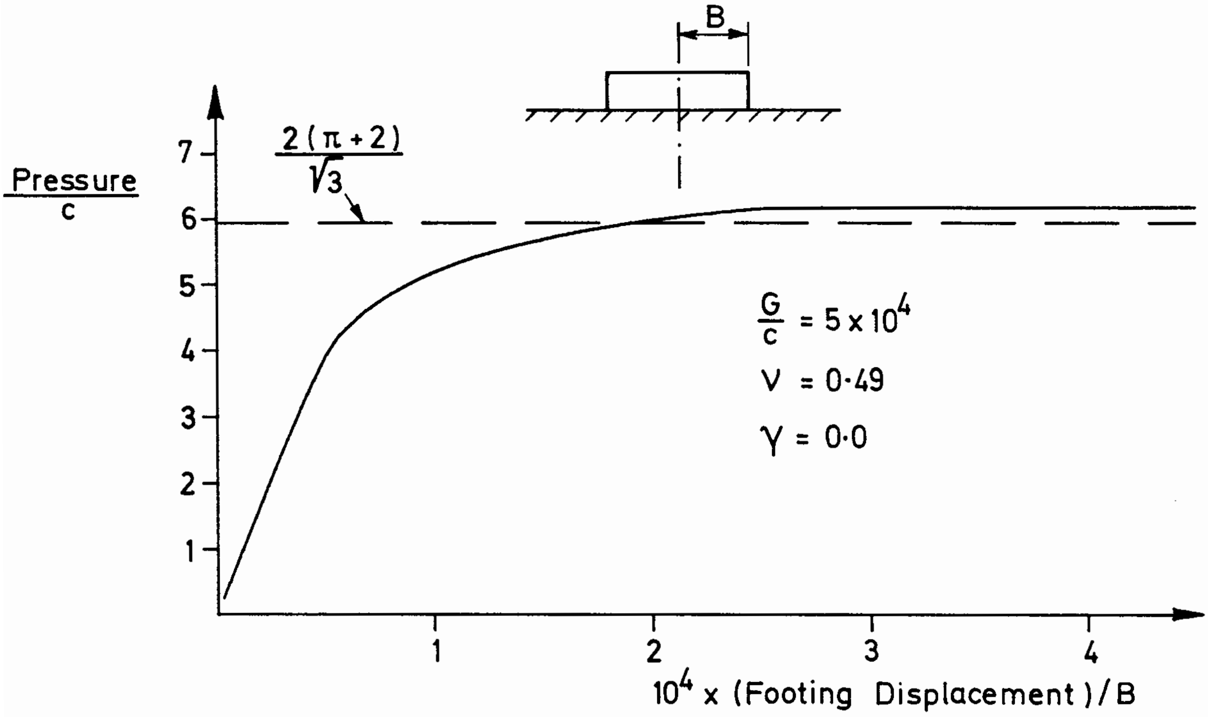

Figure 6.17: Collapse Calculation for a von Mises material

A collapse load calculation for a smooth footing resting on weightless von Mises soil has been performed, and the resulting load/displacement curve is plotted in Figure 6.17. A large value of G/c was adopted in order to ensure that the calculation approximated the infinitesimal displacement case. The analysis was performed in 150 vertical displacement increments to the footing base. A well defined collapse load was obtained which slightly exceeded the theoretical value of $2c(\pi + 2)/\sqrt{3}$. (Note that the $2/\sqrt{3}$ factor appears in this expression to account for the difference between plane strain and triaxial compression shear strength as discussed in Section 3.5.1). This error is partly due to the discretization inherent in the finite element method, and partly due to the effects of the kinematic constraints on the nodal velocities.

6.9.2 Matsuoka Material

Collapse load calculations involving smooth and rough footings on frictional soil either with self-weight or surcharge have been performed. The Matsuoka plasticity formulation described in Section 3.5.2 was used to represent the soil, and a triaxial compression friction angle of 26.46° was used in conjunction with a 'degree of association' of 0.6*. These calculations correspond to a plane strain friction angle of 30° (see Table 3.1). A Poisson's ratio of 0.35 was used, and the value of K_o was taken to be unity in the calculation of the initial stresses.

An exact solution to N_q exists for both smooth and rough footings (Prandtl (1921)) which may be used to check the results of the finite element calculation for the weightless soil with surcharge:-

$$N_q = \tan^2\left[\frac{\pi}{2} + \frac{\phi_{ps}}{2} \right]\exp\left[\pi \tan(\phi_{ps})\right] \qquad (6.48)$$

For the case of a footing resting on a soil with self-weight, no exact collapse load solutions exist. Hansen and Christensen (1969) have

---

* The choice of dilation angle in this type of calculation is somewhat arbitrary in this case since it has negligible effect on the value of the computed collapse load.

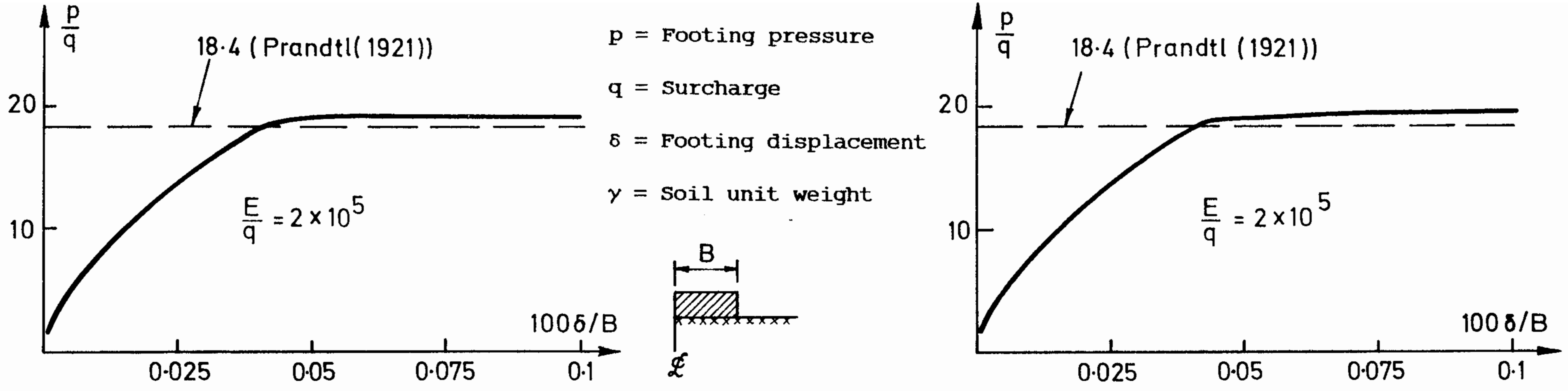

Smooth Footing with Surcharge

Rough Footing with Surcharge

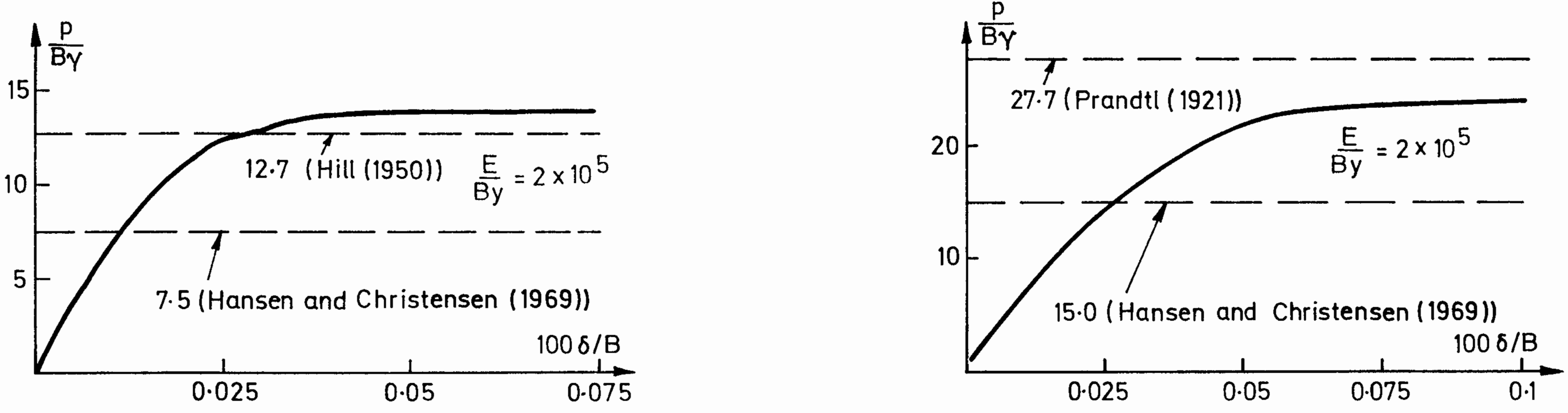

Smooth Footing with Self-Weight

Rough Footing with Self-Weight

Figure 6.18: Collapse Calculations for a Matsuoka Material

obtained approximate solutions using a slip line technique and Prandtl (1921) and Hill (1950) have proposed mechanisms that may be used to obtain approximate collapse loads for rough and smooth footings respectively.

The load/displacement curves obtained from the finite element analyses are plotted in Figure 6.18 and the collapse load solutions described above are superimposed on the appropriate plots. For the weightless case, the finite element collapse load exceeds the exact value by an acceptably small amount. For the soil with self-weight, the finite element solutions compare well with the approximate solutions.

An interesting feature of calculations of this sort is that as the dilation angle is reduced, then the finite element analysis tends to take longer, and becomes more unstable. This increase in solution time is due to the use of a larger number of sub-increments in the 'stress update' calculation which is necessary to preserve the accuracy of the equilibrium check. These instabilities seem to be dependent on the difference between the friction angle and the angle of dilation, and have also been observed by Griffiths (1982) who was unable to obtain stable collapse loads using a zero dilation angle when the plane strain friction angle exceeded 35°.

APPENDIX 6A

Closed Form Solution for Cavity Expansion

(After Sagaseta (1984))

In the elastic region:-

$$\sigma_r = I_r \, c \, \Lambda(\eta) \tag{6A.1}$$

$$\sigma_z = I_r \, c \left[\Lambda(\eta) + \log_e(1 - \eta^2) \right] \tag{6A.2}$$

$$\sigma_\theta = I_r \, c \left[\Lambda(\eta) + 2 \log_e(1 - \eta^2) \right] \tag{6A.3}$$

where:-

$$I_r = \frac{G}{c} \tag{6A.4}$$

$$\eta^2 = \frac{a^2 - a_o^2}{r^2} \tag{6A.5}$$

$$\Lambda(\eta) = \eta^2 + \frac{\eta^4}{4} + \frac{\eta^6}{9} + \frac{\eta^8}{16} + \; . \; . \; . \tag{6A.6}$$

a_o is the initial radius of the cavity

a is the final radius of the cavity

r is radius corresponding to the stresses σ_r, σ_z and σ_θ

c is the triaxial compression shear strength

The position of the elasto-plastic boundary is given by:-

$$\eta_r^2 = 1 - \exp\left[\frac{-2}{\sqrt{3}\, I_r} \right] \tag{6A.7}$$

The stresses in the plastic zone are:-

$$\sigma_r = p + \frac{2c}{\sqrt{3}} \tag{6A.8}$$

$$\sigma_\theta = p - \frac{2c}{\sqrt{3}} \tag{6A.9}$$

$$\sigma_z = p \tag{6A.10}$$

where p, the mean pressure, is given by:-

$$p = I_r c\left[\Lambda(\eta) + \log_e(1 - \eta_r^2)\right] + \frac{4}{\sqrt{3}} c \log_e(\eta/\eta_r) \tag{6A.11}$$

APPENDIX 6B

Correcting Layer for the Cavity Expansion Problem

Consider a cavity of radius R in a continuum of infinite extent of Young's modulus E, and Poisson's ratio ν. If an internal pressure p is applied, then for small elastic deformations under plane strain conditions, the radial displacement is:-

$$\delta_r = \frac{pR(1 + \nu)}{E} \tag{6B.1}$$

For an outer correcting layer of internal radius R and outer radius κR, whose outer edge is fixed, made from material of Young's modulus E' and Poisson's ratio ν', then the radial displacement corresponding to an internal pressure p (again assuming small elastic plane strain deformations) is:-

$$\delta_r = \frac{pR(1 - 2\nu')(1 + \nu')(\kappa^2 - 1)}{E'\left[1 + \kappa^2(1 - 2\nu')\right]} \tag{6B.2}$$

For the finite layer to be of equivalent stiffness to the infinite continuum, then:-

$$\frac{1 + \nu}{E} = \frac{(\kappa^2 - 1)(1 + \nu')(1 - 2\nu')}{E'\left[1 + \kappa^2(1 - 2\nu')\right]} \tag{6B.3}$$

This equation clearly does not give a unique set of values of E' and ν'. For reasons of computational accuracy it is desirable to choose a low value of Poisson's ratio, thus suitable material properties for the correcting layer are:

$$\kappa = 2 \qquad E' = \frac{5E}{12} \qquad \nu' = 0.25 \tag{6B.4}$$

CHAPTER 7 ANALYSIS OF A REINFORCED ROAD

7.1 Introduction

The application of this finite element formulation to the back-analysis of a series of tests performed on physical models of the reinforced unpaved road is described in this chapter. The primary purpose of these calculations is to check the general validity of the mathematical model by seeking to use it to reproduce the trends observed in the experimental results. It is important to compare theoretical predictions with experimental results in this way in order to assess the general accuracy of the numerical calculations.

A series of model tests performed by Love (1984) has been chosen as a basis for this study. These tests were all performed under carefully controlled conditions and involved plane strain, monotonic loading only. The author had considerable opportunity to observe this experimental work at first hand and is therefore familiar with the materials and methods used, and is satisfied as to the quality of the results.

A plastic grid reinforcement was used in these experiments, and this would be expected to provide good interlock with the surrounding soil. Since the assumption is made in the finite element model that zero slip occurs at the soil/reinforcement interface, the formulation is well suited to the back-analysis of the results of these particular experiments. The general approach adopted in these calculations is to use the soil properties measured in independent tests to furnish the parameters for the finite element model. In cases where appropriate data were not available, it was necessary to resort to a 'trial and error' process to obtain the required parameters.

7.2 Model Tests Performed by Love (1984)

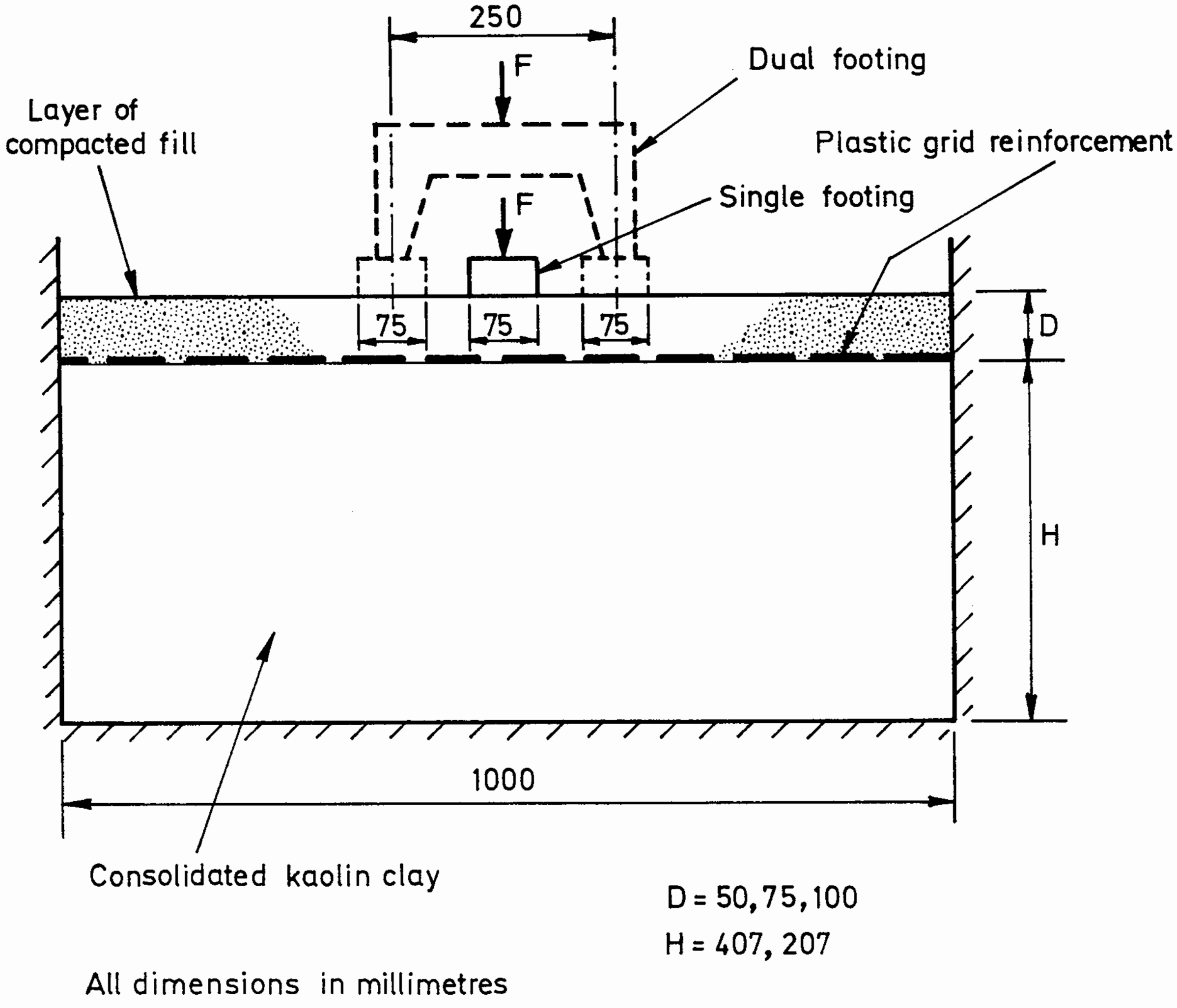

Figure 7.1: Model Test Rig (after Love(1984))

All of the tests were performed at a nominal one-quarter scale using the arrangement illustrated diagrammatically in Figure 7.1. The linear dimensions were scaled down by a factor of four from the prototype, and the shear strength and modulus of the clay scaled down by the same factor in accordance with the modelling laws. The reinforcement used in the model tests was a scaled down version of a proprietary geogrid in which the linear dimensions of the grid were reduced by a factor of four, and the stiffness (force per unit width) reduced by a factor of sixteen. A model granular fill was used in which the grading curve was a scaled down version of the full sized material.

The clay subgrade was prepared by consolidating a kaolin slurry in the test rig itself. Three different nominal clay strengths were used in the tests, and these were obtained by using the appropriate consolidation pressures. The consolidation process was arranged so that after the clay had been allowed to swell and had then been trimmed by a small amount, the final height of the block was 407 mm.

Two sets of experiments were performed on each clay sample. The trimmed clay block obtained at the end of the consolidation process was used for the first set, and a second series of tests was performed in which the clay disturbed by the first set of experiments had been removed, and the block trimmed to a height of 207mm. The results of these two sets of experiments demonstrated that the effects of variations in the height of the clay block were relatively insignificant, and that equal importance could be attached to both sets of results.

In addition to the clay blocks prepared for model testing, one sample at each of the three nominal strengths was prepared with the sole object of investigating the variations of strength and moisture content with depth. The shear strengths were measured using a shear vane and the results obtained by Love are reproduced in Figure 7.2. Since the clay blocks were clearly non-homogeneous, the shear vane measurement made at the arbitrary depth of 55 mm below the trimmed surface was used to characterize the subgrade strength in the model tests.

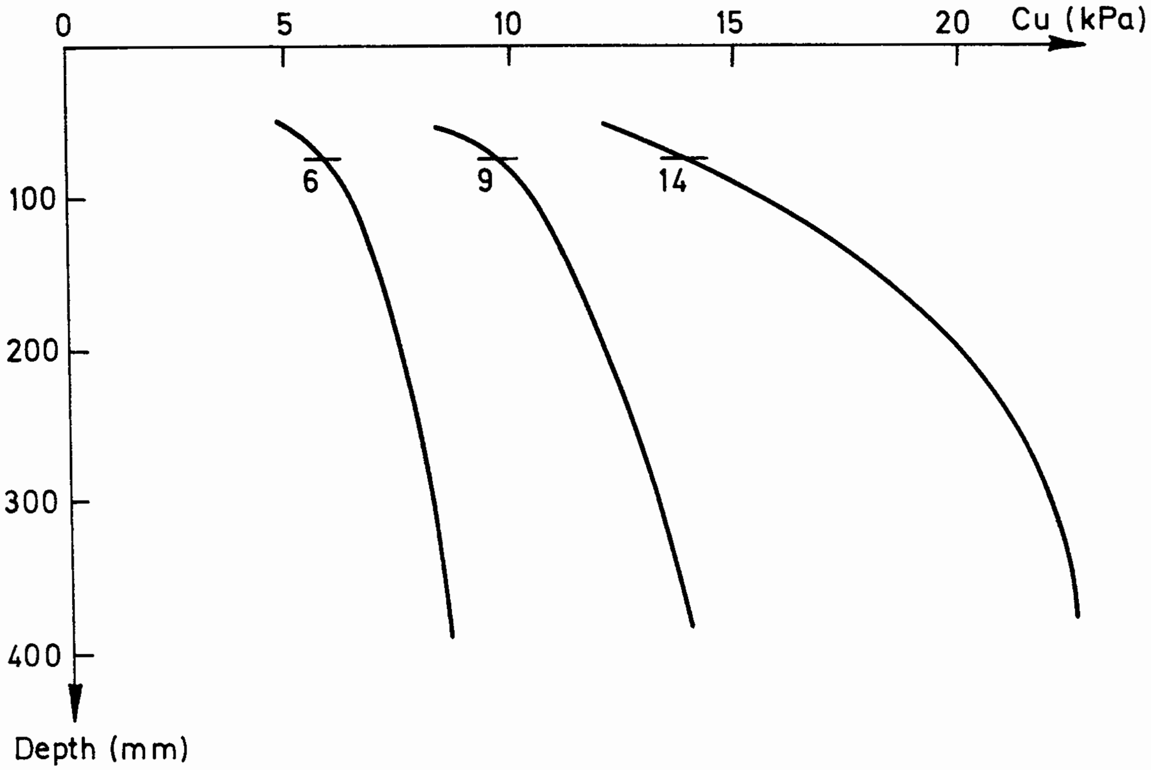

Figure 7.2: Shear Strength Variation in Model Subgrade (after Love(1984)

In the main series of experiments described by Love, a single footing was jacked monotonically a distance of 50 mm into the model road for both the reinforced and unreinforced cases. During these tests, the load/deformation response of the footing was measured, and the subgrade displacements were monitored using a photographic technique. Nine combinations of fill thickness and subgrade strength were studied in this series of experiments, and these are listed in Appendix 7A. In addition to these single footing tests, one pair of experiments was performed by Love in which a dual footing was jacked into the model road. The conditions used in these tests are also listed in Appendix 7A.

Love also performed a series of experiments in which a single footing was jacked directly into the subgrade. The purpose of these subgrade-only tests was to compare the bearing capacity with the value calculated from the shear vane measurements. A selection of these tests has also been chosen for back-analysis (see Appendix 7A) in order to obtain a correlation between the shear vane measurement, and the shear strength of the equivalent homogeneous clay block for use in the finite element back-analysis calculations.

7.3 Choice of Material Properties

The following parameters are required for the finite element model:-

Clay	Two elastic parameters
	Triaxial compression shear strength
	Unit weight
Reinforcement	Modulus
	Poisson's ratio
Fill	Two elastic parameters
	Triaxial compression friction angle
	Degree of association
	Unit weight

The methods by which these parameters were obtained are described below.

7.3.1 Clay Parameters

The rate of loading used in the model tests was sufficiently high for the response of the clay to be predominantly undrained. A clay Poisson's ratio of 0.49 was therefore used to approximate the incompressibility condition imposed by this type of behaviour.

A clay density of 19 kN/m^3, being the value measured during the model tests, is used in all of the computations.

The remaining clay parameters, however, are not so easy to determine since the soil properties are not constant with depth (see Figure 7.2) whereas the material modelled by the finite element calculation is homogeneous. This difficulty was resolved by performing a series of back-analyses of the subgrade-only model tests and using the results to develop a correlation between the shear vane measurement and the strength and stiffness of the equivalent homogeneous block.

In all of the finite element back-analyses of the subgrade-only model tests, Mesh B was adopted (see Figure 7.3) to represent the clay block. This particular mesh had been prepared for the reinforced unpaved road calculation, and therefore consists of separate layers of elements to model the clay and the fill. In these subgrade-only back analysis calculations however, the clay parameters were assigned to the elements in both layers of the mesh, and the reinforcement stiffness was set to zero. This means that the finite element solution is for a clay block of total depth 450 mm, whereas in the model tests the depth was either 407 mm or 207 mm. Since the experimental results indicated that variations in the depth of the clay block had little effect on the load/deformation response of a footing on the surface, it is argued that the use of Mesh B in this way is justified.

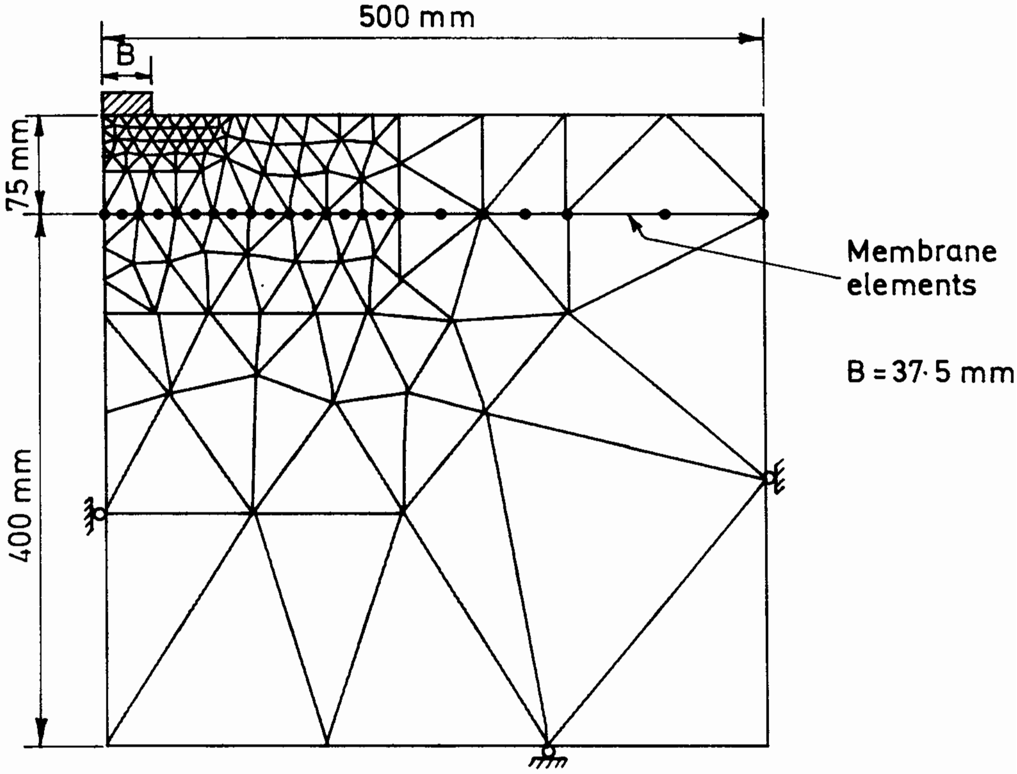

Figure 7.3: Mesh B

The four subgrade-only tests performed by Love that have been selected for back-analysis are listed in Appendix 7A. These particular cases have been chosen because they involve each of the three nominal clay strengths used in the model tests.

In order to develop a correlation between the vane shear strength measured at a depth of 55mm below the fill surface, s_{sv}, and the plane strain shear strength of the equivalent homogeneous block, c_{ps}, the following relationship is adopted:-

$$c_{ps} = K_c \, s_{sv} \tag{7.1}$$

The optimum value of K_c was found on a 'trial and error' basis by comparing finite element predictions with model test results. Once K_c had been established in this way, it was treated as a constant for all of the clay blocks used in the model test programme.

The variation of overconsolidation ratio (OCR) throughout the sample is likely to be similar for each clay block. Since the ratio (G/c_{ps}) is generally considered to be a function only of OCR (Zytynski et al. (1978)), then a rational value of shear modulus for use in the finite element computations, G, is given by:-

$$\frac{G}{c_{ps}} = I_r \qquad (7.2)$$

where I_r is again varied to obtain the best comparison between the finite element and model tests results, and subsequently treated as a constant.

The first few subgrade-only back-analysis calculations were performed using a three-point integration rule for each element in the mesh. It was found, however, that the elements in the region of the footing edge became too severely distorted (as indicated by the parameter ψ defined in equation (2.39)) for the three-point rule to be used with confidence to calculate the element stiffness matrices (see Section 2.2.4). These distortions became so severe that at large displacements some of the elements began to invert. In order to reduce the errors in the computation of the element stiffness matrices, a thirteen-point Gauss rule was used in all subsequent calculations for the elements in the region of the footing (see Figure 7.4). As well as increasing the accuracy of the stiffness matrix calculation, the use of a higher order integration rule for these selected elements had the effect of improving the general stability of the mesh.

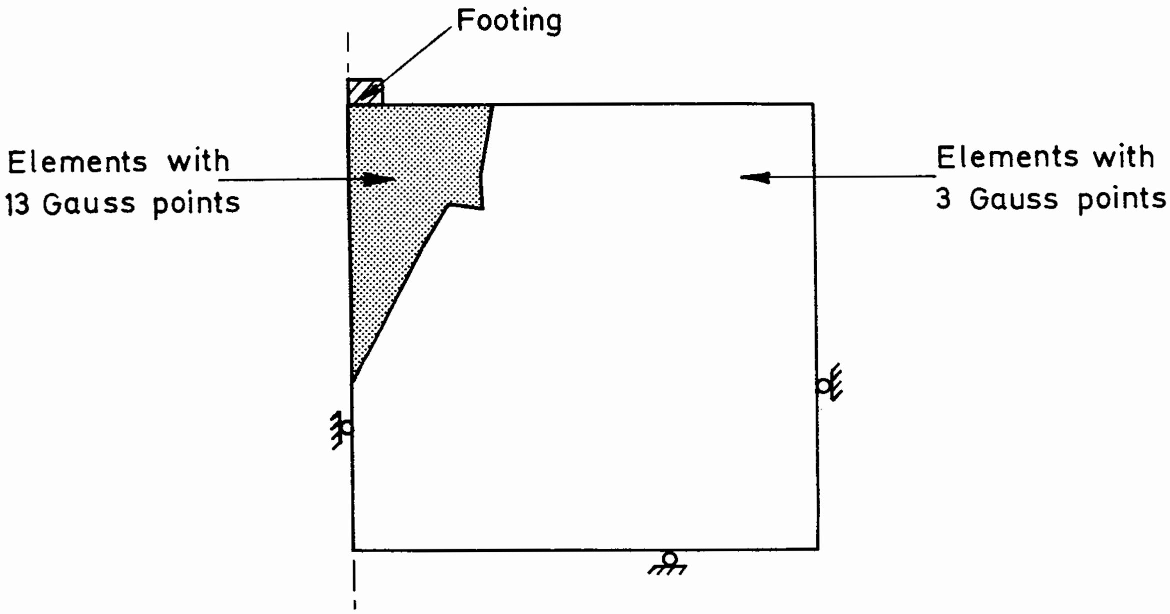

Figure 7.4: Element Gauss Points for Subgrade-Only Calculations

The values of the constants K_c and I_r that were found to give the best correlation between the experimental and numerical results are:-

$$K_c = 0.9 \qquad I_r = 31 \tag{7.3}$$

This rather low value of I_r is a direct result of the large strains occurring in the model tests. A comparison between the load/deformation curves obtained from the finite element model in which the above values of K_c and I_r are used, and the corresponding model test results is given in Figure 7.5.

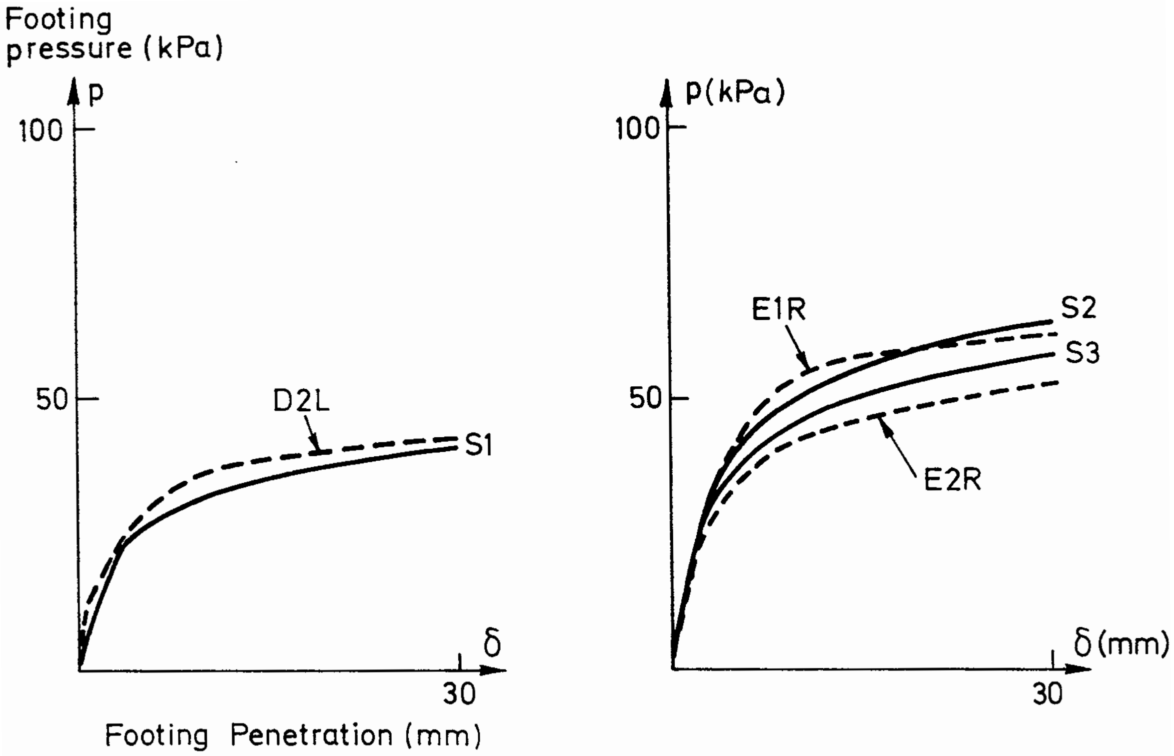

6 kPa Nominal Clay Strength

9 kPa Nominal Clay Strength

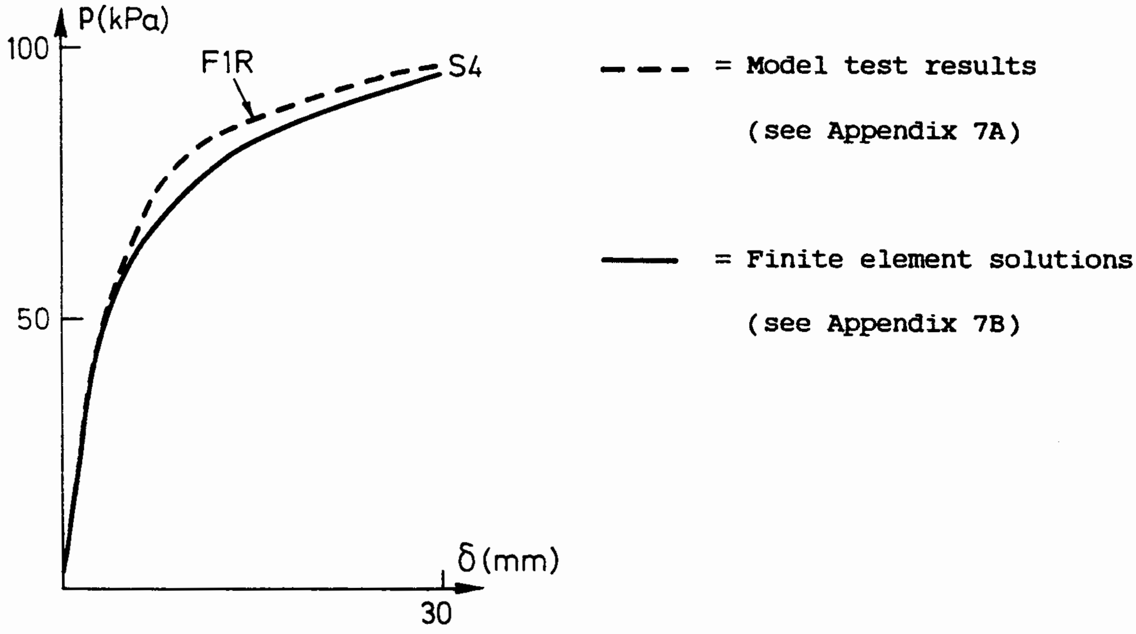

14 kPa Nominal Clay Strength

Figure 7.5: Subgrade-Only Model Test Results and Finite Element Predictions

As an example of the nature of the deformations that occurred in these calculations, part of the deformed mesh obtained at the end of calculation reference S3 is shown in Figure 7.6.

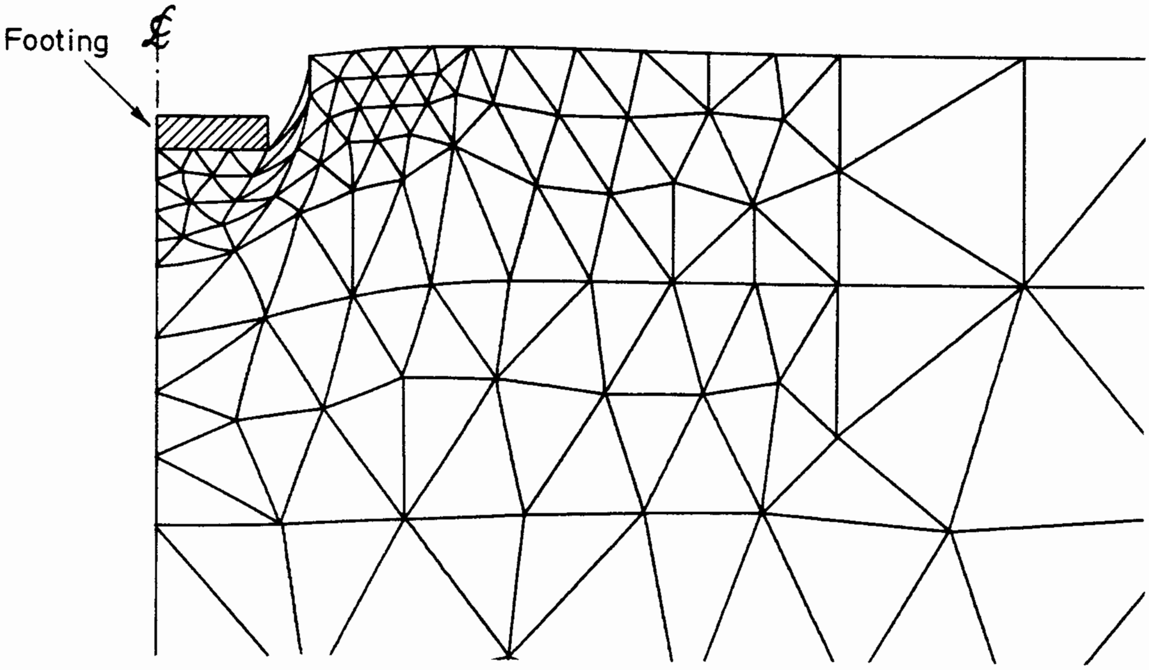

Figure 7.6: Deformed Mesh at End of Calculation S3

7.3.2 Reinforcement Parameters

A series of tests on the reinforcement was performed by Love, from which the following plane stress parameters may be obtained:-

$$Et_o = 28 \text{ kN/m} \qquad \nu = 0.5 \tag{7.4}$$

where E is the Young's modulus of the reinforcement material, and t_o is the initial thickness. This value of Poisson's ratio implies that the reinforcement material deforms at constant volume.

7.3.3 Fill Parameters

It is unfortunate that few data relating specifically to the fill properties were obtained by Love. In view of this, the parameters were selected by performing a series of back-analyses of the reinforced unpaved road model tests in which the fill properties were adjusted to give the best fit with the experimental data. The fill parameters obtained using this approach are:-

$$E = 4000 \text{ kPa} \qquad \nu = 0.35 \qquad \phi = 32^{\circ} \qquad \gamma_a = 0.6 \qquad (7.5)$$

where the triaxial compression friction angle, ϕ, and degree of association, γ_a, are defined in Section 3.5.2. These parameters correspond to plane strain friction and dilation angles of:-

$$\phi_{ps} = 36^{\circ} \qquad \psi_{ps} = 22^{\circ} \qquad (7.6)$$

The unit weight of the fill was taken to be 19 kN/m^3 in all of the finite element calculations.

7.4 Single Footing Calculations

Three separate finite element meshes, corresponding to the three fill thicknesses used in the model tests, were used to perform the reinforced unpaved road back-analysis calculations for the single footing case, and these are depicted in Figures 7.3, 7.7 and 7.8. The meshes are of the same dimensions as the test rig and are divided into two layers with the upper layer used to represent the fill and the lower layer the clay. Three-noded, three Gauss point membrane elements are placed at the interface of these two layers to model the reinforcement. The continuum elements generally have three Gauss points, except for those elements in the immediate vicinity of the footing where distortions are likely to be large and a thirteen-point integration rule is adopted.

In all of these calculations, the analysis was displacement controlled. Horizontal displacement of the nodes in contact with the footing was prevented, thus the soil/structure interface was treated as being perfectly rough. All of the calculations involved a total footing displacement of 30 mm which was about the maximum that could be applied before the mesh became too severely distorted for the results to be meaningful.

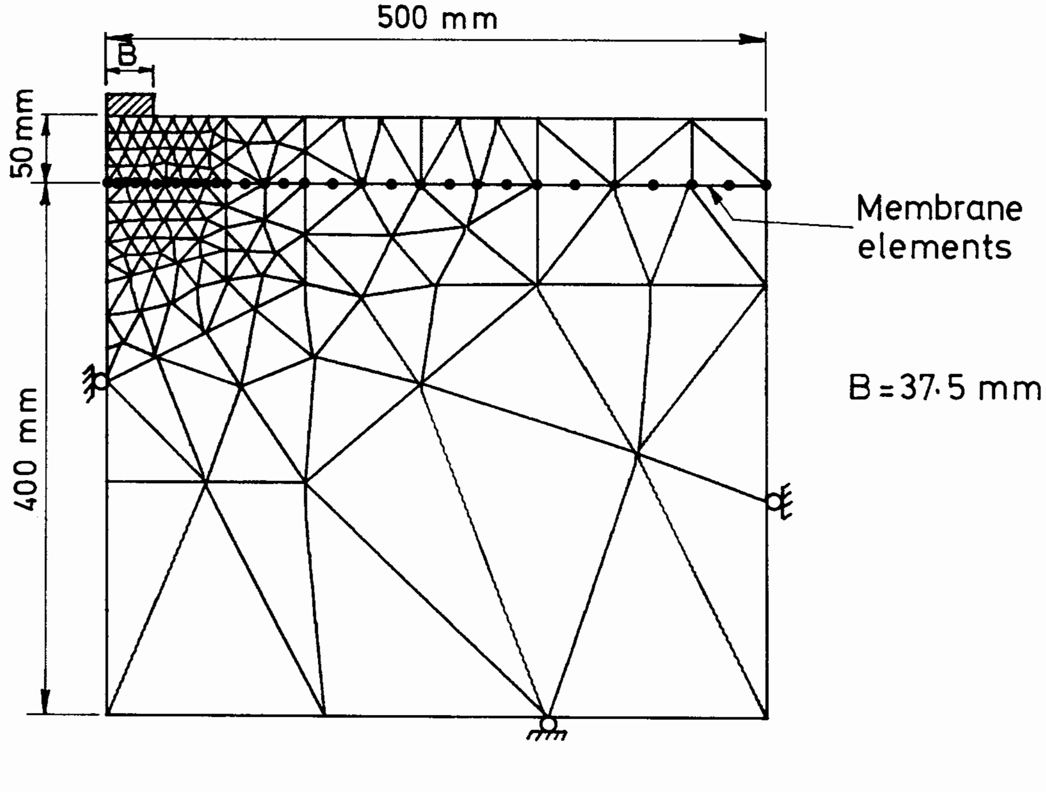

Figure 7.7: Mesh A

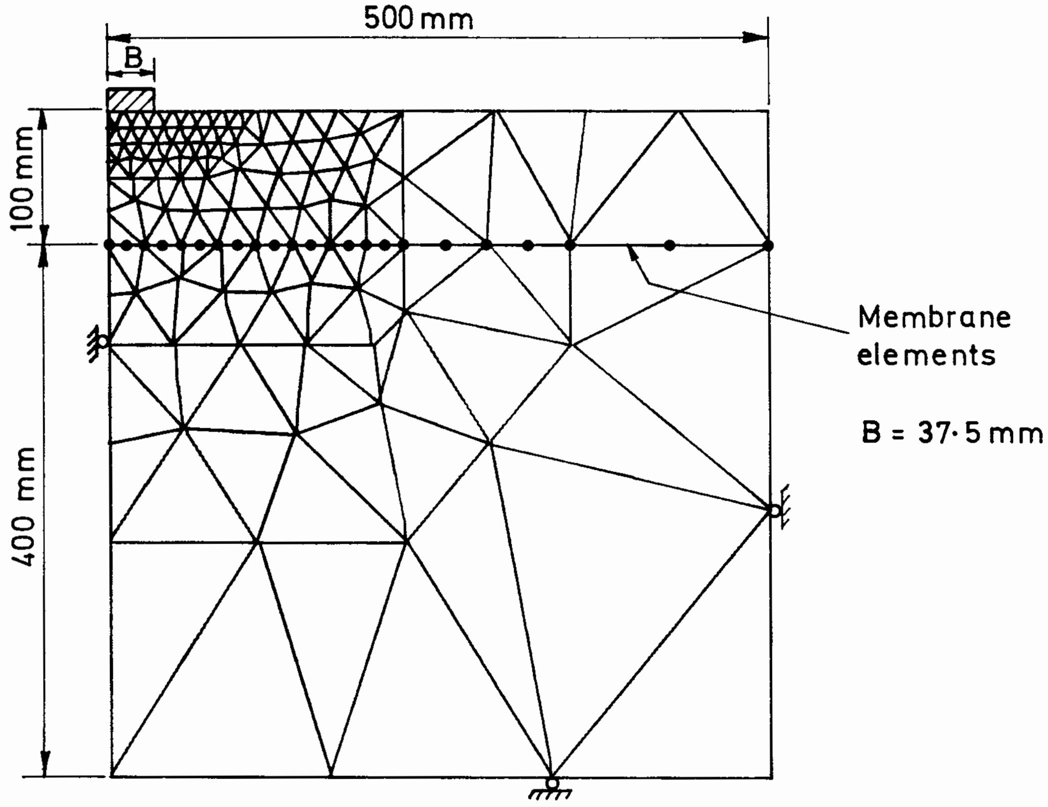

Figure 7.8: Mesh C

Love performed experiments on nine combinations of nominal clay strength and fill thickness with a single footing load, and these tests are listed in Appendix 7A. Finite element back-analyses corresponding to each of these tests were performed in which the material properties were obtained using the procedure described in Section 7.3, and are listed in Appendix 7B.

The results of these back-analysis calculations, grouped according to fill thickness, are plotted in Figures 7.9 to 7.11 in which the load/displacement curves from the model tests are compared directly with the finite element solutions. The numerical results clearly reproduce the important trend observed in the model tests that the reinforcement has an increasingly large effect on the load/deformation response as the displacements increase. A further feature of both the experimental and

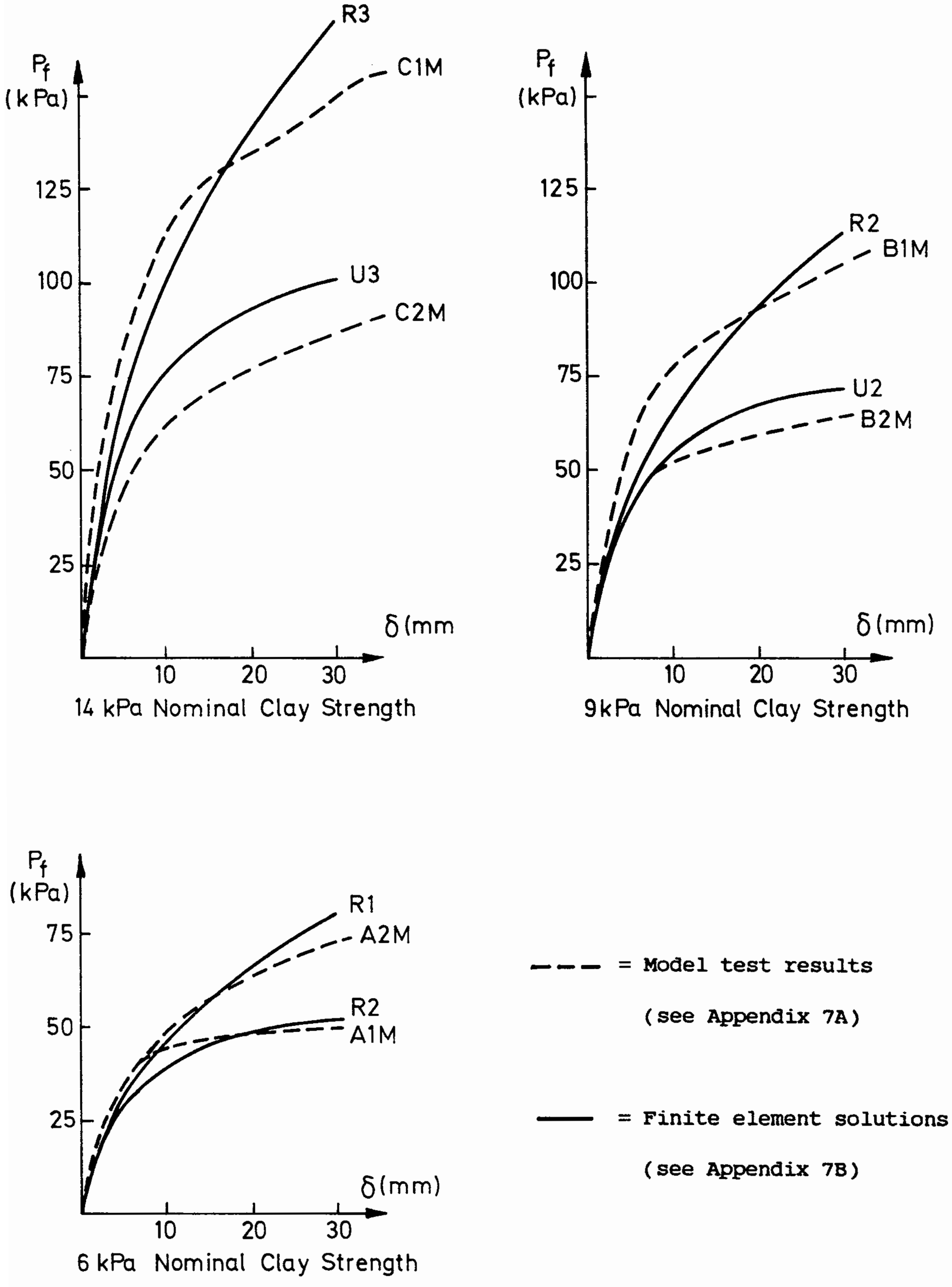

Figure 7.9: Single Footing Model Test Results and Finite Element Predictions, 50 mm Fill Thickness

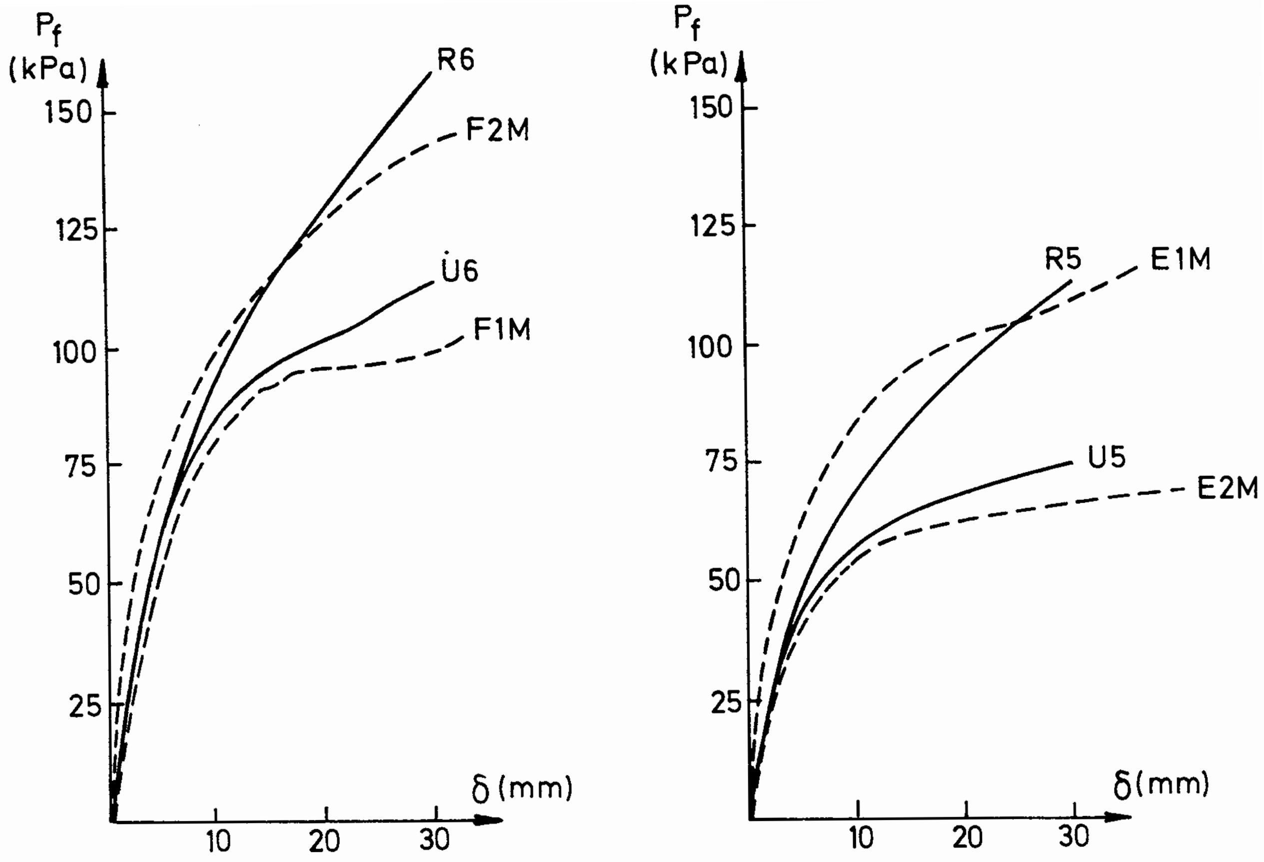

14 kPa Nominal Clay Strength

9 kPa Nominal Clay Strength

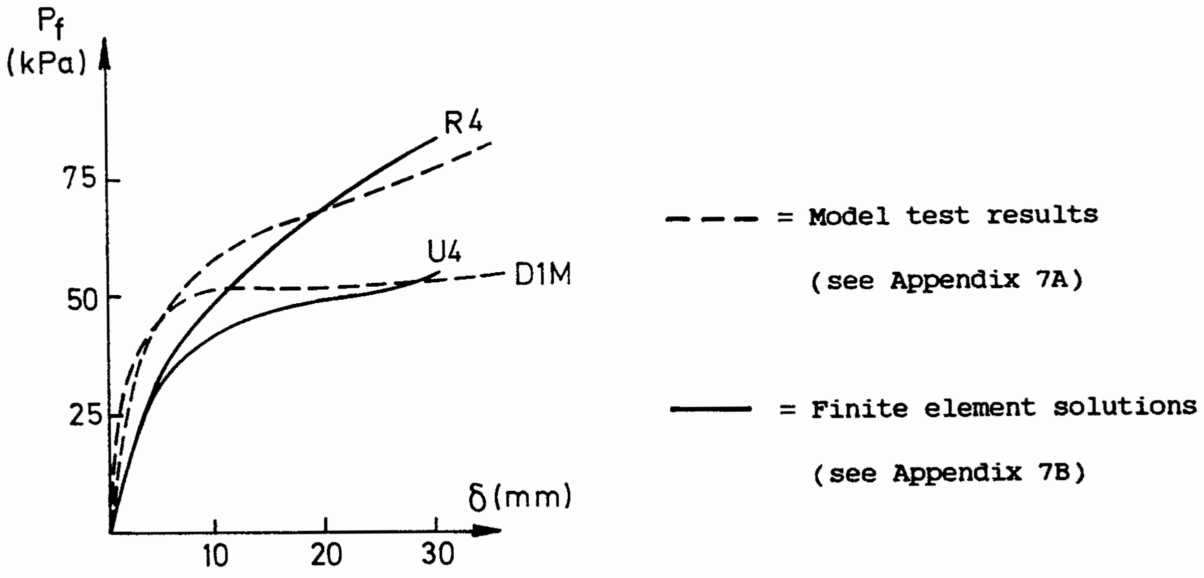

6 kPa Nominal Clay Strength

Figure 7.10: Single Footing Model Test Results and Finite Element Predictions, 75 mm Fill Thickness

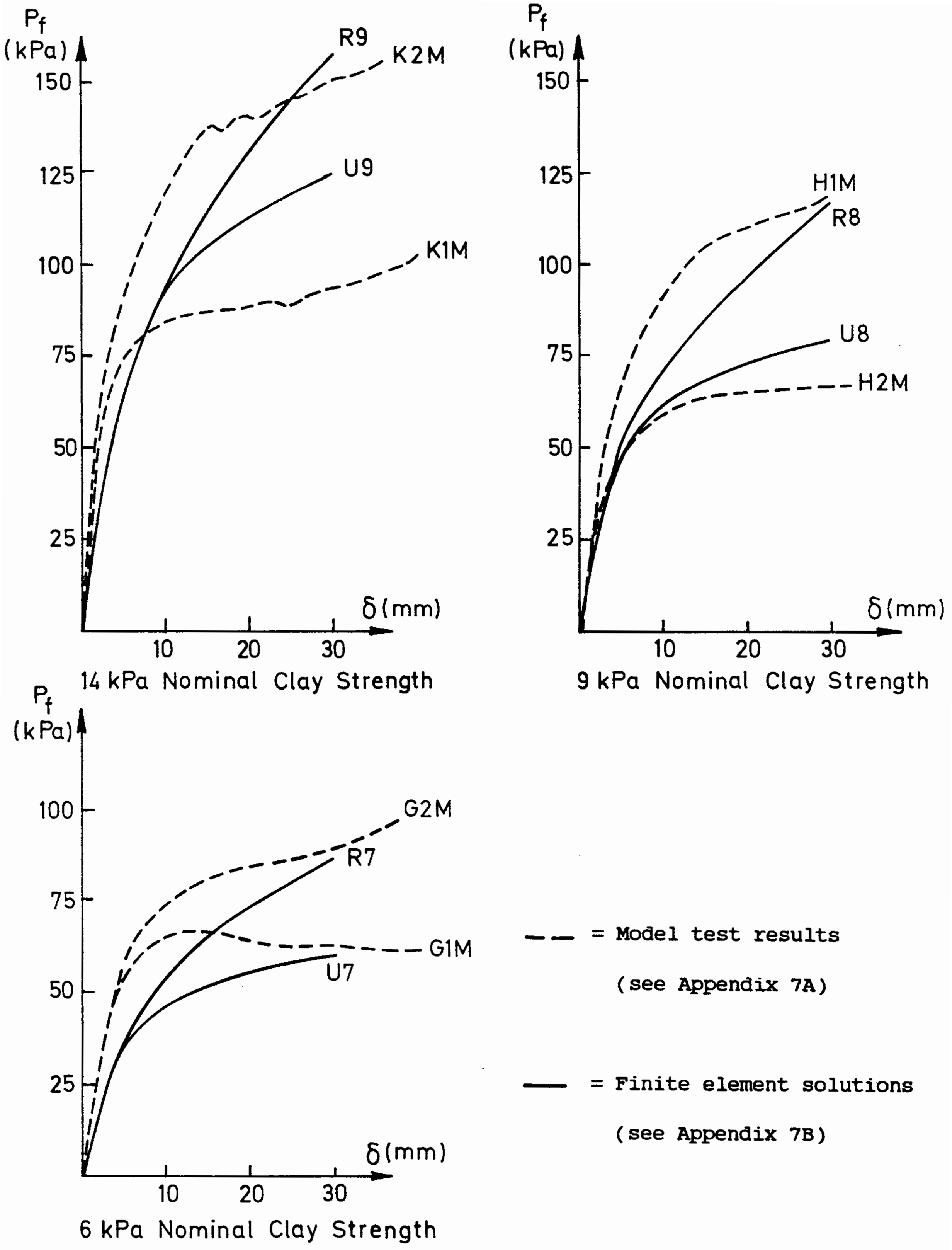

14 kPa Nominal Clay Strength

9 kPa Nominal Clay Strength

6 kPa Nominal Clay Strength

Figure 7.11: Single Footing Model Test Results and Finite Element Predictions, 100 mm Fill Thickness

numerical results is that subgrade shear strength governs the response more strongly than the fill thickness, especially in the reinforced cases. The finite element predictions of the improvement in bearing capacity caused by the reinforcement are generally realistic for the smaller fill depths at large displacements. As the fill depth increases, the correlation between numerical and experimental results becomes less accurate which indicates that an oversimplified mathematical model has been used to represent the fill.

The numerical solutions generally underestimate the initial stiffness of the structure, but the correlation improves as the displacements increase. A possible explanation for this behaviour is that the fill material is in a dense state at the start of the test and therefore would be expected to exhibit post-peak strain softening behaviour. The initial response is therefore determined by the peak friction angle with the residual angle becoming more dominant as displacements increase. Since the Matsuoka model used in this formulation is based on a material that is elastic perfectly-plastic, these variations in friction angle are not accounted for.

A further shortcoming of the numerical formulation which may have some influence on the results is that a set of constant elastic parameters are used to describe the material behaviour, whereas it is well accepted that the use of a shear modulus that increases with mean effective stress gives a more accurate representation of the behaviour of real soil (Houlsby (1985)). To the author's knowledge, however, no theory exists that can be used to model this type of behaviour in a way that ensures that the material is conservative for the case when strains are large.

The subgrade used in the model tests had a marked variation of shear strength with depth (see Figure 7.2), whereas a homogeneous subgrade was used in the finite element model. Although a method has been devised whereby the appropriate value of subgrade shear strength for use in the finite element calculation may be obtained, this correlation is only strictly valid for the particular depth of failure zone occurring in the subgrade-only tests (see Section 7.3.1). Since the effect of the reinforcement and fill is to increase the depth of the failure mechanism, it is likely that the shear strength used in the finite element calculations gives rise to an underestimate of the overall strength of the clay that is mobilised in the model tests. This would explain the general tendency of the finite element model to underestimate the strength of the road by an amount that increases with fill thickness.

It was observed in the experimental work that the reinforcement had a tendency to 'cut into' the clay subgrade. This type of behaviour was particularly apparent for the weaker clay samples and changed the nature of the reinforcement/soil interface from the ideal conditions assumed in the finite element model. It is also possible (but unlikely) that the reinforcement used in the model tests was not sufficiently rough to provide full interlock with the surrounding soil, a factor not accounted for in the numerical solutions.

As an example of the nature of the deformation computed using the finite element model, the mesh obtained at the end of analysis R1 is reproduced in Figure 7.12.

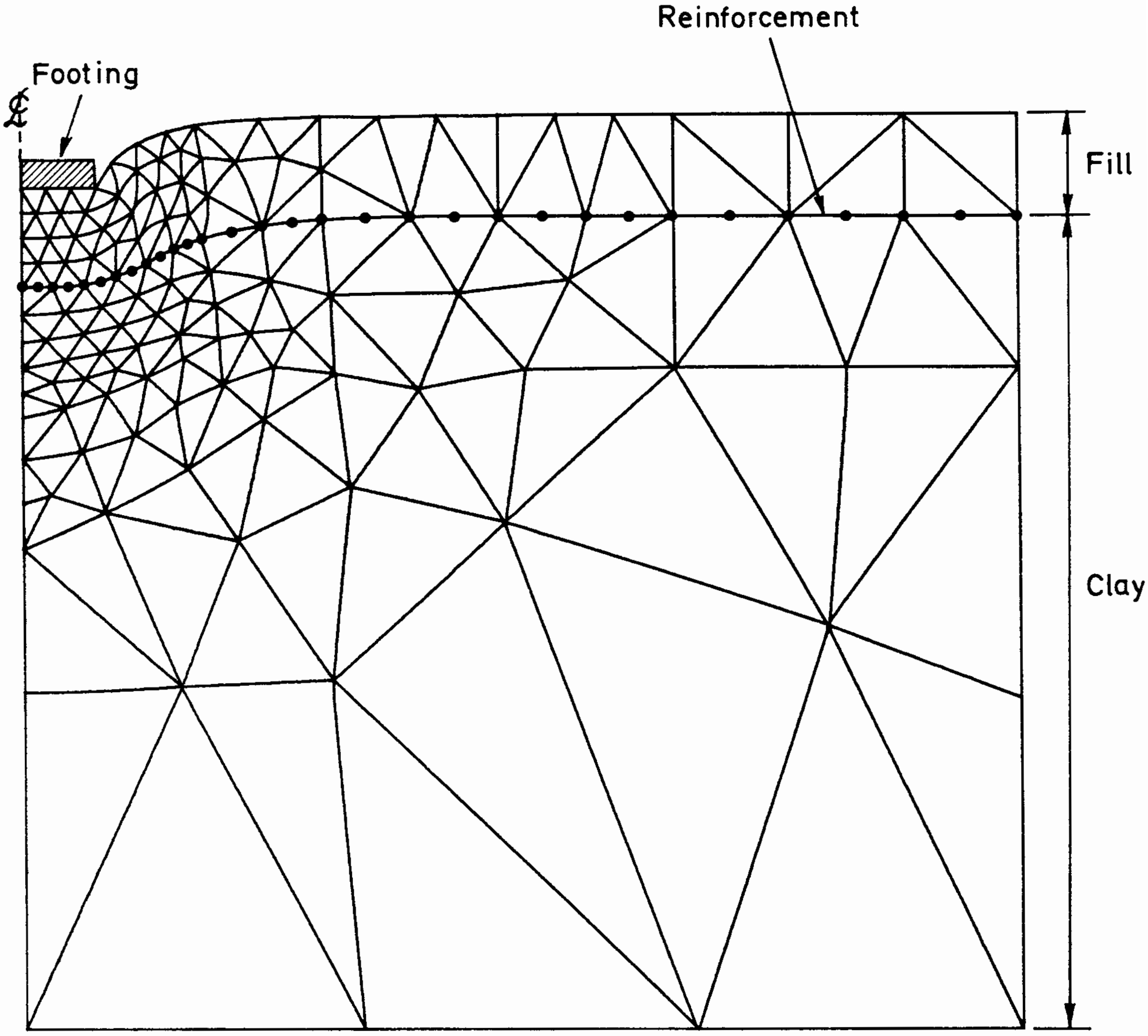

Figure 7.12: Deformed Mesh at End of Calculation R1

7.5 Dual Footing Calculations

One reinforced and one unreinforced test was performed by Love in which a dual footing was used, with all of the other features of the test rig being unchanged. The material properties used for these tests are listed in Appendix 7A. The purpose of these experiments was to investigate the effect of reinforcement on the behaviour of the model road under conditions that were more representative of traffic loading than the single footing case.

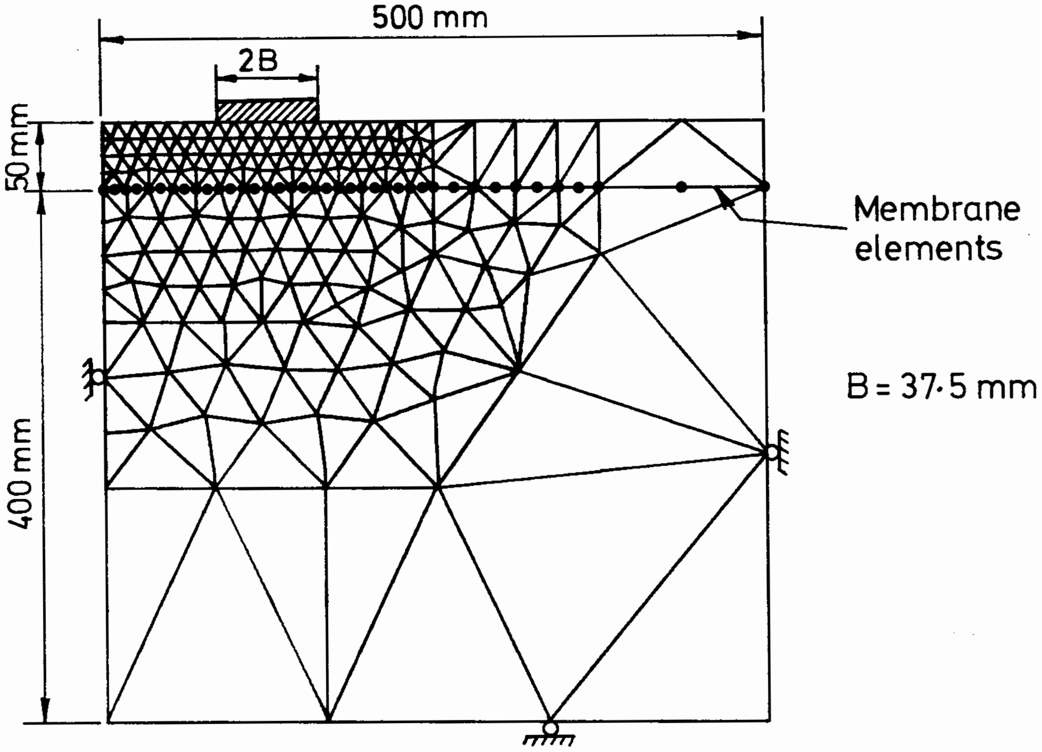

Figure 7.13: Mesh D

The finite element mesh used in the numerical study of these dual footing tests is illustrated in Figure 7.13. In developing this mesh, the intention was to keep the element densities similar to those used in the single footing calculations so that the results would be comparable. These analyses were again based on a perfectly rough footing, and were performed by prescribing a total displacement of 30 mm to the footing base. It was found to be necessary to use 200 displacement steps, rather than 150 as used in the single footing calculations, in order to ensure stability of the numerical algorithms used to perform the 'stress update' calculations.

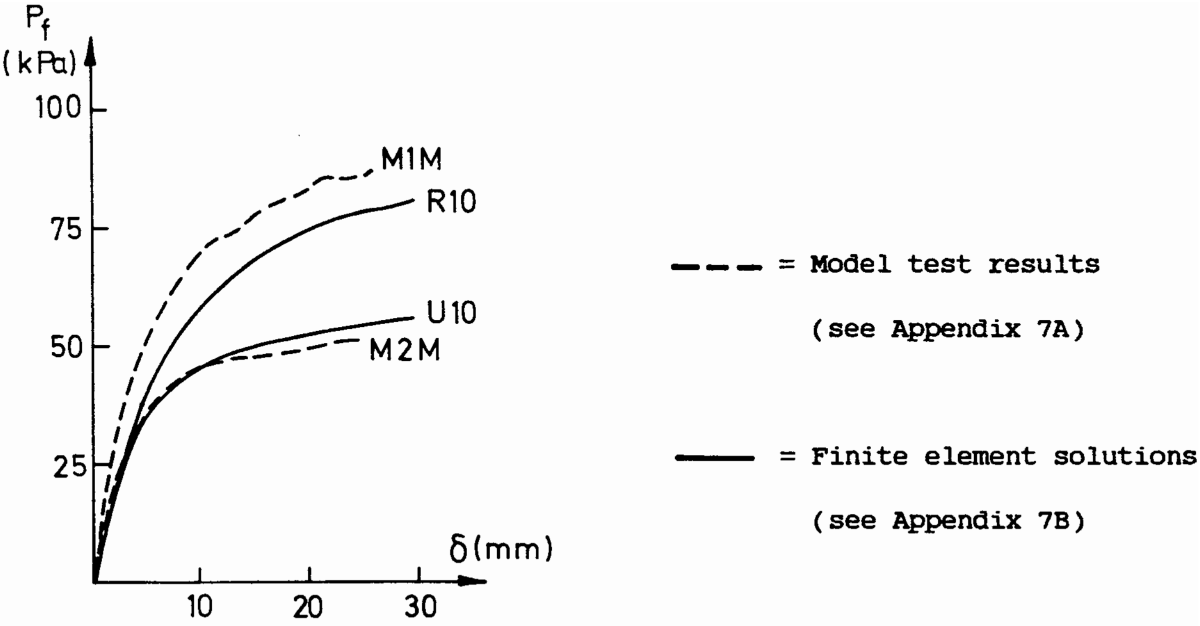

Figure 7.14: Dual Footing Model Test Results and Finite Element Predictions

The load/displacement curves for both theory and experiment are plotted in Figure 7.14. These results differ from those obtained for the single footing with the same fill thickness and subgrade strength, in that the finite element solution underestimates the capacity of the road for all values of displacement. An explanation of this result is that the reinforcement has the effect of coupling the footing loads together in such a way as to increase the depth of the failure zone thus mobilising clay of a greater average shear strength than that assumed in the finite element model. In the unreinforced case, the numerical and experimental results are similar indicating that the footings are acting independently. The deformed mesh at the end of the reinforced calculation (i.e. footing displacement = 30mm) is depicted in Figure 7.15.

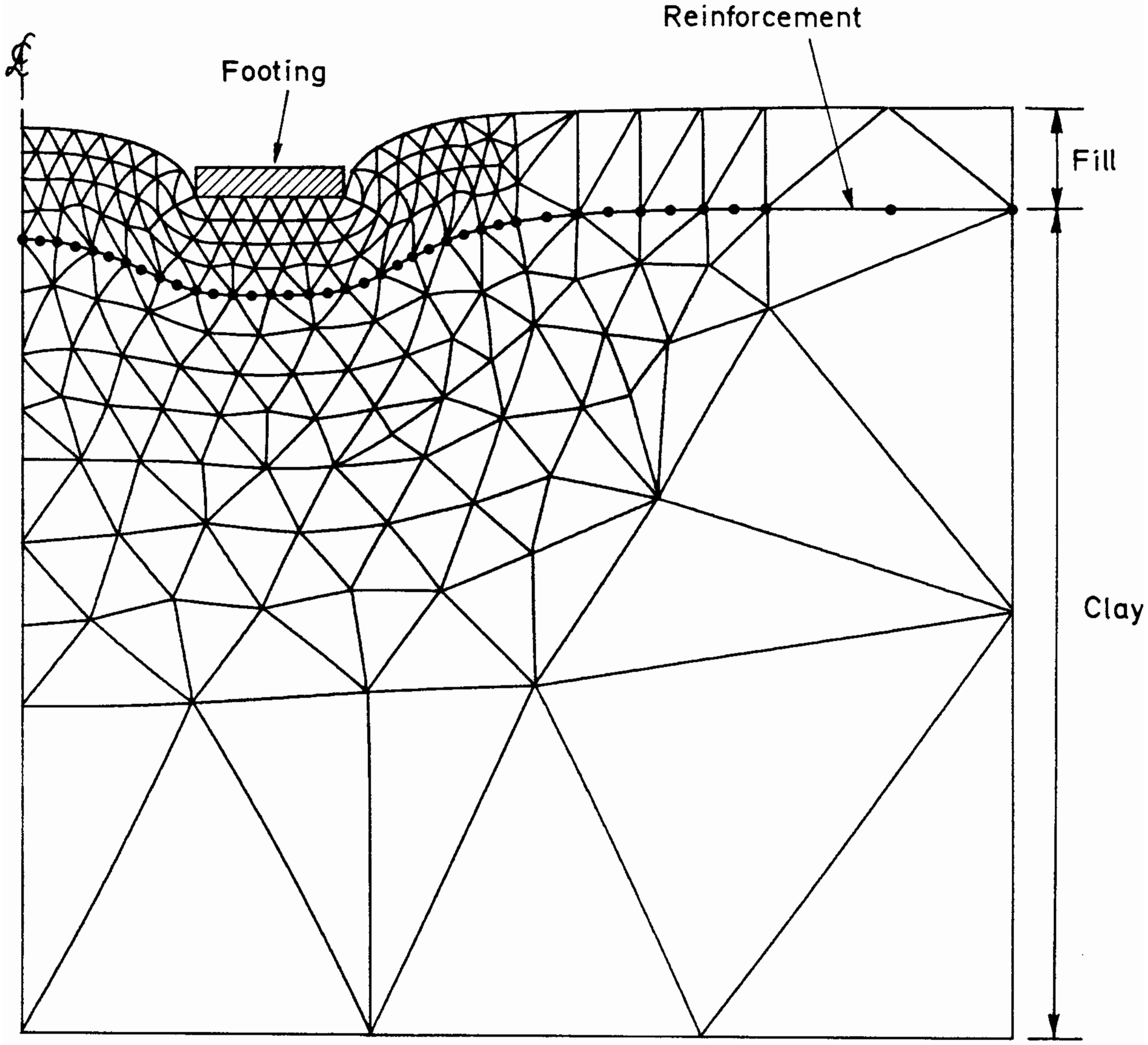

Figure 7.15: Deformed Mesh at End of Calculation R10

APPENDIX 7A

Summary of Tests Performed by Love (1984)

The tests were performed using the rig shown diagramatically in Figure 7.1. Single or dual footings were jacked into the model road at an approximate rate of 2.5 mm/s to a total depth of 50 mm.

In this summary of the conditions used in these tests, the following nomenclature is used:-

s_{sv} = Shear vane measurement made at a depth of 55mm below the trimmed clay surface.

s_n = Nominal clay strength

H = Fill thickness

The reference scheme adopted in this appendix is identical to that adopted by Love. The units of shear strength are kPa, and fill thickness is given in millimeters.

Single Footing Subgrade-Only Tests

s_n	s_{sv}	**Reference**
6.0	6.1	D2L
9.0	9.6	E1R
9.0	8.7	E2R
14.0	14.4	F1R

Single Footing Model Road Tests

(a) Reinforced

H	s_n	s_{sv}	Reference
50	6.0	5.9	A2M
50	9.0	8.9	B1M
50	14.0	15.2	C1M
75	6.0	5.6	D2M
75	9.0	8.5	E1M
75	14.0	13.0	F2M
100	6.0	5.8	G2M
100	9.0	8.8	H1M
100	14.0	13.5	K2M

(b) Unreinforced

H	s_n	s_{sv}	Reference
50	6.0	6.0	A1M
50	9.0	8.8	B2M
50	14.0	12.7	C2M
75	6.0	5.6	D1M
75	9.0	8.2	E2M
75	14.0	13.3	F1M
100	6.0	5.9	G1M
100	9.0	8.5	H2M
100	14.0	14.8	K1M

Dual Footing Model Road Tests

H	s_n	s_{sv}	Reference
50 (Unreinforced)	6.0	6.1	M2M
50 (Reinforced)	6.0	6.4	M1M

APPENDIX 7B

Parameters used in Finite Element Calculations

The following parameters are common to all of the finite element unpaved road back-analysis calculations.

(a) Clay Poisson's ratio is 0.49

(b) Fill parameters are:-

$E = 4000$ kPa, $\nu = 0.35$, $\phi = 32^{o}$, $\gamma_a = 0.6$

(c) The reinforcement is treated as deforming in plane stress and assigned the properties:-

$Et_o = 28$ kN/m $\nu = 0.5$

where E is the Young's modulus of the reinforcement material and t_o is the original thickness.

(d) Soil unit weight is 19 kN/m^3 for both the fill and the clay.

The remainder of the parameters used in the finite element computations are listed below.

Single Footing Subgrade-Only Calculations

Ref.	**Mesh**	**Clay** c_{ps}	**Clay** G	**Number of calculation steps**	**Corresponding Model Test Ref.**
S1	B	5.49	170	110	D2L
S2	B	8.64	268	110	E1R
S3	B	7.83	243	110	E2R
S4	B	13.00	403	110	F1R

Unpaved Road Back-Analysis Calculations

(a) Reinforced

Ref.	**Mesh**	**Clay** c_{ps}	G	**Number of calculation steps**	**Corresponding Model Test Ref.**
R1	A	5.31	165	150	A2M
R2	A	8.01	248	150	B1M
R3	A	13.70	425	150	C1M
R4	B	5.04	156	150	D2M
R5	B	7.65	237	150	E1M
R6	B	11.70	363	150	F2M
R7	C	5.22	162	150	G2M
R8	C	7.92	246	150	H1M
R9	C	12.15	377	150	K2M
R10	D	5.76	179	200	M1M

(b) Unreinforced

Ref.	**Mesh**	**Clay** c_{ps}	G	**Number of calculation steps**	**Corresponding Model Test Ref.**
U1	A	5.40	167	150	A1M
U2	A	7.92	246	150	B2M
U3	A	11.43	354	150	C2M
U4	B	5.04	156	150	D1M
U5	B	7.38	229	150	E2M
U6	B	12.00	372	150	F1M
U7	C	5.31	165	150	G1M
U8	C	7.65	237	150	H2M
U9	C	13.30	412	150	K1M
U10	D	5.49	170	200	M2M
U11	D	5.76	179	200	–
U12	A	5.31	165	150	–

Notes

(i) All values of strength and stiffness given in this appendix are quoted in units of kPa.

(ii) See Figures 7.3, 7.7, 7.8 and 7.13 for finite element meshes.

(iii) See Appendix 7A for parameters used in model tests.

(iv) U11 and U12 do not correspond to a model test but are repeats of R10 and R1 in which the reinforcement is absent.

CHAPTER 8 MECHANISMS OF REINFORCEMENT

8.1 Introduction

The back-analysis calculations described in Chapter 7 show that the finite element model described in this thesis is capable of making accurate predictions of the load/deformation behaviour of a reinforced unpaved road under conditions of plane strain monotonic loading. This finite element model, however, cannot be considered to be a practical design tool in its own right since reinforced unpaved roads are generally low cost structures and in most cases the use of sophisticated numerical methods in design would be uneconomic.

The design of reinforced unpaved roads is currently based on simple analytical models of behaviour and this practice is likely to continue. The design models that are currently available, however, are generally considered to be unsatisfactory since they are based on oversimplified assumptions regarding the nature of the reinforcement mechanisms. In order to improve these analytical design methods, it is necessary to obtain a better understanding of these mechanisms, and this can be achieved, at least in part, by finite element analyses of the sort described in this thesis.

In this chapter, the separate reinforcement mechanisms that have been identified as a result of previous studies of the reinforced unpaved road are described. The results of two of the finite element back-analysis calculations described in Chapter 7 are then discussed in further detail with a view to identifying the reinforcement mechanisms in operation in these particular cases. The numerical solutions chosen for this study are R10 (see Appendix 7B) which involves a dual footing, and R1 which is the single footing calculation corresponding to the same fill thickness and nominal clay strength. In order to provide a comparison with the case where the reinforcement is absent, two additional unreinforced calculations have been performed (U11 and U12 in Appendix 7B) in which the material properties are identical to those used in the corresponding reinforced analyses.

The numerical predictions of reinforcement mechanisms described in this chapter are limited to the case of a single or dual footing with one combination of fill thickness, subgrade strength and reinforcement stiffness. No indication is given as to how the mechanisms might be affected by changes in geometry or material properties.

8.2 Definition of Mechanisms

The reinforcement mechanisms that are generally considered to act in a reinforced unpaved road are defined and described below.

(i) Membrane Effect

When a wheel load is applied to the surface of the road, tensile forces are set up in the reinforcement by the shear stresses acting at the interface with the soil. If these tensile forces are coincident with appreciable curvature of the reinforcement then the normal stresses in the soil acting on each side of the reinforcement are unequal. This effect tends to reduce the normal stresses transmitted to the subgrade immediately underneath the load which increases the capacity of the road.

(ii) Restraint Effects

The reinforcement can restrain the displacements in both the fill and the subgrade in such a way as to increase the strength and stiffness of the structure. Two such restraint mechanisms have been proposed and these are defined and described below.

Effect A: When the soil displacements become appreciable, the reinforcement tends to restrain heave deformation of the subgrade on each side of the load by membrane action associated with reversed curvature of the reinforcement. The reinforcement therefore applies an additional surcharge loading to the surface of the subgrade which increases the vertical bearing capacity underneath the load.

Effect B: The reinforcement reduces the tensile strains at the base of the fill, and this improves the load-spread action of the layer thus reducing the magnitude of the vertical stresses at the fill base. This particular mechanism depends critically on the roughness of the soil/reinforcement interface and the stiffness of the reinforcement.

(iii) Reinforcement Against Local Failure

The reinforcement prevents the punching of the individual fill particles into the subgrade, thus ensuring that a distinct boundary is maintained between the soil layers.

(iv) Shear Stress Effect

In the unreinforced unpaved road, the fill layer transmits shear stresses as well as normal stresses to the subgrade. These shear stresses tend to reduce the vertical bearing capacity of the subgrade. If a reinforcing layer is placed at the base of the fill, there is evidence to suggest that these shear stresses are reduced thus increasing the subgrade bearing capacity. The amount by which the shear stresses are reduced is likely to depend on the relative stiffness of the reinforcement and the surrounding soil. This effect is ignored in the simple analytical design methods, but has been identified in the model tests performed by Love (1984) and has also been predicted by various finite element studies (e.g. Boutrup et al. (1983)).

8.3 Single Footing Analysis

The finite element calculation reference R1 described in Chapter 7 is discussed in greater detail in this section with a view to identifying the reinforcement mechanisms in operation in this particular case.

The variation of reinforcement tension with position obtained from this finite element calculation for footing displacements of 0.8B and 0.4B, where B is the footing half-width, is plotted in Figure 8.1. It is clear from this diagram that as the footing displacement increases, then the point of zero tension moves outwards and the magnitude of the tensile forces increases with the general shape of the curve being preserved. It is also noticeable that for both values of footing displacement the maximum tensile force occurs at a point almost directly underneath the

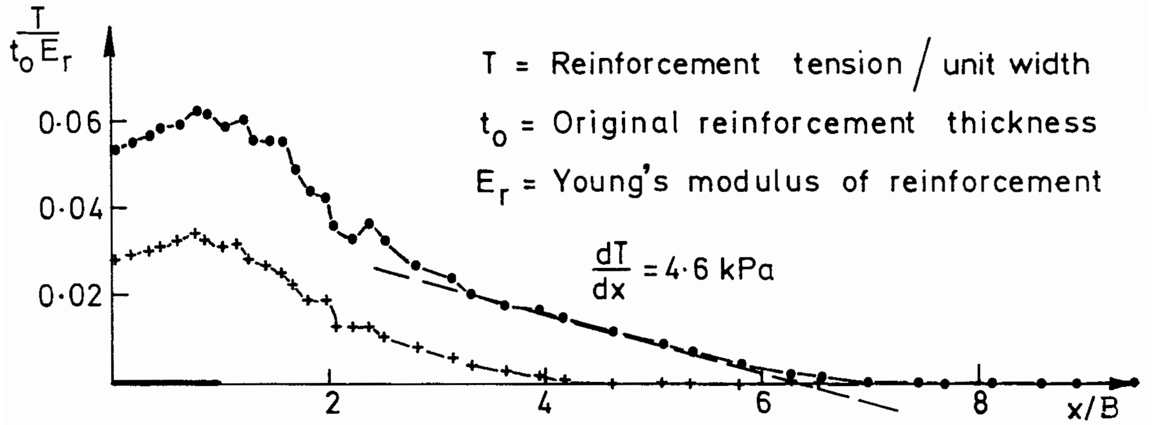

Reinforcement Tension

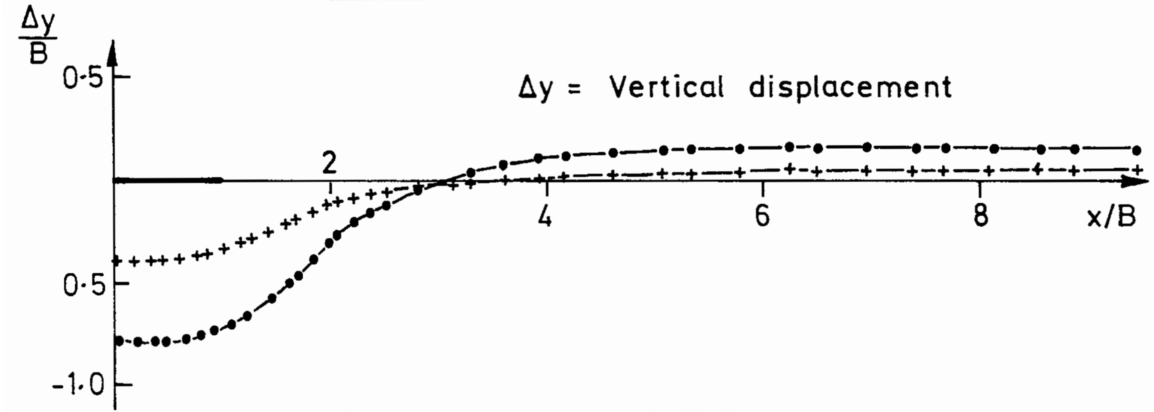

Vertical displacement of Reinforcement

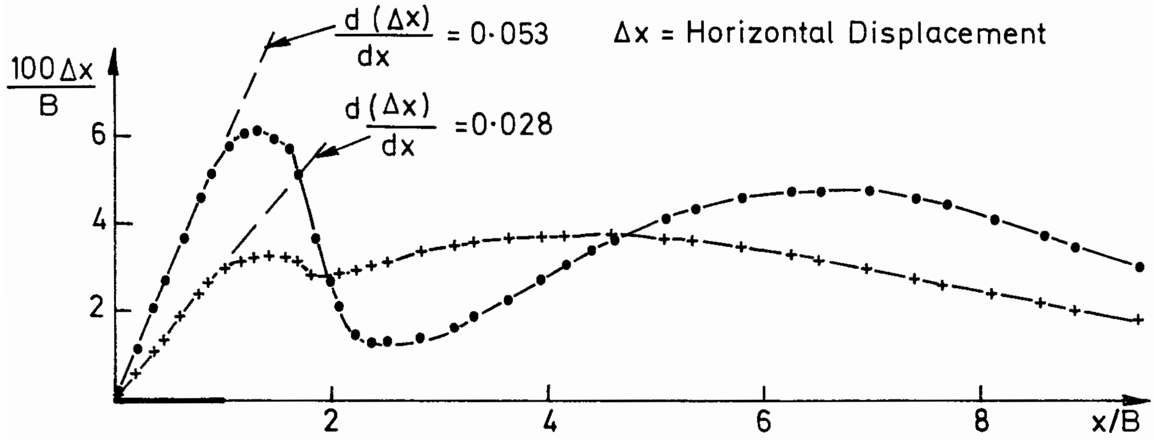

Horizontal displacement of Reinforcement

+ $\delta/B = 0{\cdot}4$

● $\delta/B = 0{\cdot}8$

Finite element calculation R1

Figure 8.1: Reinforcement Tension and Displacement (Single Footing)

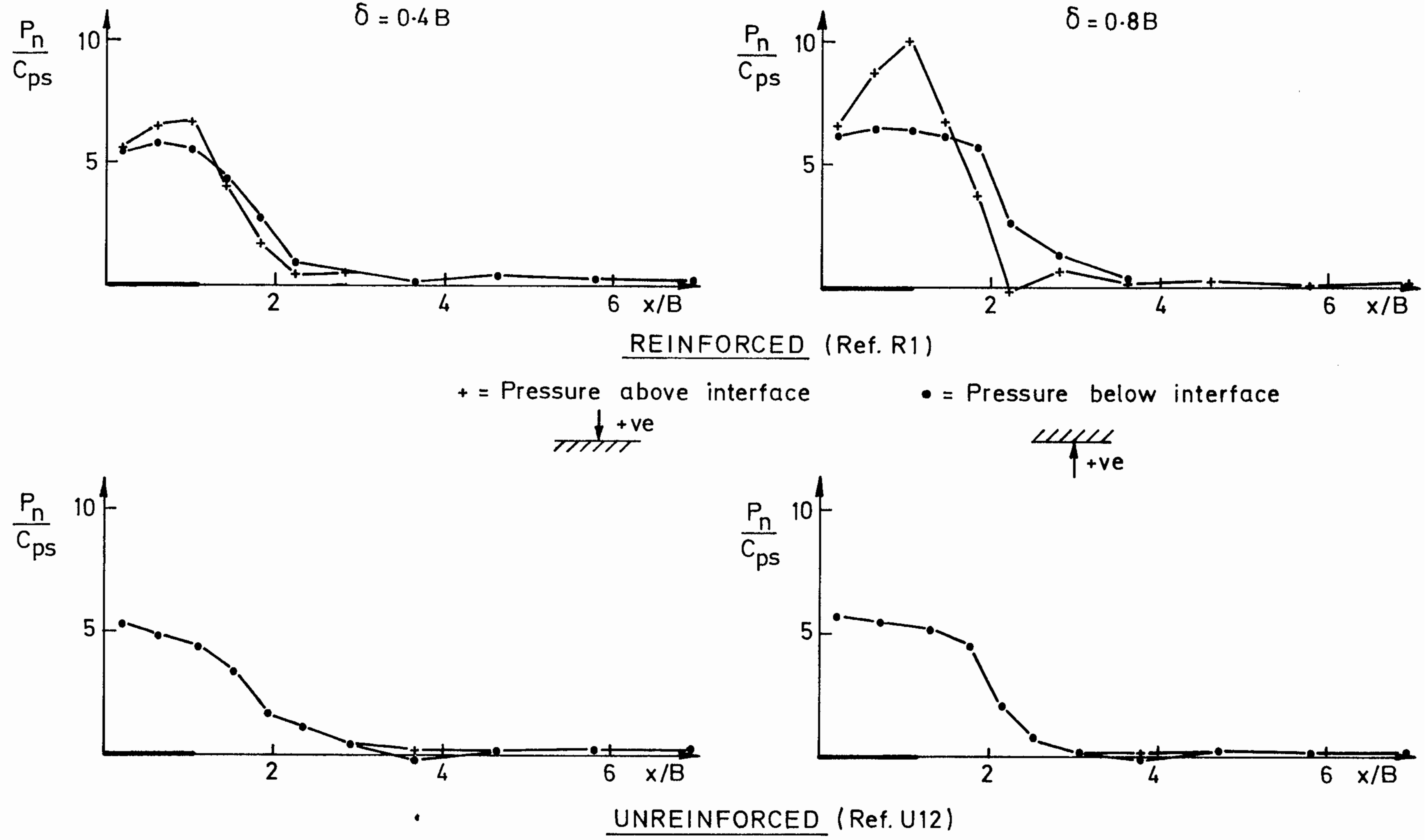

Figure 8.2: Stresses Normal to Interface (Single Footing)

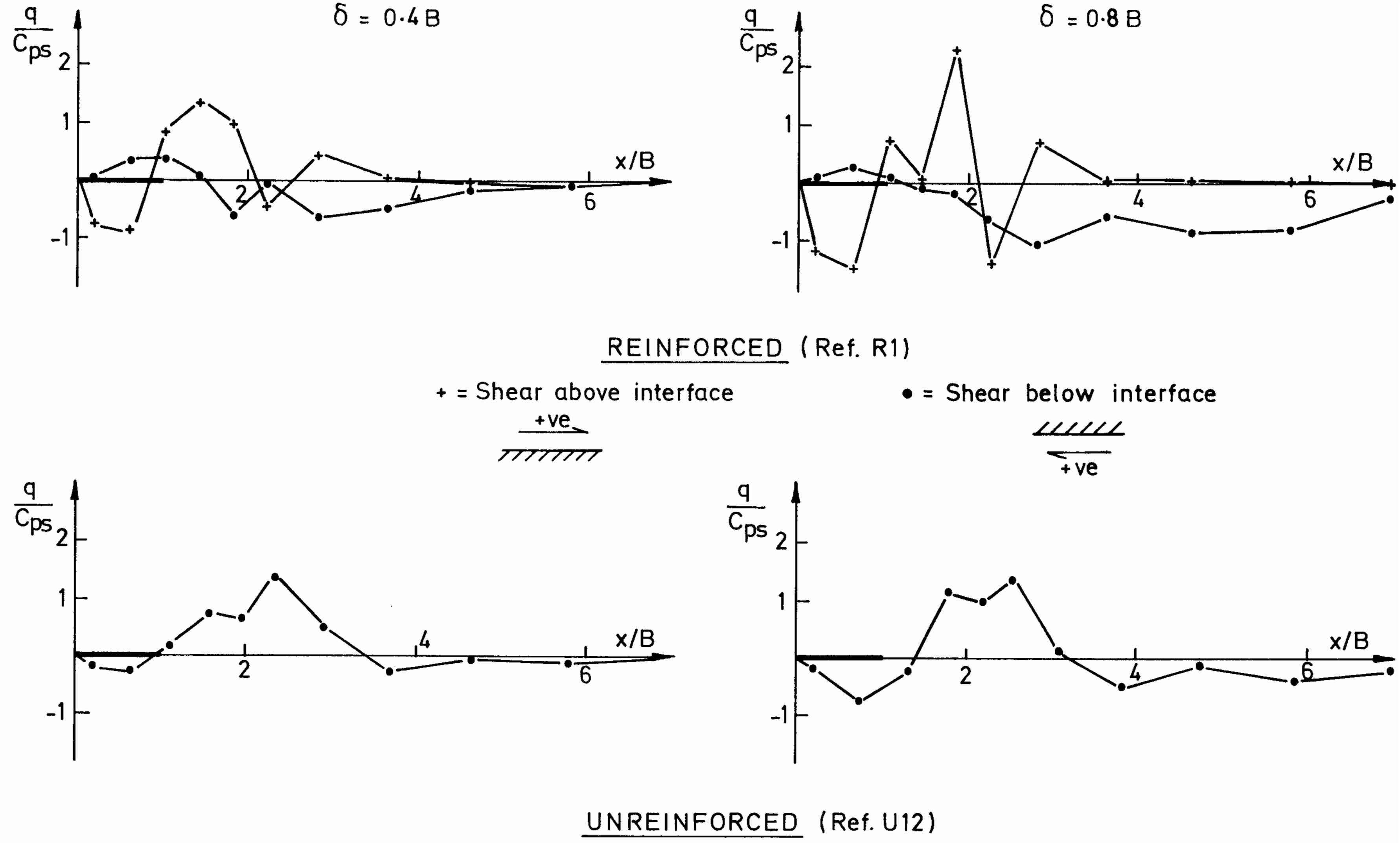

Figure 8.3 Shear Stresses at Interface (Single Footing)

footing edge. This type of behaviour has also been predicted by Zeevaert (1980) using an axi-symmetric finite element model, and has been observed in the plane strain model tests performed by Gourc and Riondy (1985).

The vertical displacements of the reinforcement obtained from the finite element calculation are also plotted in Figure 8.1, from which it is clear that the point of zero vertical displacement moves outward slightly as the footing displacement increases. This type of behaviour was also observed in the model tests performed by Love(1984).

Since the slope of the reinforcement is zero on the footing centre-line, the strain in the reinforcement at this point may be calculated from the slope of the horizontal displacement, which is also plotted in Figure 8.1. The gradients of the horizontal displacement curves agree well with the reinforcement strain on the footing centre-line which confirms the general consistency of the results.

The normal stresses acting on reinforcement for the reinforced calculation, and on the fill/clay interface for the unreinforced case are plotted in Figure 8.2. The 'membrane effect' is clearly evident in the reinforced case since the normal stresses above the reinforcement exceed those below in the area immediately underneath the footing. The magnitude of this normal stress difference is small beneath the footing centre line where the reinforcement curvature is minimal, and reaches a peak at a point roughly underneath the footing edge where both the reinforcement tension and curvature are relatively large as indicated in Figure 8.1. Outside the area immediately below the footing the sign of the normal stress difference is reversed due to the reversed curvature of the reinforcement. This increases the surcharge on the subgrade, and corresponds to 'restraint effect A' defined in Section 8.1. It is detectable in Figure 8.2 that the normal subgrade stress in the area immediately underneath the footing is slightly greater for the reinforced case which is at least partly due to this mechanism. These solutions also show that in this case the reinforcement tends to reduce the width of the loaded area at the fill base, thus it has a detrimental effect on the mechanism of load spread. This is a surprising result, and contrary to the usual assumption that the reinforcement improves the load spread in the fill.

The shear stresses acting on the soil/reinforcement and fill/clay interfaces obtained from this finite element calculation are plotted in Figure 8.3 but are more difficult to interpret than the normal stress results since they show marked variations along the length of the interface. Some of these variations are almost certainly a result of the discretization errors involved in the numerical model and have no physical significance. It may be deduced, however, that the reinforcement has the general effect of reducing the shear stresses transmitted to the subgrade immediately underneath the load. (It should be noted in making this comparison that the shear stresses are compared for the same footing displacement, rather than footing load, which is larger in the reinforced case). The results plotted in Figure 8.3 also show that appreciable negative shear stresses act on the subgrade well away from the footing when the displacement is large. These stresses arise from the horizontal movement of clay displaced by the footing, and are larger for the reinforced case since the reinforcement is able to offer greater lateral restraint than the fill layer.

The shear stress plots in Figure 8.3 for the reinforced case are consistent with the reinforcement tension plotted in Figure 8.1 in that the points of zero tension and zero shear stress are approximately coincident. For the larger displacement, the shear stress acting on the reinforcement for $4B < x < 6B$ is slightly less than c_{ps}, which corresponds well with the measured slope of the tension curve in Figure 8.1.

8.4 Dual Footing Analysis

The results of finite element calculation reference R10 (see Appendix 7B) are described in further detail in this section. This analysis involves a dual footing but is otherwise similar to the single footing calculation described in the previous section.

The reinforcement tensions obtained from the finite element analysis are plotted in Figure 8.4 for the same two values of footing displacement studied in the single footing case. These curves show similar trends to those obtained from the single footing calculation in that peak values of tension occur roughly underneath the footing edges, and the point of zero tension moves outwards as the footing displacement increases. A comparison between Figures 8.1 and 8.4 show that the magnitudes of reinforcement tension and displacement are generally larger for the dual footing case. The reinforcement displacements are also plotted in Figure 8.4 and are similar to those obtained for the single footing calculation, except that the magnitude of the heave displacements is generally greater.

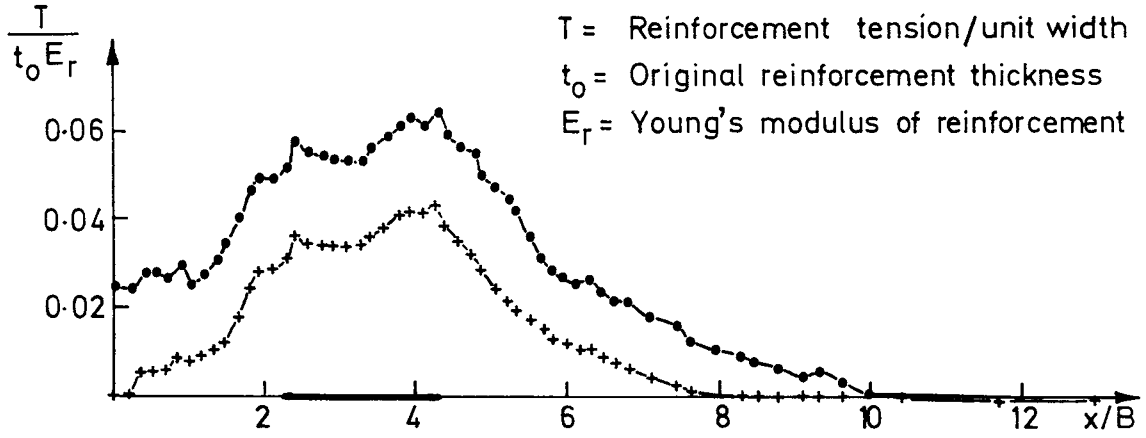

Reinforcement Tension

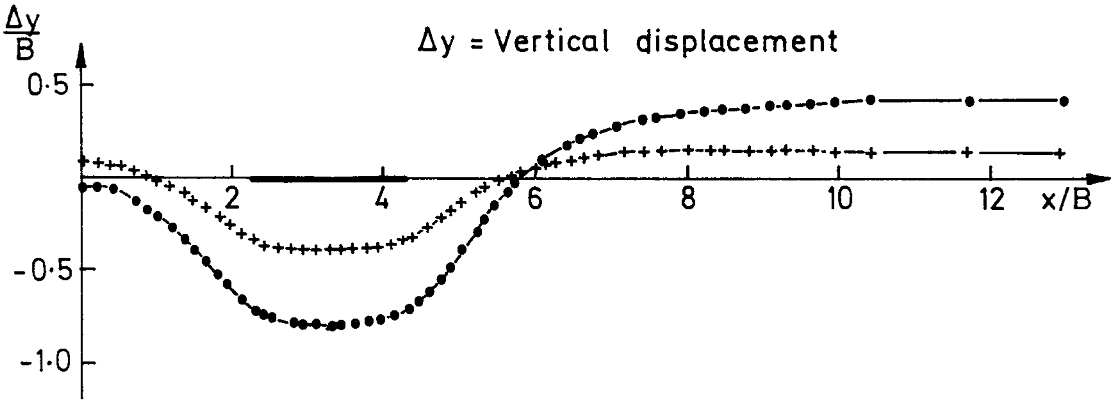

Vertical displacement of Reinforcement

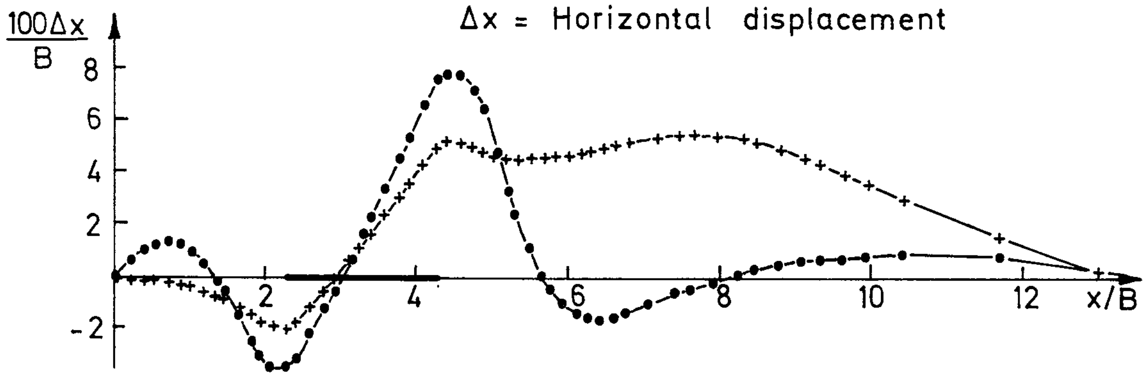

Horizontal displacement of Reinforcement

+ δ/B = 0·4 Finite element calculation R10

● δ/B = 0·8

Figure 8.4: Reinforcement Tension and Displacement (Dual Footing)

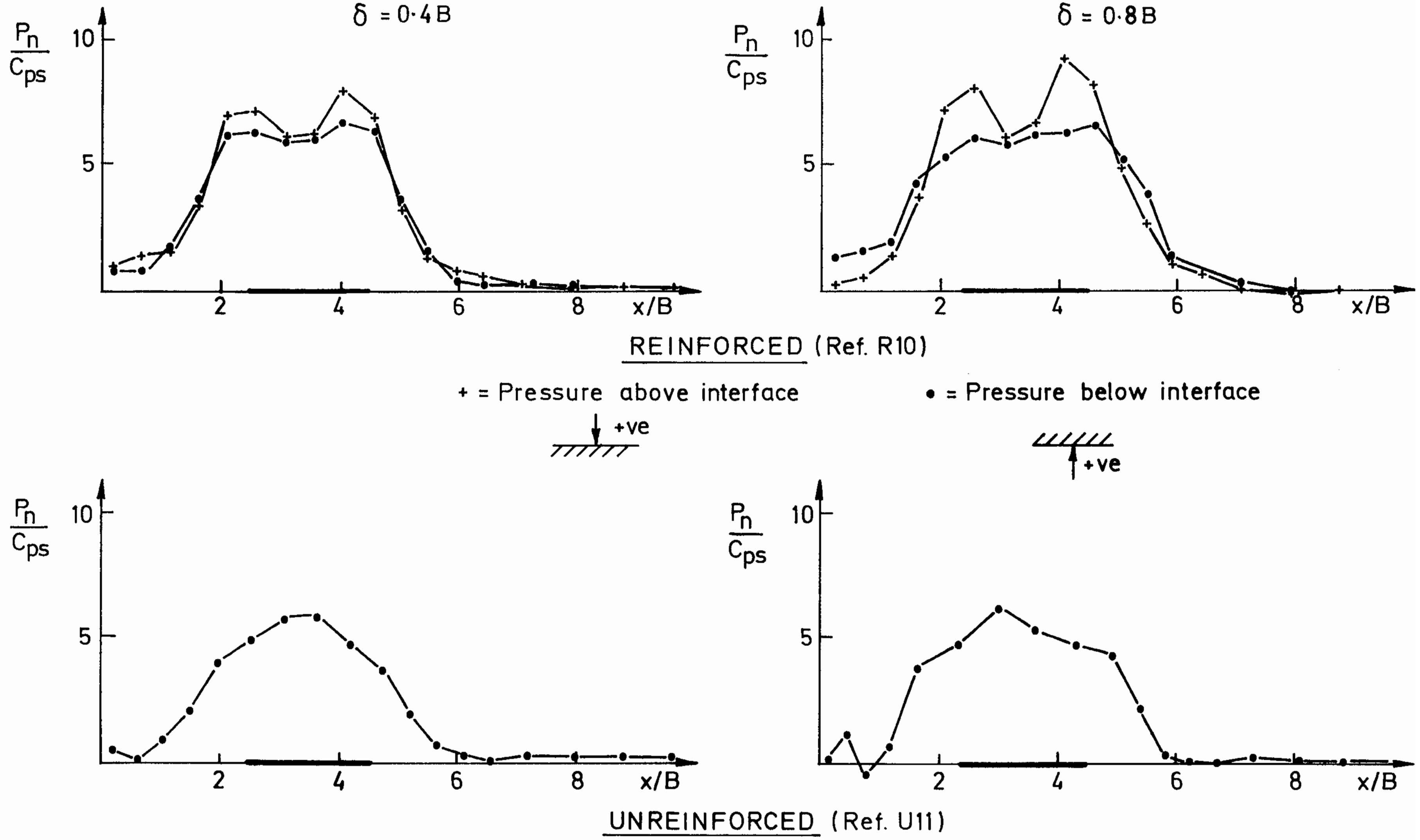

Figure 8.5: Stresses Normal to Interface (Dual Footing)

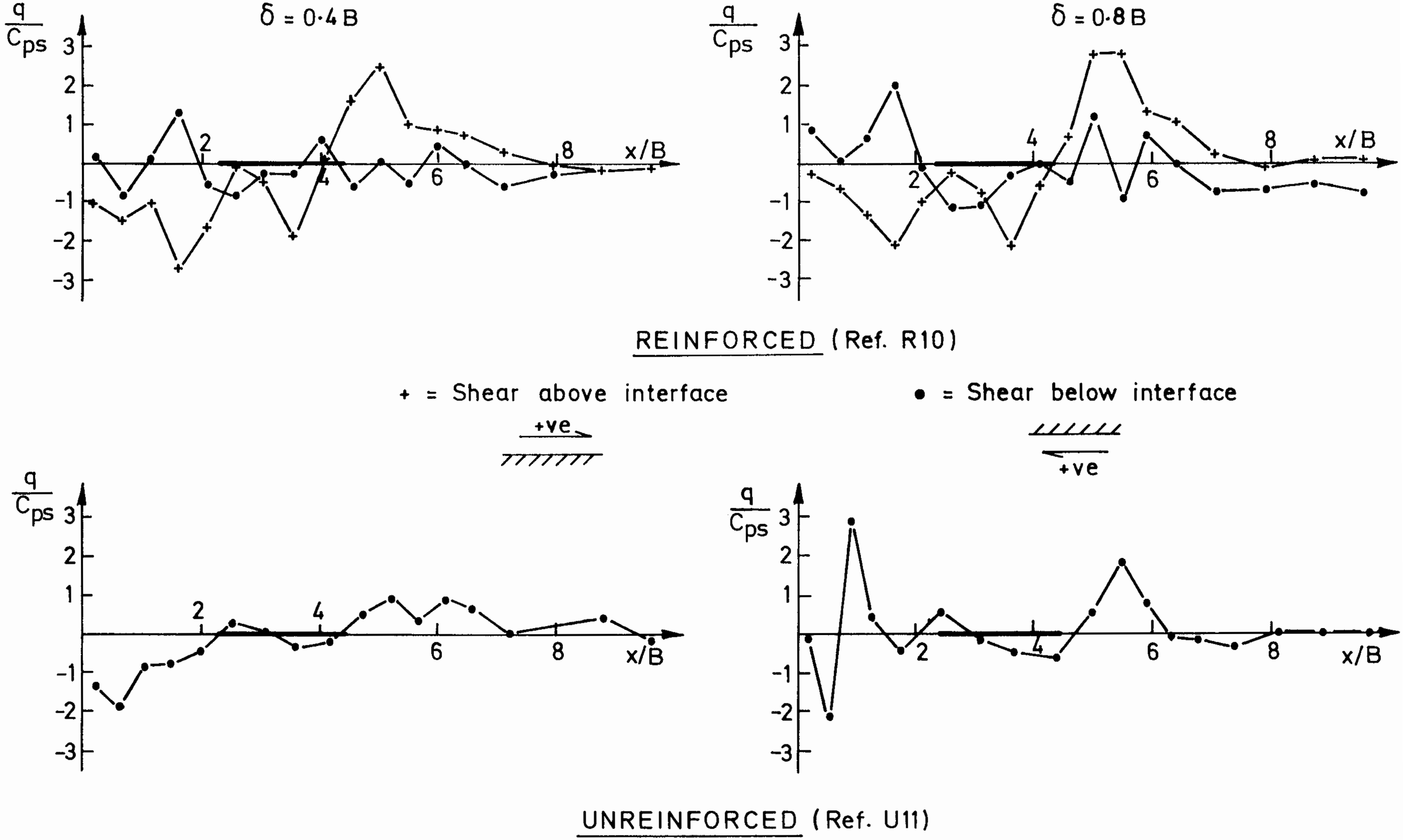

Figure 8.6: Shear Stresses at Interface (Dual Footing)

The normal stresses acting on the reinforcement are plotted in Figure 8.5, and as was the case for the single footing results the presence of the 'membrane effect' is clearly apparent. The results are also similar in that immediately outside the loaded area the reversed curvature of the membrane increases the surcharge on the subgrade. The magnitude of this surcharge is greatest in the region between the footings. This result is to be expected since the coupling between the two loads tends to increase both the reinforcement tension and curvature in this area.

The shear stresses acting on the reinforcement/soil, and fill/clay interfaces are plotted in Figure 8.6 and as was the case for the single footing calculation described in Section 8.3, the results show large spatial variations. These errors arise from the general tendency of the finite element method to produce solutions which have local erroneous variations even though they are globally correct, and this figure is included here in order to illustrate the limitations of this particular formulation.

CHAPTER 9 TWO EXISTING DESIGN METHODS

9.1 Introduction

Several simple analytical methods have been proposed for the design of reinforced unpaved roads, and these are reviewed briefly in Chapter 1. Two of these design methods, namely those proposed by Giroud and Noiray (1981) and Sowers et al. (1982), are discussed in greater depth in this chapter. The design methods are first described in detail, and are then each used to model one of the reinforced unpaved road tests described in Chapter 7. The analytical models are compared with the experimental results and the corresponding finite element back-analysis solutions in order to assess the assumptions on which these simple design models are based. The model tests chosen for this comparison correspond to the single and dual footing finite element calculations described in Chapter 8. The Giroud and Noiray method, which models a dual wheel load, is compared with the experimental and numerical results obtained for a dual footing, and the Sowers method is compared with the single footing case since it treats each wheel in isolation.

9.2 Giroud and Noiray Method

This was one of the first simple analytical design methods of the reinforced unpaved road to be proposed in which the reinforcement behaviour is treated in a rational way. Although this model is based on assumptions that clearly oversimplify the behaviour of the road, it has been successful in stimulating interest in design methods and is extensively cited in later work. This design model deals with the interaction that occurs between two wheel loads, and makes the implicit assumption that the soil behaves in a rigid, perfectly-plastic manner. The reinforcement is assumed to be linearly elastic. This design procedure is based on the analysis of a reinforced unpaved road under the action of a single monotonic load. The effects of repeated loading are then included by increasing the thickness of the fill layer by an amount derived from an empirical rule. In this description of the Giroud and Noiray method, the analysis of traffic loading is not included on the basis that the consideration of repeated loading is outside the scope of this thesis.

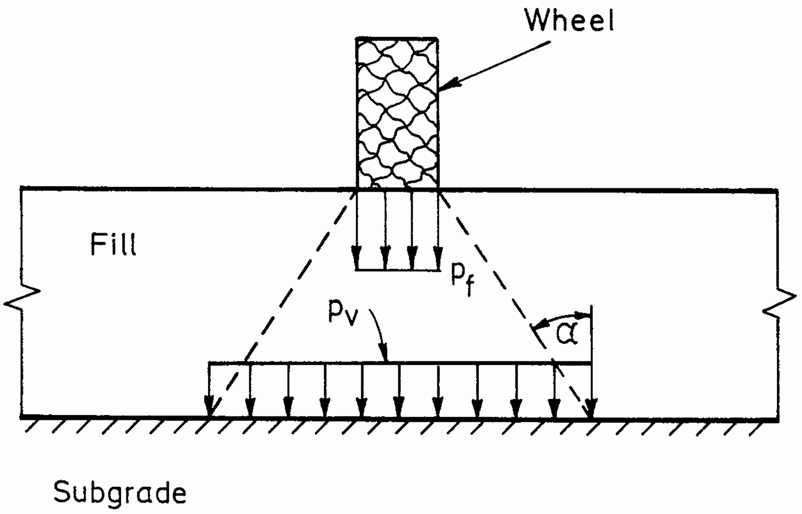

Figure 9.1: Idealised Stresses

In this design model, the wheel load is assumed to be transmitted through the fill layer such that the vertical stress due to this load is constant over the base of a truncated pyramid whose sides have angle α as shown in Figure 9.1, and zero outside. In order to adjust this design method to model the plane strain case, it is simply necessary to consider that this load spread action occurs in one direction only. The deformed shape of the reinforcement is approximated by three parabolas as shown in

Figure 9.2, where the points of zero vertical displacement correspond to the edges of the loaded area at the fill base. The fill surface is assumed to follow the same profile as the reinforcement, and the rut depth, r, is defined to be the maximum vertical differential displacement at the fill surface.

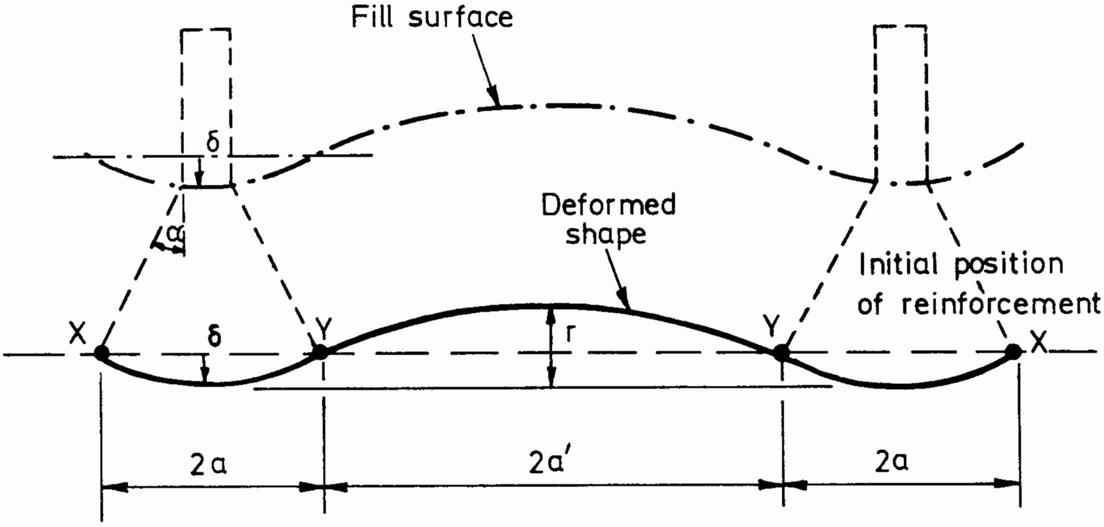

Figure 9.2: Idealised Deformations

For the case when a′ > a (see Figure 9.2), one half of the soil displaced under the load is assumed to contribute to heave between the wheels, from which the geometric relationship may be obtained:-

$$\delta = \frac{ra'}{a + a'} \qquad (9.1)$$

where δ is the maximum downwards displacement of the reinforcement and is equal to the wheel displacement since in this model compaction of the fill underneath the load is neglected. For the case when a > a′, a smaller proportion of the displaced soil is assumed to contribute to heave between the wheels, and the following relationship between the rut depth and the wheel displacement is derived:-

$$\delta = \frac{2ra^2}{2a^2 + 3aa' - a'^2} \qquad (9.2)$$

In order to calculate the strains in the reinforcement, points X and Y in Figure 9.2 are initially assumed to be pinned. The average strain in the three distinct parabolic portions of the reinforcement are then calculated using equations (9.1) or (9.2) in conjunction with the appropriate geometric relationship between the arc and subtended chord of a parabola.

For the case when a' > a, the average strain in portions X-Y is greater than in Y-Y. It is assumed in this case that the overburden between the wheels is insufficient to prevent slippage of the reinforcement over portion Y-Y so the horizontal restraints at points Y are removed. The engineering strain in the reinforcement is then assumed to be constant between points X and is given by the expression:-

$$\epsilon = \frac{b + b'}{a + a'} - 1 \qquad (9.3)$$

where b is the half-length of the reinforcement for portion X-Y and b' is the half-length for Y-Y. For the case when a > a' and points X and Y are pinned, then the average strain in portion Y-Y exceeds that in portions X-Y, and in this case the horizontal restraint at Y is retained. The average strain in the portions of reinforcement under the wheels is therefore give by:-

$$\epsilon = \frac{b}{a} - 1 \qquad (9.4)$$

The load-displacement response of the road is then obtained by considering the vertical equilibrium of portion X-Y of the reinforcement as shown in Figure 9.3.

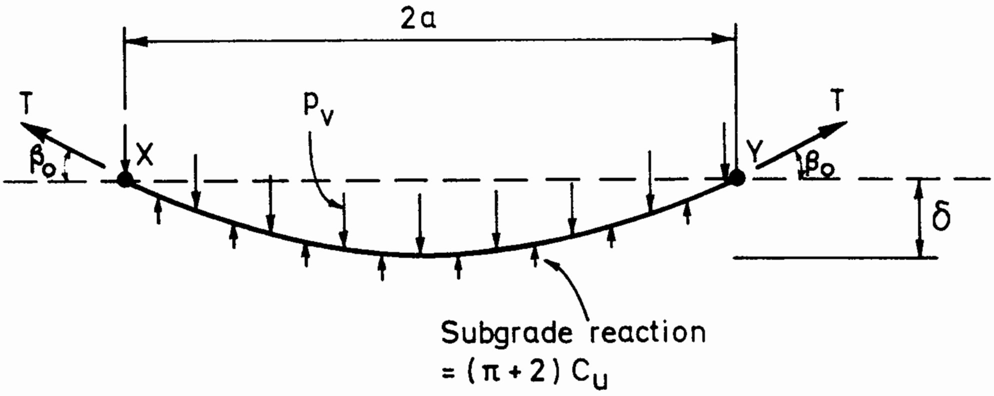

Figure 9.3: Vertical Equilibrium of Reinforcement

The tension, T, is assumed to be constant in this portion and is given by:-

$$T = K \epsilon \qquad (9.5)$$

where ϵ is the average strain defined either by equation (9.3) or (9.4), and K is the reinforcement modulus. The vertical reaction between points X and Y is assumed to be the constant value of $(\pi + 2)c_u$, where c_u is the undrained plane strain shear strength of the subgrade. From the geometry of the parabola, the slope at points X and Y is given by:-

$$\tan(\beta_o) = \eta \qquad (9.6)$$

where:-

$$\eta = \frac{2\delta}{a} \qquad (9.7)$$

and the footing displacement, δ, is related to the rut depth, r, by equations (9.1) or (9.2). The condition of vertical equilibrium may be used to give an expression for p_v, the vertical stress at the base of the fill:-

$$p_v = (\pi + 2)c_u + \frac{T}{a}\sin(\beta_o) \tag{9.8}$$

Substituting for T from equation (9.5) and for $\sin(\beta_o)$ from equation (9.6) gives:-

$$p_v = (\pi + 2)c_u + \frac{K \epsilon \eta}{a\left[1 + \eta^2\right]^{1/2}} \tag{9.9}$$

which defines the relationship between the rut depth, r, and the vertical stress at the base of the fill, p_v, for a single monotonic load. The vertical pressure immediately underneath the wheel, p_f, is related to p_v by considering the mechanism of load spread in the fill:-

$$p_f A = p_v A' \tag{9.10}$$

where A is the contact area under the wheel and A' is the area at the base of the truncated pyramid defining the load spread.

In order to obtain a reasonable fit with the experimental data, the proposal is made in this design method that for the unreinforced case the maximum vertical subgrade reaction should be set to πc_u, the elastic limit, rather than $(\pi + 2)c_u$ which is the value used for the reinforced case. This difference in bearing capacity is justified on the basis that the reinforcement provides additional confinement to the subgrade. It is likely, however, that this observed reduction of subgrade bearing capacity in the unreinforced case is caused by the 'shear stress effect' (see Section 8.2).

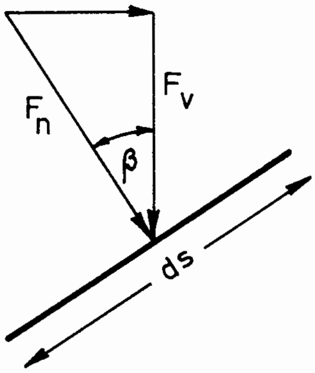

Figure 9.4: Normal and Vertical Forces on Reinforcement

In order to compare numerical and analytical predictions of behaviour, it is necessary to obtain the relationship between the vertical stress acting on the reinforcement, and the normal stress implied by the assumptions made in the Giroud and Noiray model. In order to obtain this relationship, consider the normal force F_n and the vertical force F_v acting on a portion of reinforcement of length ds as shown in Figure 9.4. The assumption is made in the Giroud and Noiray model that the reinforcement tension is constant which implies that the shear stresses acting on the reinforcement are zero. The normal and vertical forces on the element are therefore related by the expression:-

$$F_v = F_n \cos(\beta) \qquad (9.11)$$

where β is the angle of inclination of the reinforcement to the horizontal. The vertical stress, p_v, and normal stress, p_n, are therefore given by:-

$$p_v = \frac{F_v}{ds\ \cos(\beta)} \qquad p_n = \frac{F_n}{ds} \tag{9.12}$$

which is combined with equation (9.11) to give the result:-

$$p_v = p_n \tag{9.13}$$

In this design model, therefore, the implication is that a hydrostatic stress system exists at the base of the fill.

9.2.1 Comparison with Finite Element Results

The assumptions made in the Giroud and Noiray model are compared in this section with the results of a dual footing model test (ref. M1M) and the corresponding finite element back-analysis (ref. R10). In making this comparison, the Giroud and Noiray method is modified in two points from the original published version in order to make it consistent with the model test and finite element results. Firstly, in the original design model the load spread is assumed to occur in two directions, whereas in this application of the method a plane strain variation is used in which the load spread occurs in one direction only. Secondly, in its original form the Giroud and Noiray model uses as the primary variable the rut depth, r, whereas in order to make direct comparisons between this model and with the numerical and experimental results it is necessary to use the footing displacement, δ, as the primary variable. The material properties used in the Giroud and Noiray model are the same as those used in the finite element analysis with the exception of the angle which is an additional parameter and for these calculations is taken to be:-

$$\tan(\alpha) = 0.65 \tag{9.14}$$

The load/displacement relationship obtained from the Giroud and Noiray model is compared with the results of the finite element analysis and the model test in Figure 9.5.

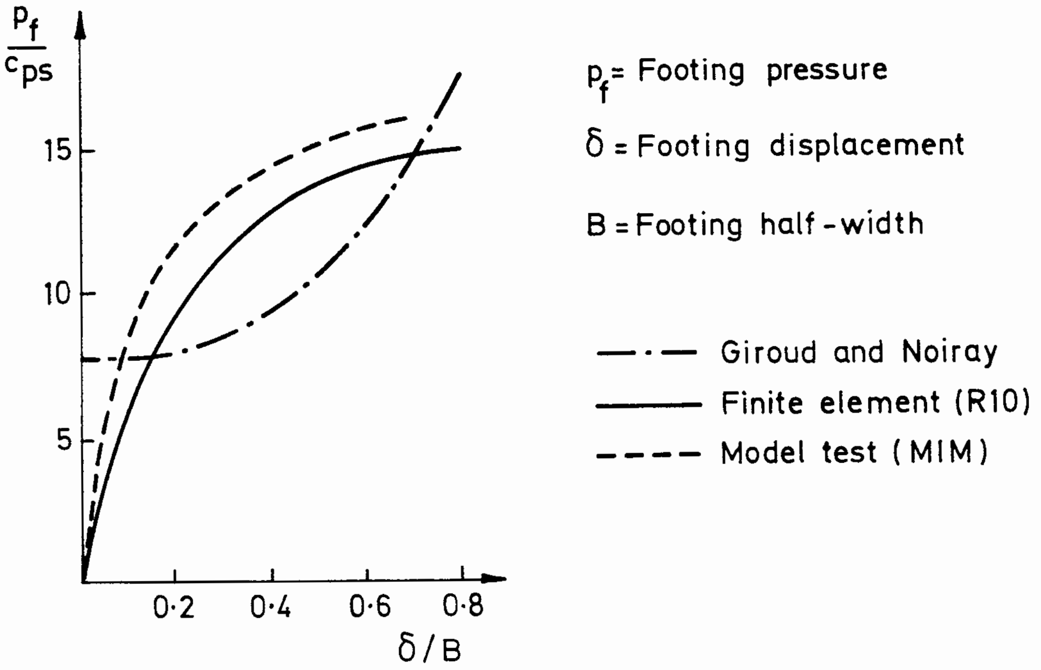

Figure 9.5: Comparison Between Analytical, Numerical and Experimental Load/Displacement Curves

The Giroud and Noiray method clearly predicts an over-stiff response at very small displacements which is a direct consequence of the use of a rigid plastic soil model. As the footing displacement increases, the values of bearing capacity predicted by the analytical model becomes more realistic, but the response differs from the numerical and experimental curves in that the slope increases with footing displacement. This means

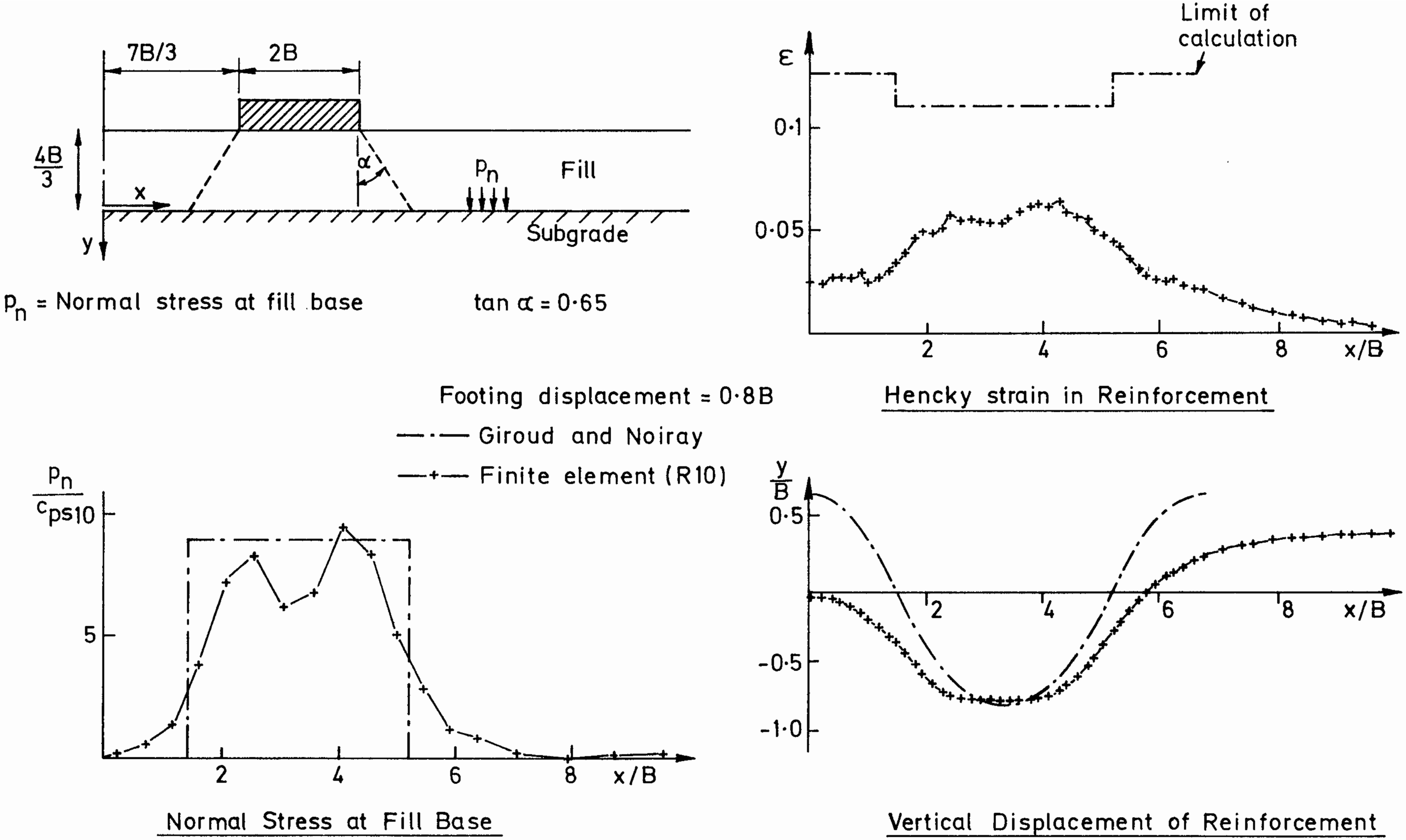

Hencky strain in Reinforcement

Normal Stress at Fill Base

Vertical Displacement of Reinforcement

Figure 9.6: Comparison Between the Giroud and Noiray Model and the Numerical Solutions

that for large footing displacements the Giroud and Noiray model will give an overestimate of the capacity of the road.

The normal stress at the fill base predicted by the Giroud and Noiray model for a footing displacement of 0.8B is plotted in Figure 9.6, and compared with the corresponding finite element solution reproduced from Figure 8.5. The normal stress derived from the Giroud and Noiray method is constant since the assumption of zero frictional stresses acting on the reinforcement implies that a hydrostatic state of stress exists at the base of the fill as shown in Section 9.2. The general magnitude of the normal stresses agree well which is consistent with the fact that at this particular footing displacement the wheel loads predicted by the numerical and analytical methods are similar (see Figure 9.5).

The variation of reinforcement strain implied by the Giroud and Noiray model for this same value of footing displacement is also plotted in Figure 9.6, and compared with the corresponding finite element results reproduced from Figure 8.4. The analytical method clearly predicts magnitudes of strain that in this case are unrealistically large.

The deformed shape of the reinforcement predicted by the Giroud and Noiray model is plotted in Figure 9.6 and compared with the corresponding finite element results. The magnitude of displacement immediately underneath the wheel centre-line calculated using the two methods are similar indicating that in the numerical solution the maximum reinforcement displacement is roughly equal to the footing displacement, which corresponds to the assumption made in the analytical model. The Giroud and Noiray method , however, predicts larger heave displacements than those obtained from the finite element calculation. This is at least partly due to the fact that in the analytical model elastic strains are neglected and an oversimplified mechanism of subgrade heave is adopted.

Two other important limitations of the Giroud and Noiray design method may be identified. Firstly, this design model fails to account for the increase in bearing capacity that is caused by the reversed curvature of the reinforcement outside the loaded area. Another important mechanism, described as the 'shear stress effect' in Section 8.2, arises from the tendency of the reinforcement to reduce the magnitude of the shear stresses transmitted from the fill to the subgrade. It is possible that in some situations this mechanism is of considerable importance, but it is not considered explicitly in this particular design model.

9.3 Sowers Method

The model proposed by Sowers et al. (1982) is one of a number of design methods presented at the Second International Conference on Geotextiles in Las Vegas. The design procedure is based on the results of a series of full scale tests and is a mixture of empiricism and mechanistic reasoning. This method is similar in many respects to the Giroud and Noiray approach, but it differs in that it deals with each wheel load in isolation. The assumed mechanism of load spread in the fill is similar to that adopted in the Giroud and Noiray model in that the vertical stress at the fill base due to the wheel load is taken to be constant over a loaded area of width 2B′ and zero outside (see Figure

9.7). In contrast to the Giroud and Noiray method, the value of B′ is given by an empirical function of wheel displacement in which the width of the loaded area increases with displacement.

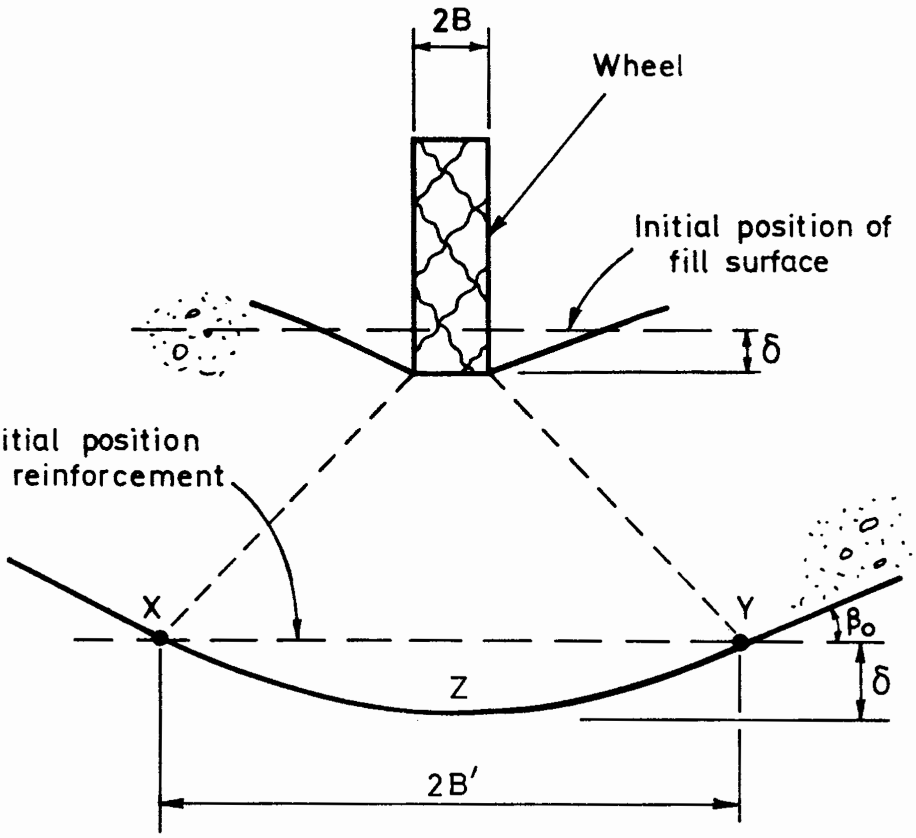

Figure 9.7: Idealised Deformations

In the full scale tests performed by Sowers et al., the displacement of the reinforcement immediately under the centre of the wheel was found to be less than the wheel displacement due to compaction of the fill. An empirical relationship between these displacements, based on the results of these tests, is therefore adopted in this design method. The empirical formula quoted in the original publication, however, is unsatisfactory for general use since it relates only to the fill material and the compaction procedure used in the tests. In order to avoid this problem, the assumption is made in this description of the Sowers method that the maximum downwards displacement of the reinforcement is equal to the wheel displacement which is consistent with the approach adopted in the Giroud and Noiray method.

The deformed shape of the portion of reinforcement beneath the wheel is assumed to be parabolic, with the edges of the loaded area defining the points of zero vertical displacement (i.e. points X and Y in Figure 9.7). The horizontal displacement of the reinforcement at these points is also assumed to be zero, thus the average engineering strain in this portion of reinforcement may be calculated by considering the arc length between points X and Y and is given by:-

$$\epsilon = \frac{\left[1 + \eta^2\right]^{1/2} + \frac{1}{\eta}\sinh^{-1}(\eta)}{2} - 1 \qquad (9.15)$$

where:-

$$\eta = \frac{2\delta}{B'} \qquad (9.16)$$

and δ is the wheel displacement.

The reinforcement is assumed to be linearly elastic with respect to engineering strain, thus the average tension in the portion between X and Y is given by:-

$$T = K\,\epsilon \qquad (9.17)$$

where K is the reinforcement modulus, and ϵ, the average strain, is defined by equation (9.15).

The variations of reinforcement tension are calculated on the assumption that horizontal forces acting on the reinforcement are zero. The horizontal component of tension in the reinforcement is therefore constant along its length and the tension at point X, T_x, is related to the tension at point Z, T_z, by the relationship:-

$$T_x = \frac{T_z}{\cos(\beta_o)} \tag{9.18}$$

where β_o is the angle of inclination of the reinforcement to the horizontal at points X and Y. Since it may be shown from the geometry of the parabola that:-

$$\cos(\beta_o) = \frac{1}{(1 + \eta^2)^{1/2}} \tag{9.19}$$

where η is defined by equation (9.16), then equation (9.18) may be re-written in the form:-

$$T_x = T_z \ (1 + \eta^2)^{1/2} \tag{9.20}$$

In order to relate T_z to the average tension in the reinforcement, T, the assumption is made that the tension varies linearly along the reinforcement giving the relationship:-

$$2T = T_x + T_z \tag{9.21}$$

where T is defined by equation (9.17). Although this approach is inconsistent with the assumptions made regarding the shape of the reinforcement and the nature of the soil/reinforcement interface stresses, it is adopted for the sake of mathematical simplicity. Combining equations (9.20) and (9.21) gives the relationship between T and T_x:-

$$T_x = \frac{2T\,[1 + \eta^2]^{1/2}}{[1 + \eta^2]^{1/2} + 1} \qquad (9.22)$$

The load/displacement relationship for the wheel is obtained by considering the vertical equilibrium of the portion of reinforcement between points X and Y as shown in Figure 9.8.

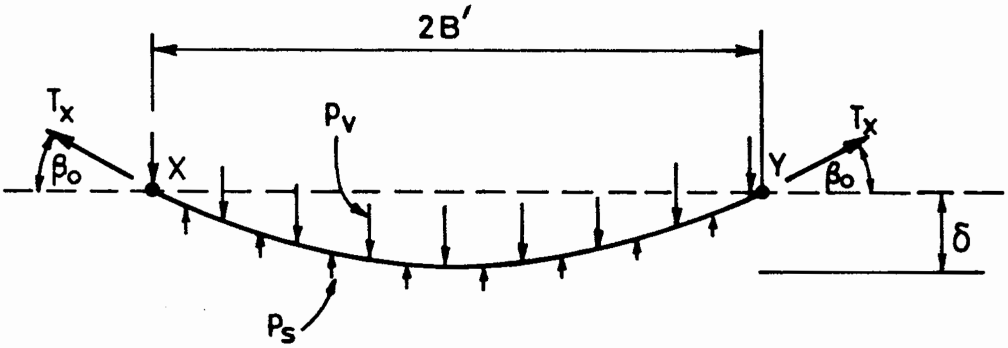

Figure 9.8: Vertical Equilibrium of Reinforcement

The vertical component of the subgrade reaction, p_s, is taken to be:-

$$p_s = (\pi + 2)\,c_u + p_q \qquad (9.23)$$

where c_u is the plane strain shear strength and p_q is the 'effective surcharge' caused by the reversed curvature of the reinforcement outside the loaded area. The condition of vertical equilibrium gives the following expression for p_v, the vertical stress at the base of the fill:-

$$p_v = (\pi + 2)\, c_u + p_q + \frac{T_x \sin(\beta_o)}{B'} \qquad (9.24)$$

The last term in this expression is the 'reinforcement uplift pressure' and the arbitrary assumption is made at this stage that this is equal to the 'effective surcharge', thus:-

$$p_q = \frac{T_x \sin(\beta_o)}{B'} \qquad (9.25)$$

Combining equations (9.19), (9.22), (9.24) and (9.25) gives a relationship between the wheel displacement and the vertical stress at the base of the fill layer:-

$$p_v = (\pi + 2)\, c_u + \frac{4\, K\, \epsilon\, \eta}{[1 + (1 + \eta^2)^{1/2}]B'} \qquad (9.26)$$

The vertical stress directly underneath the wheel, p_f, is related to the vertical stress at the base of the fill layer, p_v, by the expression :-

$$p_f = p_v \left[\frac{B'}{B}\right] \qquad (9.27)$$

The assumption is made in this design method that horizontal stresses acting on the reinforcement are zero. This means that the stresses at the base of the fill layer are not hydrostatic as was found to be the case for the Giroud and Noiray model. In order to investigate the relationship between the normal and vertical stresses at the fill base implied by this assumption, consider the forces acting on an element of reinforcement at the arbitrary point P shown in Figure 9.9. Since the horizontal force on this element is zero, the vertical force applied to the reinforcement, F_v, is related to the normal component, F_n, by:-

$$F_v = \frac{F_n}{\cos(\beta)} \qquad (9.28)$$

where β is the angle of inclination of the reinforcement to the horizontal. The normal pressure p_n, and the vertical pressure p_v, are given by:-

$$p_n = \frac{F_n}{ds} \quad \text{and} \quad p_v = \frac{F_v}{ds\cos(\beta)} \qquad (9.29)$$

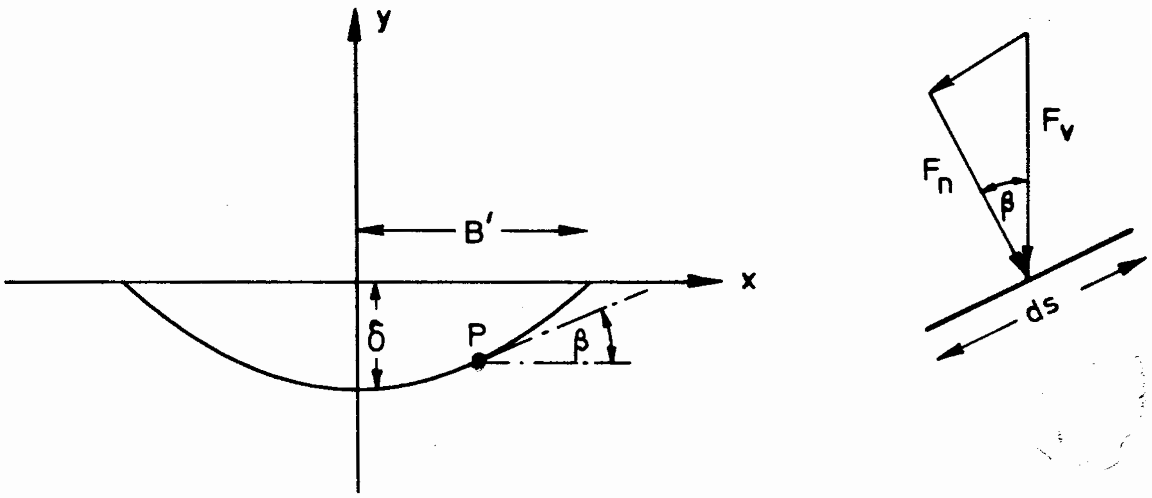

Figure 9.9: Normal and Vertical Forces on Reinforcement

Combining equations (9.28) and (9.29) gives the relationship:-

$$p_n = p_v \cos^2(\beta) \qquad (9.30)$$

The slope of the reinforcement is related to the position of point P by the relationship:-

$$\tan(\beta) = \frac{2\ x\ \delta}{(B')^2} \qquad (9.31)$$

where x is the distance from the footing centre-line. Equations (9.30) and (9.31) therefore combine to give the relationship:-

$$p_n = \frac{p_v}{\left[1 + \left[\frac{2\ x\ \delta}{(B')^2}\right]^2\right]^{1/2}} \qquad (9.32)$$

9.3.1 Comparison with Finite Element Results

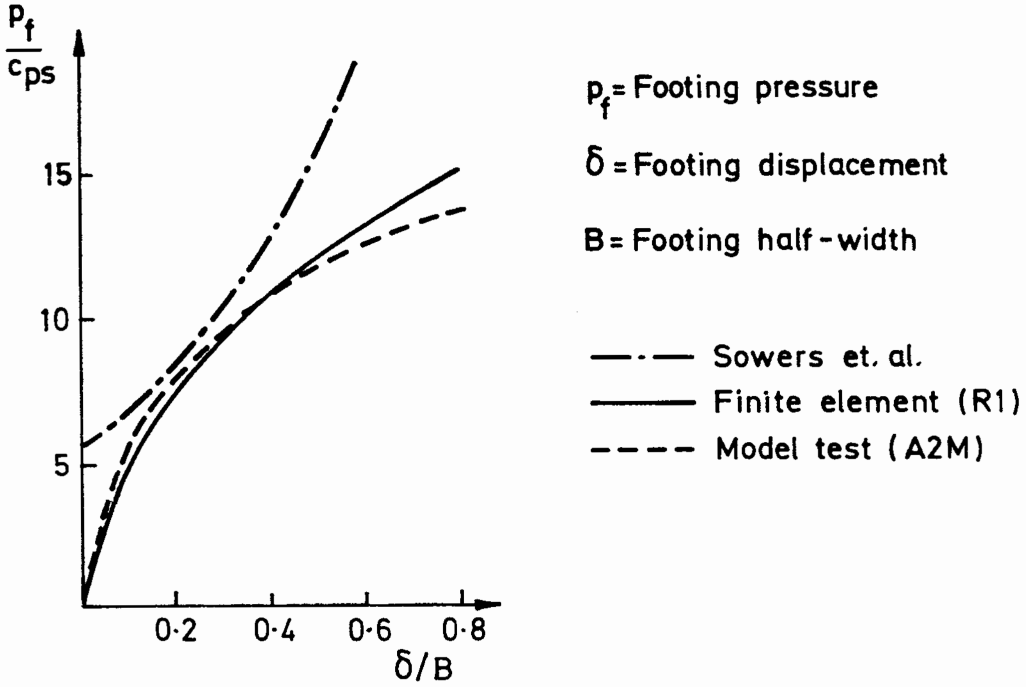

Figure 9.10: Comparison Between Analytical, Numerical and Experimental Load/Displacement Curves

The behaviour predicted by the Sowers model may be compared with any of the single footing finite element calculations described in Chapter 7. Finite element run reference R1 has been chosen for special attention,

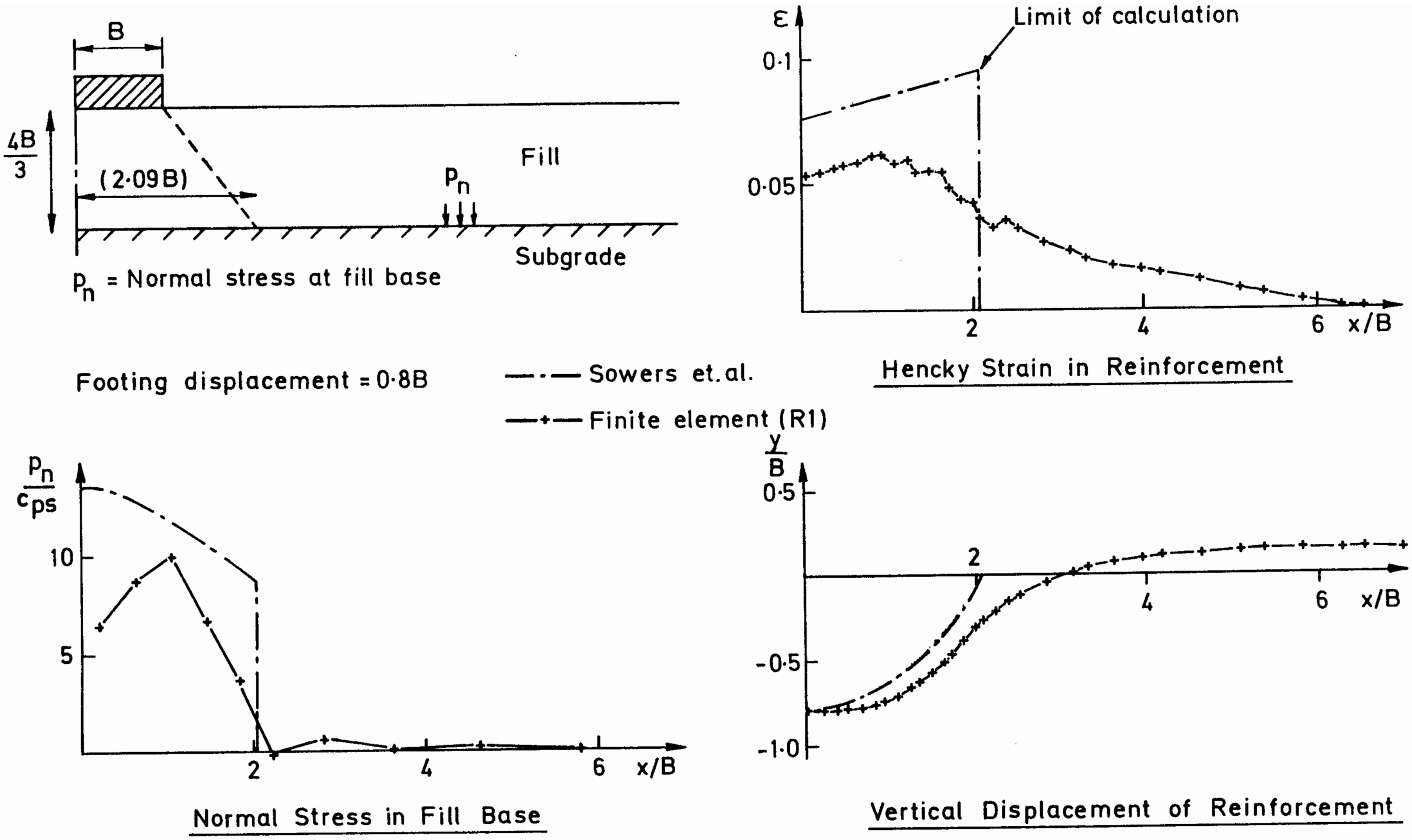

Hencky Strain in Reinforcement

Normal Stress in Fill Base

Vertical Displacement of Reinforcement

Figure 9.11: Comparison Between the Sowers Model and the Numerical Solutions

however, since it corresponds to the same conditions as the dual footing finite element calculation used to assess the Giroud and Noiray model in Section 9.2.1., and has also been discussed in detail in Chapter 8.

The load/displacement relationship obtained from the Sowers model is plotted in Figure 9.10 and compared with the results of the finite element calculation and the corresponding model test (A2M). At very low footing displacements the analytical model provides an overestimate of the bearing capacity as was also found to be the case for the Giroud and Noiray model. Although the comparison between the analytical model and the two other results improves as the displacements increase, it is clear that at very large wheel displacements this design model will seriously overestimate the capacity of the road.

The normal stress at the footing base obtained from equation (9.32) is plotted in Figure 9.11 for a footing displacement of 0.8B and compared with the corresponding finite element results. The analytical model predicts stresses of a higher magnitude than those obtained from the finite element calculation which is consistent with the fact that the wheel load calculated using the Sowers method for this displacement is considerably larger than the corresponding finite element value as indicated by Figure 9.10.

Figure 9.11 also contains a plot in which the reinforcement strains calculated using the Sowers method are compared with the corresponding finite element results for a footing displacement of 0.8B. Although the values predicted by the Sowers method are higher than those obtained from the finite element model, the slopes of the two curves on the footing centre-line are similar which is to be expected since the symmetry condition requires that horizontal forces acting on the reinforcement are zero at this point.

A comparison between the vertical displacement of the reinforcement calculated by the Sowers model and the finite element model for a footing displacement of 0.8B are also plotted in Figure 9.11. The two results agree well on the footing centre-line as was found to be the case for the Giroud and Noiray model. The point of zero vertical displacement predicted by the Sowers method is closer to the wheel centre-line than the corresponding point in the finite element solution, which would explain why the general magnitude of the strains predicted by the Sowers model exceed those obtained from the finite element analysis.

The Sowers method clearly does not offer a significant improvement over the Giroud and Noiray approach. Although this design method does deal with the increased surcharge on the subgrade arising from the reversed curvature of the reinforcement which is ignored by Giroud and Noiray, this is included in an oversimplified way. The Sowers method deals with each wheel load in isolation, and therefore ignores the possibility that two wheels can interact if the spacing is sufficiently small which is a disadvantage of this procedure. As was the case with the Giroud and Noiray method, the Sowers method ignores the 'shear stress effect' (see Section 8.2) which may in some cases be an important mechanism of reinforcement.

CHAPTER 10 CONCLUDING REMARKS

The work described in this thesis consists of the description of a finite element model that is valid for large displacements and the use of the formulation to compute the behaviour of a reinforced unpaved road deforming in plane strain. Emphasis is placed on the accurate modelling of the effects of large strain since substantial surface deformations are generally required to mobilize the reinforcement in structures of this sort. The analysis of problems in continuum mechanics involving large displacements is still a relatively new area of research and as a result no general, well defined approach exists. The finite element theory described in this dissertation is based on an Eulerian description of the deformation which is a method that is particularly suitable for use with the incremental constitutive laws that are common in Soil Mechanics. The Jaumann stress rate is adopted in order to satisfy the requirements of 'objectivity'.

This formulation is capable of making computations that fall well outside the usual scope of the finite element analysis of problems in Soil Mechanics and has therefore been subjected to a rigorous checking process. Firstly, a number of test problems was performed which involved large displacement effects but were sufficiently simple so as to have analytical solutions. Most of these calculations, which are described in Chapter 6, consisted of the analysis of the homogeneous deformation of a block of material having an initially square cross-section. The finite element method was shown to be highly effective in solving problems of this sort, but it should be emphasized that the high level of accuracy achieved in these problems would not necessarily be expected when deformations are non-homogeneous. The second category of test problems consisted of small strain collapse load calculations. Since the full reinforced unpaved road problem is a large strain variant of the collapse load calculation, this series of tests was of considerable importance in spite of the fact that deformations were small. Although the numerical formulation was shown to be capable of predicting the collapse loads within reasonable bounds of accuracy, no indication is given as to whether this is likely to be the case when strains are large.

After the formulation had been checked using these test cases, it was used to perform a series of back-analysis calculations of the results of experiments carried out on model reinforced unpaved roads. These analyses serve partly as additional checks on the finite element computer program and partly to provide values of quantities that were not measured in the tests (i.e. reinforcement tension and the soil/reinforcement interface stress).

The solution scheme was based on the Modified Euler Method, and this was found to be highly suitable for these back-analysis calculations. Solution times for a VAX 11/780 computer ranged from between six and twelve hours of CPU time for the single footing problem and roughly fifteen hours for the dual footing cases. The slowest part of the analysis was invariably the 'stress update' calculation performed at the end of each displacement step. This procedure accounted for up to 80% of the total CPU time and was slower for the Matsuoka material behaviour than the von Mises case.

A number of general conclusions relating to the behaviour of reinforced unpaved roads deforming in plane strain under the action of a single monotonic load can be derived from the results of these back-analysis calculations. It is clear from both the finite element computations and the model test results that the reinforcement has a negligible effect at low surface deformations, but becomes increasingly effective as deformations become appreciable. For the particular cases studied in detail, it was found that the reinforcement had little effect on the load spread action of the fill, but did tend to reduce the shear stresses transmitted from the fill to the subgrade. This latter effect is not considered in any of the commonly used simple design methods. The results of the calculation involving a dual footing indicated that coupling between adjacent wheel loads tends to increase the bearing capacity.

In any practical situation, a reinforced unpaved road is likely to be subjected to repeated loads, and this needs to be considered in design. The inclusion of this type of loading in a finite element formulation of the sort described in this dissertation is, however, not currently feasible since suitable constitutive models are not available and in any case the computing costs would be prohibitive. Static calculations of the sort described in this thesis could be used for design purposes if the calculated reinforcement strength and stiffness, or the fill depth, are increased to cater for the additional requirements of the cyclic effects. This modification could be derived either from empirical results or simply from engineering judgement. A good description of a procedure of this sort is given by Giroud and Noiray (1981).

This finite element formulation is based on constitutive laws that have been kept deliberately simple in order to aid the formulation and implementation of the large strain finite element equations. It is clear, however, that in some points these constitutive relationships are unrealistic, and this aspect of the formulation could be improved in future work. The most obvious shortcoming of the model is that an elastic model based on constant parameters is used to model a frictional material, wheras it is well accepted that the elastic modulus of such materials depends on the stresses. The modification of this formulation to include these effects in such a way as to preclude the possibility of non-conservative material behaviour, however, would require a considerable amount of further work. The material models would also benefit from the inclusion of the effects of strain hardening (or softening). The clay used in the model tests had a shear strength that increased markedly with depth, whereas a subgrade with constant strength and stiffess parameters was used in the back-analysis calculations. The numerical model would be considerably improved if it were modified to allow the material properties to vary with depth, and this feature should be included in any future work.

The analysis of a reinforced unpaved road is a good example of a problem in Soil Mechanics in which large strain effects are important. The formulation described in this thesis has been developed specifically to solve this particular problem, but it is useful to consider whether other problems of a similar nature exist within geotechnical engineering. An obvious example is the cavity expansion that occurs during pile driving. A simple example of a calculation of this sort is included in this thesis, but the formulation could also be used to investigate more complex conditions of geometry and material behaviour. A number of applications exist in the analysis of offshore foundations where the soil is soft and large displacements can occur. Appreciable geometry changes can also occur in the analysis of problems involving consolidation effects.

The size and complexity of problems involving large displacements that can be solved using finite element formulations of the sort described in this thesis are limited by the speed and efficiency of the available computing hardware. If the capabilities of computing equipment increase at the current rate, then large strain computations will be a fruitful area of future research.

REFERENCES

Baker, R. and Desai, C.S. (1982) 'Consequences of Deviatoric Normality in Plasticity with Isotropic Strain Hardening' *Int. J. Num. Analyt. Meth. Geomech. Vol 6(3) pp 383-390*

Barenberg, E.J., Dowland, J.H. and Hales, J.H. (1975) 'Evaluation of Soil-Aggregate Systems with Mirafi Fabrics' *Highway Research Lab. University of Illinois, UILU-ENG-75-2020*

Bathe, K.J., Ramm, E. and Wilson, E.L. (1975) 'Finite Element Formulations for Large Deformation Analysis' *Int. J. Num. Meth. Eng. Vol 9(2) pp 353-386*

Bell, J.R., Greenway, D.R. and Vischer, W. (1977) 'Construction and Analysis of a Fabric Reinforced Low Embankment' *Proc. Int. Conf. Geotextiles, Paris pp 71-75*

Booker, J.R. (1984) Personal communication

Bourdeau, P.L., Harr, M.E. and Holtz, R.D. (1982) 'Soil-Fabric Interaction - An Analytical Model' *Proc. 2nd Int Conf. Geotextiles, Las Vegas pp 387-391*

Boutrup, E. and Holtz, R.D. (1983) 'Analysis of Embankments on Soft Ground Reinforced with Geotextiles' *Proc. 8th ECSFME, Helsinki pp 469-472*

Burd, H.J. and Houlsby, G.T. (1985) 'Finite Element Analysis of Two Cylindrical Expansion Problems Involving Near Incompressible Material Behaviour' *Report No. O.U.E.L. 1580/85, University of Oxford*

Burd, H.J. and Houlsby, G.T. (1986) 'A Large Strain Finite Element Formulation for One Dimensional Membrane Elements' *Comp. and Geotech. Vol 2(1) pp 3-22*

Carter, J.P. (1977) 'Finite Deformation Theory and its Application to Elastoplastic Soils' *Ph.D. Thesis, University of Sydney, Australia*

Carter, J.P., Booker, J.R. and Davis, E.H. (1977) 'Finite Deformation of an Elasto-Plastic Soil' *Int. J. Num. Analyt. Meth. Geomech. Vol 1 pp 25-43*

Christian, J.T., Hagmann, A.J. and Marr, W.A. (1977) 'Incremental Plasticity Analysis of Frictional Soils' *Int. J. Num. Analyt. Meth. Geomech. Vol 1(4)*

Cook, R.D. (1981) 'Concepts and Applications of Finite Element Analysis' *2nd Ed. Wiley*

Cotter, B.A. and Rivlin, R.S. (1955) 'Tensors Associated with Time Dependant Stress' *Quart. Appl. Math. Vol 13 pp 177-182*

Davis, E.H., Ring, G.J. and Booker, J.R. (1974) 'The Significance of the Rate of Plastic Work in Elasto-Plastic Analysis', *Proc. Int. Conf. on Finite Element Methods in Engineering, Sydney, Australia pp 327-337*

Dienes, J.K. (1979) 'On the Analysis of Rotation and Stress Rate in Deforming Bodies' *Acta Mechanica Vol 32 pp 217-232*

Gadala, M.S., Dokainish, M.A. and Oravas, G.AE. (1984) 'Formulation Methods of Geometric and Material Nonlinearity Problems' *Int. J. Num. Meth. Eng. Vol 20(5) pp 887-914*

Gibson, R.E. and Anderson, W.F. (1961) 'In Situ Measurement of Soil Properties with the Pressuremeter' *Civil Engineering and Public Works Review Vol 56 p 615*

Giroud, J-P. and Noiray, L. (1981) 'Geotextile-Reinforced Unpaved Road Design' *J. Geo. Eng. Div., ASCE Vol 107(GT9) pp 1233-1254*

Gourc, J.P. and Riondy, G. (1985) 'Modelisation du Comportment a la Fatique des Chaussees Provisoires Renforcees par Geotextile' Proc. 2nd Symposium Canadien des Geotextiles et Geomembranes, Edmonton

Griffiths, D.V. (1982) 'Computation of Bearing Capacity Factors using Finite Elements' *Geotechnique Vol 32(3) pp 195-202*

Hansen, B. and Christensen, N.H. (1969) 'Discussion of Theoretical Bearing Capacity of Very Shallow Footings' *J. Soil Mech. Fdns. Div., ASCE Vol 95 (SM6) pp 1568-1572*

Hibbitt, H.D., Marcal, P.V. and Rice, J.R. (1970) 'A Finite Element Formulation for Problems of Large Strain and Large Displacement' *Int. J. Sol. Struct. Vol 6(8) pp 1060-1086*

Hill, R. (1950) 'The Mathematical Theory of Plasticity' *Oxford, Clarendon Press*

Hinton, E., Salonen, E.M. and Bicanic, N. (1978) 'A Study of Locking Phenomena in Isoparametric Elements' *The Mathematics of Finite Elements and Applications III (MAFELAP 1978)*

Houlsby, G.T. (1985) 'The Use of the Variable Shear Modulus in Elastic-Plastic Models for Clays' *Comp. and Geotech. Vol 1 pp 3-13*

Hughes, T.J.R. (1977) 'Equivalence of Finite Elements for Nearly Incompressible Elasticity' *J. Appl. Mech. Vol 44 pp 181-183*

Jaumann, G. (1911) *Sitzungsberichte Akad. Wiss. Wien (IIa) 120 p 385*

Johnson, G.C. and Bammann, D.J. (1984) 'A Discussion of Stress Rates in Finite Deformation Problems' *Int. J. Sol. Struct. Vol 20(8) pp 725-737*

Kinney, T.C. (1979) 'Fabric Induced Changes in High Deformation Soil-Fabric-Aggregate Systems' *Ph.D. Thesis, University of Illinois, Michegan, U.S.A.*

Lee, E.H. (1969) 'Elastic-Plastic Deformation at Finite Strains' *J. Appl. Mech. Vol 36 pp 1-6*

Lee, E.H. and McMeeking, R.M. (1980) 'Concerning Elastic and Plastic Components of Deformation' *Int. J. Sol. Struct. Vol 16(1) pp 91-100*

Love, J.P. (1984) 'Model Testing of Geogrids in Unpaved Roads' *D.Phil. Thesis, University of Oxford*

Malkus, D.S. (1976) 'A Finite Element Displacement Model Valid for any Value of the Compressibility' *Int. J. Sol. Struct. Vol 12(11) pp 731-738*

Malkus, D.S. and Hughes, T.J.R. (1978) 'Mixed Finite Element Methods, Reduced and Selective Integration Techniques: A Unification of Concepts' *Comp. Meth. Appl. Mech. Engng. Vol 15 pp 63-81*

Marti, J. and Cundall, P. (1982) 'Mixed Discretization Procedure for Accurate Modelling of Plastic Collapse' *Int. J. Num. Analyt. Meth. Geomech. Vol 6(1) pp 129-139*

Matsuoka, H. (1976) 'On the Significance of the Spatial Mobilised Plane' *Soils and Foundations, Vol 16(1) pp 91-100*

McMeeking, R.M. and Rice, J.R. (1975) 'Finite-Element Formulations for Problems of Large Elastic-Plastic Deformation' *Int. J. Sol. Struct. Vol 11(5) pp 601-616*

Mercier, B. (1979) 'A Conforming Finite Element Method for Two-Dimensional Incompressible Elasticity' *Int. J. Num. Meth. Eng. Vol 14(6) pp 942-945*

Mondkar, D.P. and Powell, G.H. (1978) 'Evaluation of Solution Schemes for Non-linear Structures' *Comp. and Struct. Vol 9(3) pp 223-236*

Moss, W.C. (1984) 'On Instabilities in Large Deformation Simple Shear Loading' *Comp. Meth. Appl. Mech. Engng. Vol 46(3) pp 329-338*

Murnaghan, F.D. (1937) 'Finite Deformations of an Elastic Solid' *Am. J. Math. Vol 59 pp 235-260*

Nagtegaal, J.C., Parks, D.M. and Rice J.R. (1974) 'On Numerically Accurate Finite Element Solutions in the Fully Plastic Range' *Comp. Meth. Appl. Mech. Engng. Vol 4 pp 153-177*

Nagtegaal, J.C. and de Jong, J.E. (1981) 'Some Computational Aspects of Elastic-Plastic Large Strain Analysis' *Int. J. Num. Meth. Eng. Vol 17 pp 15-41*

Nayak, G.C. and Zienkiewicz, O.C. (1972) 'Elasto-plastic Sress Analysis: A Generalization for Various Constitutive Laws Including Strain Softening' *Int. J. Num. Meth. Eng. Vol 5 pp 113-135*

Naylor, D.J. (1974) 'Stresses in Nearly Incompressible Materials by Finite Elements with Application to the Calculation of Excess Pore Pressures' *Int. J. Num. Meth. Eng. Vol 8 pp 443-460*

Nemat-Nasser, S. (1979) 'Decomposition of Strain Measures and their Rates in Finite Deformation Elastoplasticity' *Int. J. Sol. Struct. Vol 15(2) pp 155-166*

Nieuwenhuis, J.D. (1977) 'Membranes and the Bearing Capacity of Road Bases' *Proc. Int. Conf. Geotextiles, Paris pp 3-8*

Oldroyd, J.G. (1950) 'On the Formulation of Rheological Equations of State' *Proc. Roy. Soc. (A) Vol 200 pp 523-541*

Osias, J.R. and Swedlow, J.L. (1974) 'Finite Elasto-Plastic Deformation - I Theory and Numerical Examples' *Int. J. Sol. Struct. Vol 10(3) pp 321-339*

Pian, T.H.H. (1973) 'Hybrid Elements' in 'Numerical and Computer Methods in Structural Mechanics' (Eds. Fenves, S.H., Perrone, N., Robinson, A.R. and Schnobrich, W.C.) *Academic Press, New York pp 59-78*

Pian, T.H.H. and Lee, S.W. (1976) 'Notes on Finite Elements for Nearly Incompressible Materials' *AIAA J. Vol 14 pp 824-826*

Prager, W. (1961a) 'An Elementary Discussion of Definitions of Stress Rate' *Quart. Appl. Math. Vol 18 pp 403-407*

Prager, W. (1961b) 'Introduction to Mechanics of Contiua' *Ginn and Co., Boston*

Prandtl, L. (1921) 'Eindringungsfestigkeit und Festigkeit von Schneiden' *Z. Angew. Math. Mech. Vol 1(15)*

Prevost, J.H. and Hughes T.J.R. (1981) 'Finite-Element Solution of Elastic-Plastic Boundary-Value Problems' *J. Appl. Mech. Vol 48(1) pp 69-74*

Rice, J.R., McMeeking, R.M., Parks, D.M. and Sorensen, E.P. (1979) 'Recent Finite Element Studies in Plasticity and Fracture Mechanics' *Comp. Meth. Appl. Mech. Engng. Vol 17/18 pp 411-442*

Sagaseta, C. (1984) Personal communication

Sellmeijer, J.B., Kenter, C.J. and Van den Berg, C. (1982) 'Calculation Method for a Fabric Reinforced Road' *Proc. 2nd Int. Conf. Geotextiles, Las Vegas pp 393-398*

Seth, B.R. (1935) 'Finite Strains in Elastic Problems' *Phil. Trans. Roy. Soc. (A) Vol 234 pp 231-264*

Shimodaira, H. (1985) 'Equivalence Between Mixed Models and Displacement Models Using Reduced Integration' *Int. J. Num. Meth. Eng. Vol 21(1) pp 89-104*

Sloan, S.W. (1981) 'Numerical Analysis of Incompressible and Plastic Solids Using Finite Elements' *Ph.D. Thesis, University of Cambridge*

Sloan, S.W. (1984) 'Substepping Schemes for the Numerical Integration of Elastoplastic Stress-Strain Relations' *Report No. 003.12.84, Dept. of Civil Engineering and Surveying, University of Newcastle, New South Wales, Australia*

Sloan, S.W. and Randolph, M.F. (1982) 'Numerical Prediction of Collapse Loads Using Finite Element Methods' *Int. J. Num. Analyt. Meth. Geomech. Vol 6 pp 47-76*

Sowerby, R. and Chu, E. (1984) 'Rotations, Stress Rates and Strain Measures in Homogenous Deformation Processes' *Int. J. Sol. Struct. Vol 20(11/12) pp 1037-1048*

Sowers, G.F., Collins, S.A. and Miller, D.G. (1982) 'Mechanisms of Geotextile-Aggregate Support in Low Cost Roads' *Proc. 2nd Int. Conf. Geotextiles, Las Vegas pp 341-346*

Spilker, R.L. (1981) 'Improved Hybrid-stress Axisymmetric Elements Including Behaviour for Nearly Incompressible Materials' *Int. J. Num. Meth. Eng. Vol 17(4) pp 483-501*

Steward, J. and Mohney, J. (1982) 'Trial Use and Experience Using Geotextiles for Low-Volume Forest Roads' *Proc. 2nd Int. Conf. Geotextiles, Las Vegas pp 335-340*

Stricklin, J.A. and Haisler, W.E. (1977) 'Formulations and Solution Procedures for Nonlinear Structural Analysis' *Comp. and Struct. Vol 7(1) pp 125-136*

Taylor, L.M. and Becker, E.B. (1983) 'Some Computational Aspects of Large Deformation, Rate-Dependant Plasticity Problems' *Comp. Meth. Appl. Mech. Engng. Vol 41 pp 251-277*

Thomas, J.N. (1984) 'An Improved Accelerated Initial Stress Procedure for Elasto-Plastic Finite Element Analysis' *Int. J. Num. Analyt. Meth. Geomech. Vol 8 pp 359-379*

Toh, C.T. and Sloan, S.W. (1980) 'Finite Element Analysis of Isotropic and Anisotropic Cohesive Soils with a View to Correctly Predicting Impending Collapse' *Int. J. Num. Analyt. Meth. Geomech. Vol 4 pp 1-23*

Truesdell, C. (1953) 'The Mechanical Foundations of Elasticity and Fluid Dynamics' *J. Rat. Mechs. Analys. Vol 2(3) pp 593-616*

Tseng, N.T, and Lee, G.C. (1985) 'Inelastic Finite Strain Analysis of Structures Subjected to Nonproportional Loading' *Int. J. Num. Meth. Eng. Vol 21 pp 941-957*

Yamada, Y. and Wifi, A.S. (1977) 'Large Strain Analysis of Some Geotechnical Problems by the Finite Element Method' *Int. J. Num. Analyt. Meth. Geomech. Vol 1 pp 299-318*

Zeevaert, A.E. (1980) 'Finite Element Formulation for the Analysis of Interfaces, Nonlinear and Large Displacement Problems in Geotechnical Engineering' *Ph.D. Thesis, Georgia Institute of Technology, Atlanta, Georgia*

Zienkiewicz, O.C. (1977) 'The Finite Element Method' *McGraw-Hill, London*

Zienkiewicz, O.C., Humpheson, C. and Lewis, R.W. (1975) 'Associated and Non-Associated Visco-Plasticity and Plasticity in Soil Mechanics' *Geotechnique Vol 25(4) pp 671-689*

Zytynski, M., Randolph, M.F., Nova, R. and Wroth, C.P. (1978) 'On Modelling the Unloading-Reloading Behaviour of Soils' *Int. J. Num. Analyt. Meth. Geomech. Vol 2 pp 87-94*